STUDYING THE FORMULATION EFFECTS
ON STEADY-STATE AND TRANSIENT COMBUSTION BEHAVIOR
OF ALUMINIZED PROPELLANTS

Final Technical Report

by

Prof. Vladimir E. Zarko, principal investigator

Novosibirsk, 1999

REPORT DOCUMENTATION PAGE

form Approved
OMB No. 0704-0188

1. AGENCY USE ONLY	2. REPORT DATE **30 JULY 1999**	3. REPORT TYPE AND DATES COVERED **FINAL, 07 SEPTEMBER 98 - 07 JUNE 99**

4. TITLE AND SUBTITLE
STUDYING THE FORMULATION EFFECTS ON STEADY-STATE AND TRANSIENT COMBUSTION BEHAVIOR OF ALUMINIZED PROPELLANTS

5. FUNDING NUMBERS

6. AUTHORS
V. E. Zarko, O. G. Glotov, V. V. Karasev, V. N. Simonenko, A. B. Kiskin, A. G. Svit, L. K. Gusachenko

7. PERFORMING ORGANIZATION NAME(S) AND ADDRESS(ES)
Institute of Chemical Kinetics and Combustion
Russian Academy of Sciences,
Novosibirsk, 630090, Russia

8. PERFORMING ORGANIZATION REPORT NUMBER
N/A

9. SPONSORING/ MONITORING AGENCY NAME(S) AND ADDRESS(ES)
United States Air Force European Office of Aerospace Research and Development 223/231 Old Marylebone Road, London NW1 5TH, United Kingdom

10. SPONSORING / MONITORING AGENCY REPORT NUMBER
F61708-97-W0197

11. SUPPLEMENTARY NOTES

12a. DISTRIBUTION/AVAILABILITY STATEMENT

12b. DISTRIBUTION CODE

13. ABSTRACT. A new approach based on use of special "super heterogeneous" propellants that generate during combustion the model agglomerates with given reproducible size and structure has been elaborated for study of model agglomerate evolution. The experiments with agglomerates of 395÷540 µm size and initial aluminum content 42.6 % were carried out in pressure range 1-80 atm. The following correlation for incompleteness of aluminum combustion η has been found: $\eta = 2.86 \cdot t^{0.28} \cdot P^{-0.20}$, where $\eta = m_{Al} / m_{Al}^0$; m_{Al} is the mass of unburnt aluminum in sampled agglomerate and m_{Al}^0 is the initial mass of aluminum in agglomerate; t is the residence time for agglomerate in flame of burning sample ($20 < t < 90$ ms); P – pressure ($10 < P < 70$ atm). It was also found that the mass fraction φ of oxide accumulated on the burning agglomerate increases with completeness of aluminum combustion $\xi = 1 - \eta$ as $\varphi = 0.539 + 0.213 \cdot \xi$, and agglomerate mass also increases with ξ due to oxide accumulation on the burning agglomerate. For calculation of burning agglomerate motion law and residence time for agglomerate in flame the drag coefficient C_d was taken in the form $C_d = K/Re$. Here Re is the Reynolds number. K was determined in experiments on particle trajectory visualization and found to be equal $K = 45 \pm 7$ at $7 < Re < 9$. The characteristics of condensed combustion products (CCP) were measured via sampling technique at pressure 46 atm (argon or nitrogen) for 12 metalized propellant formulations manufactured using well characterized ingredients. All compositions were based on energetic binder (20%). They included totally 18 % aluminum (commercial or ultra fine particles in various proportion) and contained AP or AP and HMX as oxidizer. The replacement of commercial aluminum by electrically exploded aluminum (Alex) lead to increase of burning rate, decrease of agglomerate mass and increase of metal conversion completeness. All propellant formulation exhibited very effective aluminum conversion (total unburnt aluminum content in CCP did not exceed 9%). The listed trends are mostly expressed in combustion of HMX containing propellants and even small additive of Alex (Alex/Al = 8.3/91.7) gives sizable effect. For oxide particles in the size range 0.5-100 µm the typical three-peak structure of mass size distribution was found. The replacement of aluminum by Alex and using argon instead of nitrogen affects slightly the CCP size distribution. Thermal decomposition of different types of the binders and mixtures modeling the pocket matter was investigated at low (10 K/min) and fast ($\geq$ 450 K/min) heating rate. Data obtained are not sufficient to make clear the cause of difference in agglomeration behavior for propellant formulations based on these types of binders.

14. SUBJECT TERMS: Combustion, solid propellant, condensed combustion products, sampling, aluminum agglomeration, ultra fine, electro-exploded aluminum, Alex, agglomerate evolution, aluminum oxide, aluminu nitride, particle size distribution, particle density, aluminum combustion efficiency, decomposition temperature fast thermal pyrolysis of binder, burning particle motion, drag coefficient, argon.

15. NUMBER OF PAGES
97

16. PRICE CODE

17. SECURITY CLASSIFICATION OF REPORT	18. SECURITY CLASSIFICATION OF THIS PAGE	19. SECURITY CLASSIFICATION OF ABSTRACT	20. LIMITATION OF ABSTRACT

ABSTRACT

A new approach based on use of special "super heterogeneous" propellants that generate during combustion the model agglomerates with given reproducible size and structure has been elaborated for study of model agglomerate evolution. The experiments with agglomerates of $395 \div 540$ µm size and initial aluminum content 42.6 % were carried out in pressure range 1-80 atm. The following correlation for incompleteness of aluminum combustion η has been found: $\eta = 2.86 \cdot t^{0.28} \cdot P^{-0.20}$, where $\eta = m_{Al} / m_{Al}^0$; m_{Al} is the mass of unburnt aluminum in sampled agglomerate and m_{Al}^0 is the initial mass of aluminum in agglomerate; t is the residence time for agglomerate in flame of burning sample ($20 < t < 90$ ms); P – pressure ($10 < P < 70$ atm). It was also found that the mass fraction φ of oxide accumulated on the burning agglomerate increases with completeness of aluminum combustion $\xi = 1 - \eta$ as $\varphi = 0.539 + 0.213 \cdot \xi$, and agglomerate mass also increases with ξ due to oxide accumulation on the burning agglomerate. For calculation of burning agglomerate motion law and residence time for agglomerate in flame the drag coefficient C_d was taken in the form $C_d = K/Re$. Here Re is the Reynolds number. K was determined in experiments on particle trajectory visualization and found to be equal $K = 45 \pm 7$ at $7 < Re < 9$.

The characteristics of condensed combustion products (CCP) were measured via sampling technique at pressure 46 atm (argon or nitrogen) for 12 metalized propellant formulations manufactured using well characterized ingredients. All compositions were based on energetic binder (20%). They included totally 18 % aluminum (commercial or ultra fine particles in various proportion) and contained AP or AP and HMX as oxidizer. The replacement of commercial aluminum by electrically exploded aluminum (Alex) lead to increase of burning rate, decrease of agglomerate mass and increase of metal conversion completeness. All propellant formulation exhibited very effective aluminum conversion (total unburnt aluminum content in CCP did not exceed 9%). The listed trends are mostly expressed in combustion of HMX containing propellants and even small additive of Alex (Alex/Al = 8.3/91.7) gives sizable effect. For oxide particles in the size range 0.5-100 µm the typical three-peak structure of mass size distribution was found. The replacement of aluminum by Alex and using argon instead of nitrogen affects slightly the CCP size distribution.

Thermal decomposition of different types of the binders and mixtures modeling the pocket matter was investigated at low (10 K/min) and fast ($\geq$ 450 K/min) heating rate. Data obtained are not sufficient to make clear the cause of difference in agglomeration behavior for propellant formulations based on these types of binders.

Keywords

ACKNOWLEDGEMENTS

TABLE OF CONTENT

1. INVESTIGATION OF MODEL AGGLOMERATE EVOLUTION

1.1. Background

Using of metal combustion in rocket propulsion motivated by higher theoretical specific impulse of solid propellants with metal additives created the numerous agglomeration problems. Aluminum particles may react and merge in a subsurface layer or/and on the burning surface forming agglomerates that then burn in gas phase [1]. Studying the agglomeration of metal in the combustion wave can be divided onto *internal* and *external* problems. The internal problem implies obtaining answer on two important questions: 1) How do the agglomerates form, and 2) What are the agglomerate parameters at the moment of detachment from the burning surface? In practice, to solve this problem one has to determine size distribution function as well as internal structure and chemical composition of agglomerates. It is also necessary to know the dependence of those agglomerate characteristics of combustion conditions and chemical composition and granule size of heterogeneous components of propellant.

External problem implies investigation of kinetics of metal burn out in agglomerates when they move in environment of combustion products of propellant. When calculating the energy release, the rate of metal consumption is of major importance while in calculations of two-phase flow the mass and size of agglomerates play crucial role. Unfortunately, there are no detailed combustion models that may allow to predict precisely the agglomerate size and its temporal behavior. Therefore, the only potential source of reliable information about agglomerate characteristics and transient behavior remains experiment with inherent problems regarding the instrumental errors and data scattering. Note that there might arise specific problems with processing and treatment of experimental data.

Among different experimental approaches used for studying the agglomerates behavior one of the most informative is the sampling technique which provides obtaining data on size distribution and chemical composition of agglomerates. However, interpretation of these data meets serious difficulties caused by complex character of formation and motion of metal agglomerates in flame.

First of all, the agglomerates have broad range of sizes because of statistical nature of process of their formation. The motion of agglomerates in flame depends on their size, density, and gas flow field. All these parameters may vary depending on prehistory of metal combustion behavior (residence time on the surface, efficiency of merging, ignition, etc.) as well as of local burning rate at the surface (ignition and extinction of local spots). As a matter of fact, for given individual agglomerate within large number of particles it is difficult to evaluate real residence time and real local composition of gaseous combustion products. When doing laboratory scale experiments with restricted number of sampled particles and remarkable effect of boundary conditions, it leads to essential errors and scattering of experimental data.

In order to eliminate (or diminish) uncertainty in experimental data the novel experimental approach has been suggested. The approach is based on experimenting with special design model propellants generating the monodisperse agglomerates of specific structure which burn in combustion gases of given composition. It is expected that by using such propellant one will be able to determine correctly the particle motion law and the residence time for particles in flame. These data should give valuable information about agglomerate evolution behavior and can be used in the future for analysis of the metal combustion efficiency in real propellants.

1.2. Model propellant generating the monodisperse agglomerates.

1.2.1. Basic idea

The first proposal on manufacturing and investigation of model composite propellant capable to generate equal size metal agglomerates was formulated in our laboratory in 1989. The propellant named as "super heterogeneous" (SH) consists of homogenized matrix (all powders of small grain size) with inclusion of macro elements simulating the "pocket" composition in real coarse oxidizer propellants. These macro elements are named below by equivalent term "insertions" or "inclusions".

It is supposed that in the combustion wave each inclusion transforms into single agglomerate whose size is determined by initial size and composition of macro element. Using homogenized matrix allows to avoid the complex multiple jet structure of gaseous products flow and provides closeness of their characteristics to the thermodynamics calculated ones.

The following considerations were taken into account when making choice of the formulation:

- The properties of real propellant under simulation. The material for inclusions must be similar to the pocket matter in real propellant, i. e. it should have the same formulation as that in local space between coarse oxidizer grains in real propellant. In particular, the propellant for insertions includes fine AP grains. Fortunately, it appeared that fine AP facilitated an ignition of insertion in a very effective way.
- The thermodynamics calculation data to maximize the burning temperature of homogenized matrix.
- The technological restrictions of propellant mass mixing.

1.2.2. Realization – propellant formulations.

The composition of the SH propellant components is presented in Table 1.1

Table 1.1. Matrix and inclusion formulations (% mass.) in SH propellant

Ingredient	Matrix	Insertion
Energetic binder[a]	27	42.6
Al (D_{30} ~15 μm)[b]	-	42.6
AP (S = 6700 cm^2/g)	34	14.8
HMX (re-crystallized)[c]	39	-
Density, g/cm^3	1.71±0.05	1.74±0.04

Comments:

a) The energetic binder based on nitryl rubber plastisized by diethylene glycol dinitrate (DEGDN) (98%) with additives (2%) was used.

b) The content of metal in virgin aluminum particles amounted 97.8 ± 0.9%.

c) Commercial cyclotetramethylene tetranitramine (HMX) powder was re-crystallized in order to reduce the grain size. For this a solution of HMX in acetone was instilled by thin flood in cooled water. Then a suspension of fine HMX crystals was filtered and dried at room temperature.

The results of particle size distribution analysis for aluminum (Al), ammonium perchlorate (AP) and HMX powders are shown in Figs 1.1-1.3. The automated sizer Malvern 3600E was employed for particle size analysis. The following substances were used as a carried liquid in Malvern analyses: hexane for AP and HMX powder, water for Al powder.

The results of thermodynamics calculations for combustion products of non-metalized martix made using Russian computer code ASTRA-3 are shown in Table 1.2. The following parameters are presented for gaseous products (gp): flame temperature T_{gp}, viscosity μ, molar mass M_{gp}, heat capacity C_p, and mass fraction of main ingredients.

Table 1.2. Thermodynamics data on combustion products calculated at various pressures P

	$P=$ 1 atm	$P=$ 12.8 atm	$P=$ 23.5 atm	$P=$ 46 atm	$P=$ 85 atm
T_{gp}, K	2805	3008	3050	3093	3127
μ, Pa·s	$0.8080 \cdot 10^{-4}$	$0.8483 \cdot 10^{-4}$	$0.8565 \cdot 10^{-4}$	$0.8648 \cdot 10^{-4}$	$0.8715 \cdot 10^{-4}$
M_{gp}, g/mol	24.20	24.65	24.74	24.84	24.91
C_p, kJ/(kg·K)	1.8389	1.8563	1.8597	1.8631	1.8659
Mass fraction of substances					
O_2	$0.5764 \cdot 10^{-2}$	$0.2459 \cdot 10^{-2}$	$0.1862 \cdot 10^{-2}$	$0.1315 \cdot 10^{-2}$	$0.92022 \cdot 10^{-3}$
HCl	0.05838	0.06423	0.06551	0.06681	0.06789
N_2	0.19293	0.19672	0.19757	0.19846	0.19921
H_2O	0.28697	0.30560	0.30963	0.31374	0.31711
H_2	0.08408	0.07950	0.07851	0.07752	0.07672
CO	0.20502	0.20483	0.20461	0.20434	0.20408
CO_2	0.10018	0.10597	0.10737	0.10882	0.11003
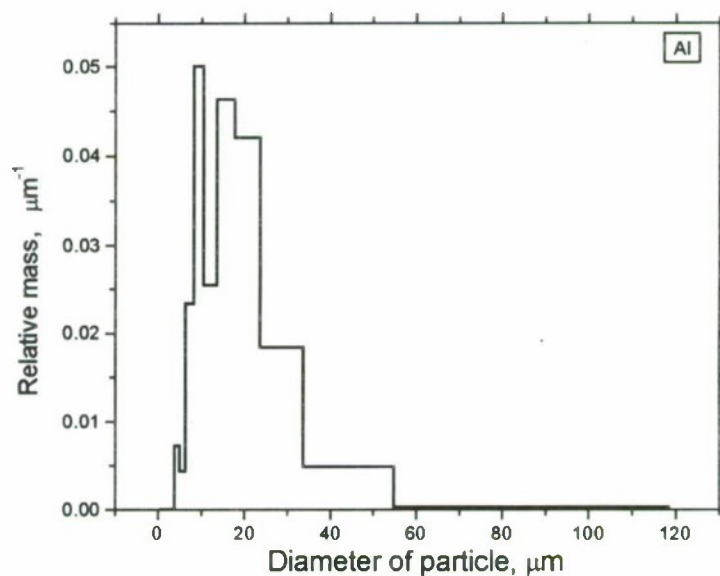
Fig. 1.1. Mass size distribution for aluminum used in manufacturing the model propellants. Measurements were made by Malvern 3600E in water after treatment by ultrasound during 40 seconds, mixer ON, size range 0.5-118.4 μm.

D_{mn}, μm: D_{10}= 4.2; D_{20}= 4.8; D_{30}=5.8; D_{21}=5.4; D_{32}=8.7; D_{43}=15.0; D_{53}=18.3.
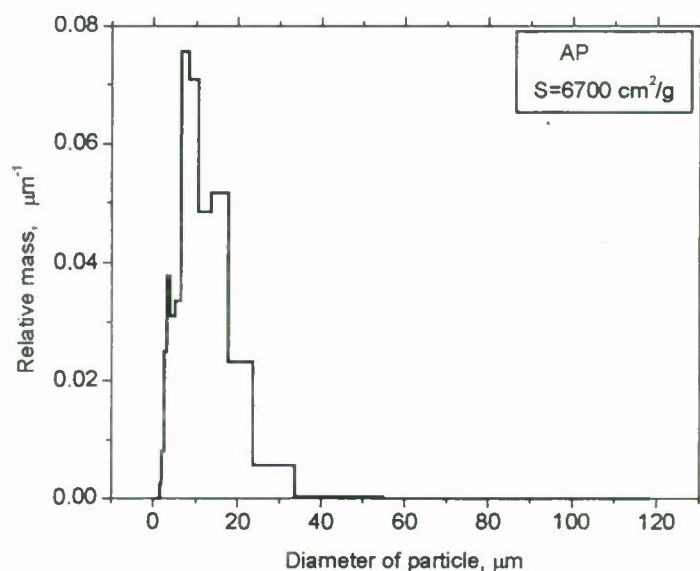
Fig. 1.2. Mass size distribution for AP with S = 6700 cm^2/g used to manufacture the model propellants.

Measurements were made by Malvern 3600E in hexane, mixer ON, size range 0.5-118 μm.

D_{mn}, μm: D_{10}=4.5; D_{20}=5.4; D_{30}=6.6; D_{21}=6.5; D_{32}=9.6; D_{43}=13.1; D_{53}=14.8.

5
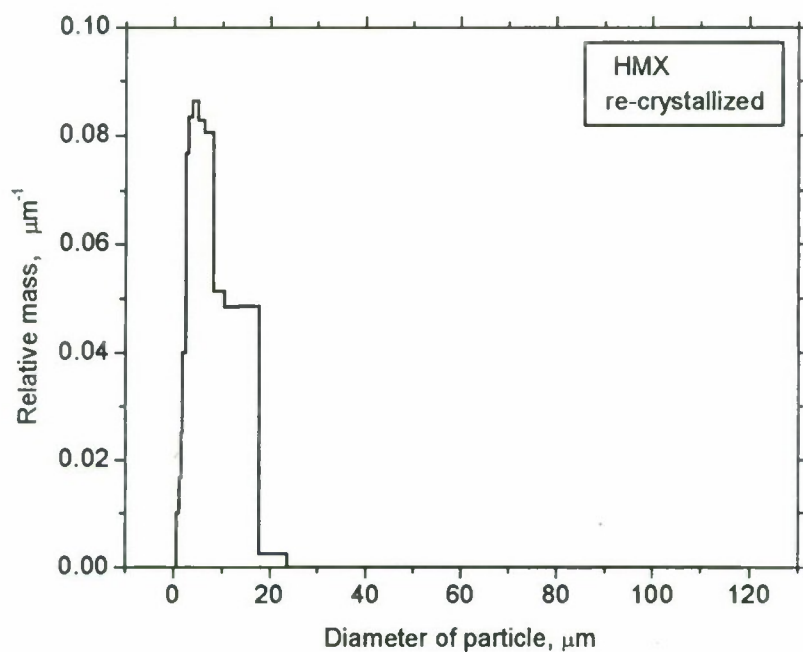
Fig. 1.3. Mass size distribution for re-crystallized HMX used to manufacture the model propellants.

Measurements were made by Malvern 3600E in hexane, mixer ON, size range 0.5-118 μm. D_{mn}, μm: D_{10}=2.0; D_{20}=2.6; D_{30}=3.5; D_{21}=3.5; D_{32}=6.0; D_{43}=8.9; D_{53}=10.1.
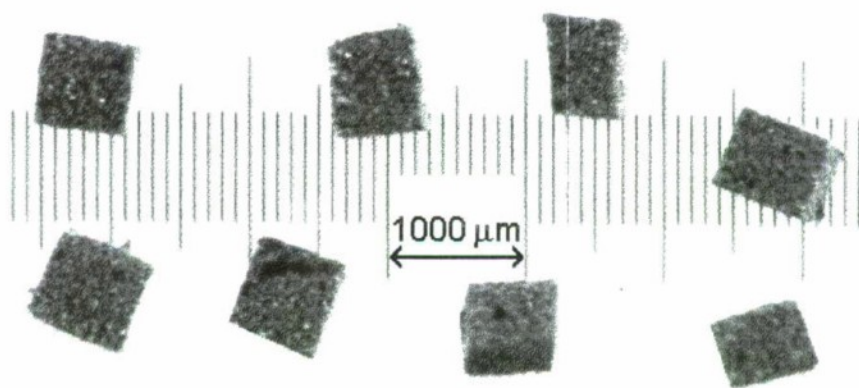
Fig. 1.4. Agglomerate seeds- miniature cubic shape pieces of metalized propellant. A few tens (60-120) of such inclusions were inserted into non-metalized matrix in course of preparation of each super heterogeneous propellant sample.

1.2.3. Realization – specimens for sampling experiments.

A procedure for manufacturing super heterogeneous propellant specimens for experiments in sampling bomb consists of following steps:

1. Manufacturing the cured model metalized propellant for inclusions. Curing of cylindrical slabs of propellant was made in air at 70°C during 170 hours.
2. Manufacturing uncured non-metalized propellant for matrix.
3. Making the inclusion elements via cutting the propellant for inclusions into small pieces of approximately equal size. The set of 5 shaving blades fixed in parallel using spacers of 500 μm height was employed for cutting. The insertion elements were of cubic shape with rib about 500 μm, see Fig. 1.4, and had the weight about 0.2 mg each.
4. Selecting necessary amount (60-120) of pieces having approximately equal size for inserting into one sample. The scatter of initial agglomerate mass and size depends on this tedious work.
5. Inserting these elements into matrix propellant mass. This mass had the plasticine consistence. For more operative work the ready samples were not cured. The insertion was made as follows. From the beginning the thin layer (~ 1 mm) of matrix was placed on the bottom of sample cup (cylindrical glass). Then a few of "cubs" were pressed in this layer with butt-end of cylindrical pistil made of teflon. After that the next layer of non-metalized matrix was placed on the previous one. Again the few cubs were pressed into the layer surface and so forth, until filling the sample holder cylinder. The inserted cubs were localized no closer than 1 mm to the bottom, walls and flush of the glass.

The mass fraction of inclusions was 1.2-3 %. Thus we assumed that the composition of the gaseous combustion products was not changed as a result of the agglomerate combustion.

1.3. Experimental set up and procedure.

The ordinary sampling technique [2] was used to investigate the model agglomerate evolution. Briefly, the burning particles are quenched by inert gas flow, captured by the wire mesh screen and aerosol filter AFA and then subjected to particle size distribution and chemical analyses.

The blow through bomb (Fig. 1.5) consists of massive case *1* supplied with gas inlet *11* and outlet *6* valves which allow to maintain an appropriate gas flow rate in the bomb. Inside the bomb there is a steel cylinder *3* of 50 mm in diameter with propellant specimen *9* mounted in the top cover *2* (inner part) of cylinder. The bottom of a cylinder is supplied with wire mesh screen and aerosol analytical filter AFA *5*. The propellant specimen is ignited by nichrome wire *8* and the flame torch is directed downward. The tube *7* made of plexiglass provided protection of combustion products against mixing with environmental gas. After leaving the tube the combustion products mix with cold nitrogen filling the bomb and cylinder interior through the top ring slot *10* ($\varnothing 40 - \varnothing 30$ mm).

The burning rate was calculated as specimen height divided by the burn out time. The last one was determined from pressure-*vs*-time record in the case of elevated pressures 10 - 64 atm and from temporal record of light emission of burning specimen in the case of pressure 1 atm. In this last case a photodiode was mounted inside the bomb in cylinder *3*, see Fig. 1.5. The maximum rise of pressure during the combustion run was 6 atm in the experiments with at initial pressure 60

atm. The characteristic pressure was taken as a half of sum of initial and final pressures. The mass flow rate of nitrogen through the bomb was in the range 0÷2 g/s.

The sampling technique has been described previously [2-3, 10-11] in detail. Therefore we list below only specific features of the technique option used in this study.

• One wire screen with nominal mesh size 130 μm was used instead of the stack of screens.

• Particle size analysis and chemical analysis were performed for each propellant sample test run.

• Five types of firing geometry were used to provide different length of initial mixing area for co-current flows of gaseous combustion products and cooling nitrogen and, subsequently, different residence time for particles in flame. Two different propellant sample diameters (7 mm or 12 mm) and three length of protecting tube (28 mm, 56 mm, and 98 mm) allowed to vary the residence time of particles in flame within the interval 20-100 ms. The protective tube was used only with the samples having diameter 12 mm. The inner diameter of glasses, and the inner diameter of protective tubes were equal to the sample diameter. The sample geometry types (*A-E*) are pictured in Fig. 1.6.

• The agglomerates captured by wire screen in the bomb were weighed with an error of no less than 0.00015 g, photographed by projection scanner Uniscan (Russia) with following measurement of their sizes using printed copy. The accuracy of size measurement has been estimated as a half of histogram sub-range and it was equal to 15-30 μm. After making particle size measurement the agglomerate were subjected to chemical analysis. The latter was made by permanganatometric method [4] that allows to determine the unburnt aluminum content. The mass of particles trapped by filter was calculated as the difference of filter mass before and after the combustion experiment. Particles from filter wasted by soot-like plexiglas pyrolysis products were not analyzed on aluminum content, only their total mass was used to control.

• The density of agglomerate particles was calculated by the formula

$$\rho = m \left/ \left(N \, \frac{\pi}{6} D_{30}^3 \right) \right. ,$$

using experimentally determined values of m - the mass of particle population, N – number of particles, and D_{30} - the average size.

The estimated error [5] can be calculated as

$$\Delta \rho = \rho \cdot \sqrt{\left(\frac{3 \Delta D_{30}}{D_{30}} \right)^2 + \left(\frac{\Delta m}{m} \right)^2 + \left(\frac{\Delta N}{N} \right)^2} \, .$$

To calculate $\Delta \rho$ the following instrumental errors have been used: ΔD_{30}=15-30 μm, Δm=0.00015 g, ΔN=0.
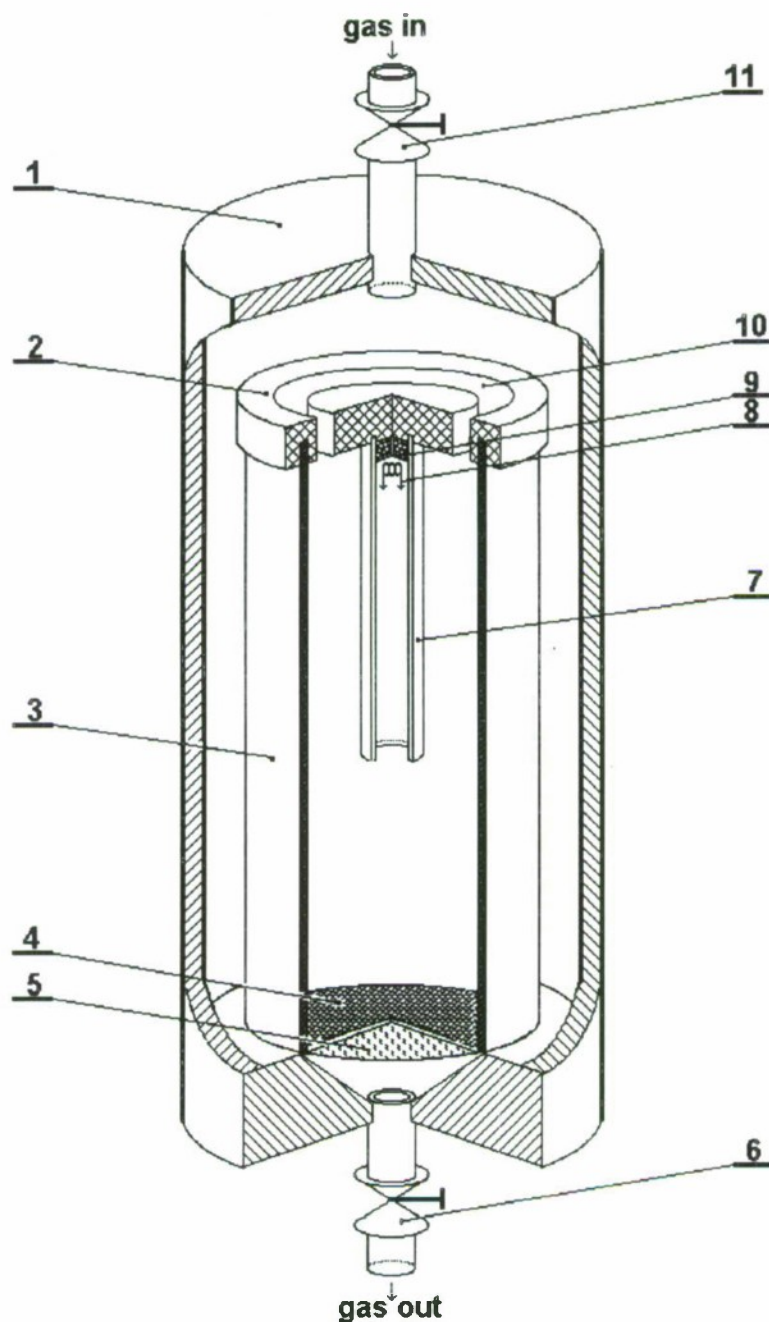
Fig. 1.5. Chart of the flow bomb for agglomerate sampling:

_1_	-	bomb body,	_7_	-	protective tube,
_2_	-	top cover of the cylinder 3,	_8_	-	ignition wire,
_3_	-	thin wall cylinder,	_9_	-	propellant specimen,
_4_	-	wire mesh screen,	_10_	-	ring slot for blowing the cylinder 3,
_5_	-	filter,	_11_	-	gas inlet valve.
_6_	-	gas outlet valve,			
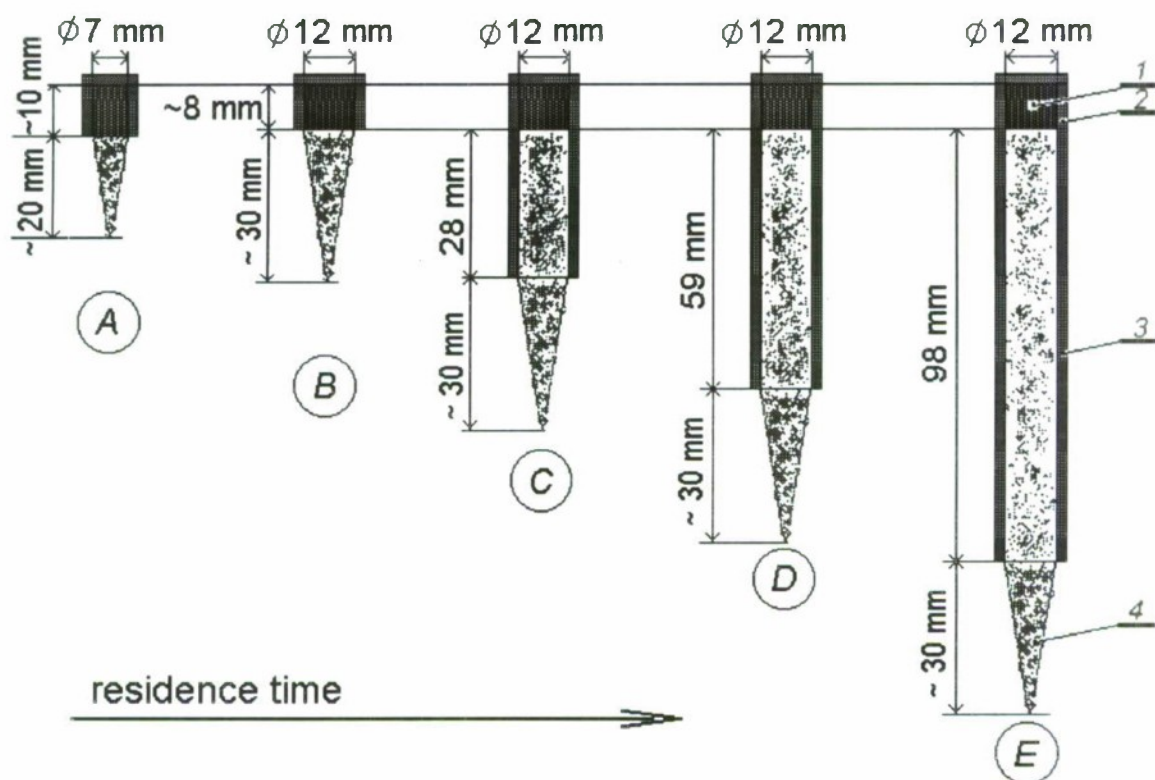
Fig. 1.6.

Five types of firing geometry (*A-E*) that provided variation of the residence time for agglomerate particles in flame.

1 - propellant specimen,	*3* - protective tube,
2 - cylindrical sample holder,	*4* - initial mixing area L_{mix}.

1.4. Residence time calculations

The particle motion was calculated individually for each test run using modified Stokes law. The procedure included 5 steps.

Step 1. Thermodynamics calculation of gaseous products at given pressure was performed using Russian code ASTRA-3. For each calculated run the mass of plexiglas burnt was added to the mass of propellant sample. The mass of burnt plexiglas was measured experimentally as the difference between mass of mounting cylindrical holder and protective tube before and after run. This mass depends essentially on protective tube length and pressure. Thus, the effective flame temperature and other parameters of gas were different of these for pure matrix (see Table 1.2). The gas proterty for used values obtained in thermodynamics calculations were as follows.

Flame temperature or temperature of gaseous combustion products T_{gp} = 1699÷3049 K,

Molecular mass of gaseous combustion products M_{gp} = 19.834÷24.598,

Dynamic viscosity of the gaseous combustion products μ =(0.5567÷0.8551)·10^{-4} Pa·s,

Heat capacity C_p = 1.8671÷1.8876 kJ/(kg·K),

Step 2. The characteristic length of mixing, or initial mixing area L_{mix} has been calculated by the formula [6] for turbulent co-current coaxial streams taking into consideration the difference in temperature and density of mixing gases.

Step 3. The gas flow field was calculated using original 2D computer code FLOW. The result of calculations are stationary axis-symmetrically fields of temperature, nitrogen and combustion products concentrations and velocities in bomb interior including protective tube and cylinder *3*, see Fig. 1.5. The combustion product source was assumed to be placed at the bottom of sample holder. The initial velocity of gaseous combustion products is determined by the mass continuity equation in the form

$$V_{gp}= \rho_{matrix} \cdot r_b \cdot (1-\alpha)/\rho_{gp},$$

where ρ_{matrix} = 1.71 g/cm^3 is the density of non-metalized matrix propellant, r_b is the burning rate, α is the mass fraction of non-gasified part of propellant sample. For studied super heterogeneous propellant the α value was taken as a 42.6% of mass of metalized inclusions in propellant sample. An example of such calculation results is presented in Fig. 1.7.

Step 4. Calculation of the particle motion for each individual run in determined by step 3 gas flow field using the modified Stokes law. The last one is substantiated in special experiments described below in Chapter 2. The main features of the law are: drag coefficient is $C_D=45/Re$, initial particle velocity is 40 cm/s. The temperature, molar mass, dynamic viscosity and heat capacity of gaseous combustion products were taken from thermodynamics calculations (step 1). The particle diameter and density have been taken from experiment.

The particle trajectories were calculated for the set of varied particle starting points. It was assumed that the residence time of particles in flame (*or* in hot gaseous products of propellant combustion) equals to the time which particle spends passing a distance from its start to the crossing the cone surface that corresponds to initial mixing area (the cone's height equals to L_{mix} calculated in step 2). The procedure is illustrated by sketch in Fig. 1.8. It was found in numerical calculations that the particle velocity has non-zero tangential component. This tangential velocity is directed to the axis when particle moves inside the tube and is directed from the axis when particle leaves the tube. This effect is caused by the gas velocity profile across the tube and it increases with the tube length.
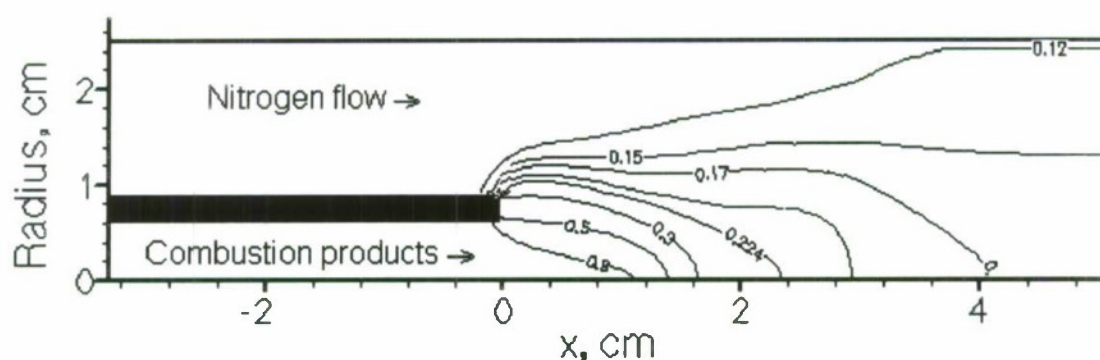
Fig. 1.7. An example of 2D calculation of axially symmetrical gas field by FLOW code in sampling bomb interior. The process of co-axial streams mixing is shown in the form of the lines of equal concentration for combustion products. Black rectangle is the wall of the sample holder and the protective tube having inner radius 0.6 cm and outer radius 0.9 cm.

The combustion gaseous products source surface (left in the picture) is placed at the coordinate $x = -3.62$ cm that corresponds to the sum the depth of the sample holding mounting glass and the length of the protective tube. The open end of protective tube is placed at the coordinate $x = 0$. Radial coordinate $R=2.5$ cm corresponds to the wall of the cylinder 3 in Fig. 1.5.

Another parameter values in this calculation were as follows: pressure = 45.5 atm, burning rate = 2.9 cm/s, and gases parameters

	Nitrogen	Combustion products
Velocity, m/s	0.008	14
Temperature, K	300	3091
Molecular mass	28	24.8
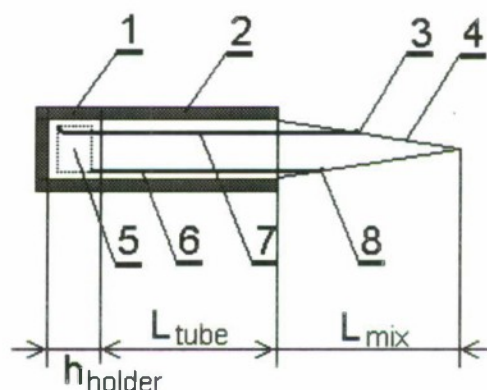
Fig. 1.8. Scheme of determining the residence time as the time for motion from starting point in the bulk of matrix to the cone surface. The trajectories for arbitrary particles A and B are shown.

1	-	mounting glass with sample,	7	-	trajectory of particle A,
2	-	protective tube,	8	-	end point for particle B,
3	-	end point for particle A,	h_{holder}	-	depth of sample holder,
4	-	cone surface,	L_{tube}	-	length of protective tube,
5	-	sample volume containing particles,	L_{mix}	-	initial mixing area.
6	-	trajectory of particle B,			

Typical qualitative results of calculation of the residence time using above mentioned assumptions are presented in Figs. 1.9a, 1.9b, 1.9c for particles that start from different points within the propellant volume. In these figures the starting radius and depth assign the coordinates of starting point. Particle depth is measured from the open end of the protective tube.
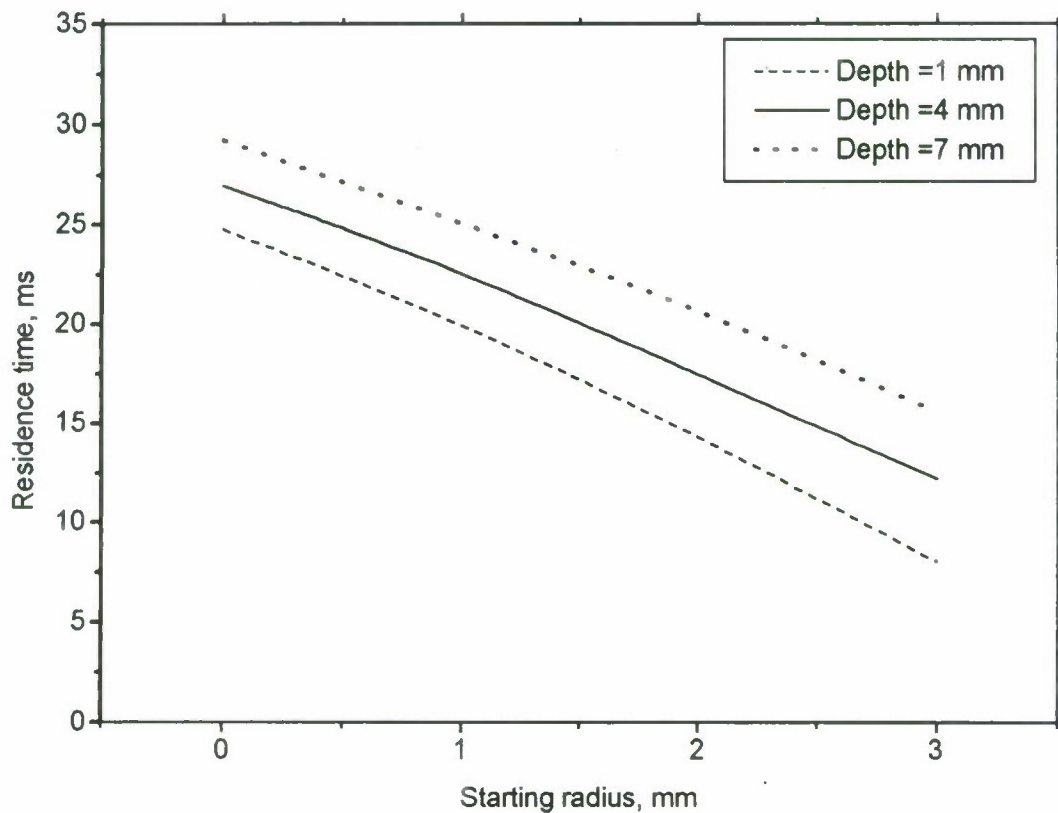
Fig. 1.9a. Calculated residence time for particles started from different points within the propellant volume. Firing geometry type *A*.
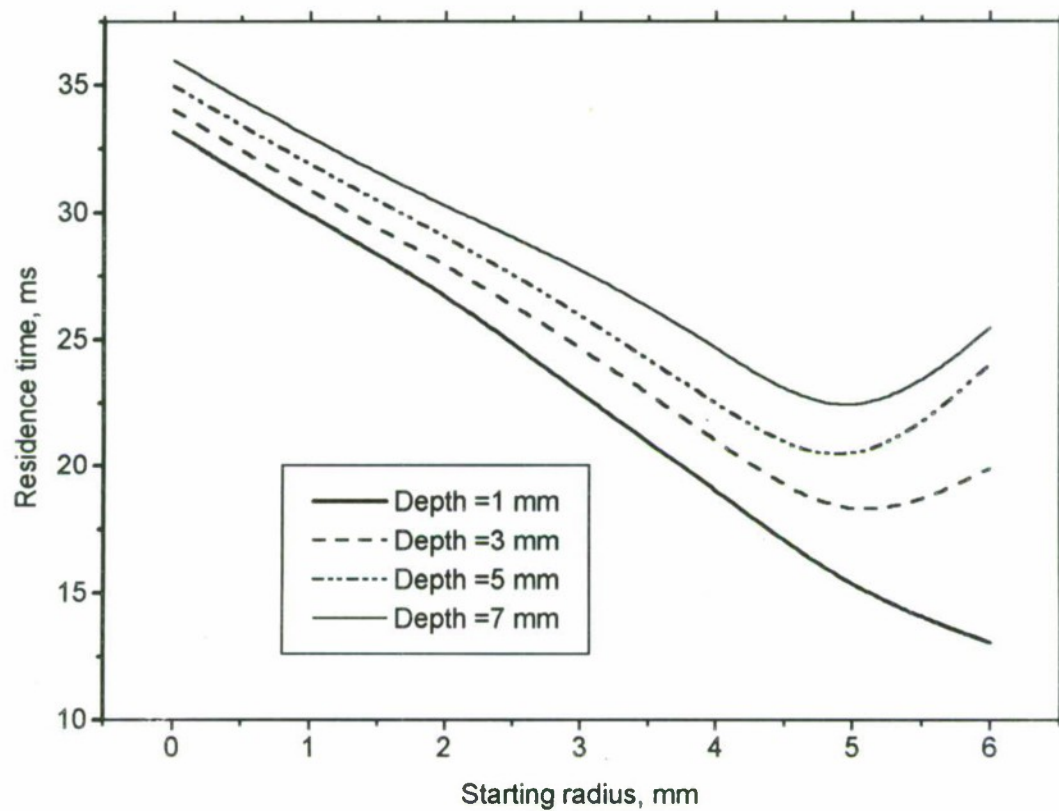
Fig. 1.9b. Calculated residence time for particles started from different points within the propellant volume. Firing geometry type *B*.
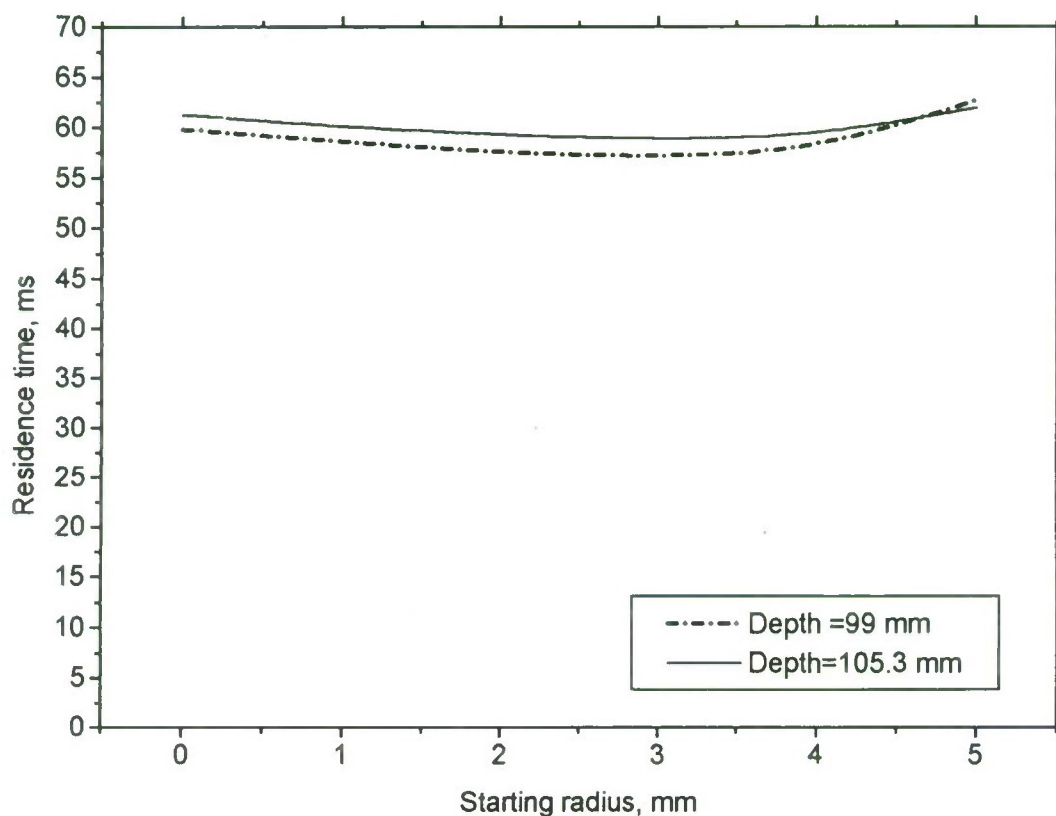
Fig. 1.9c. Calculated residence time for particles started from different points within the propellant volume. Firing geometry type E.

Examining the results of calculations, presented in Figs. 1.9a, 1.9b, and 1.9c, one may conclude that there is difference in residence time for particles starting from different points which is caused by 2D effect. The particles initially located close to the sample holder wall (Fig. 1.9b, starting radius 6 mm) demonstrate very specific motion behavior. In fact, this reason urged us to avoid placing insertions closer than 1 mm to the wall of holder. (Compare with Fig 1.9a, starting radius 3 mm). It is worse to note that in the case of relatively long protective tube (Fig. 1.9c) the particle starting from peripheral radial zone can surpass the particle starting from the lesser depth. But analyzing these results we have to keep in mind the assumptions about constancy of the flow field, localization of the gas source at the bottom of sample holder, etc.

The results of calculations have been generalized by the following formula for mean residence time t_{mean} taking into account the residence time for particles starting from four characteristic points:

$$t_{mean} = [t(R_{min}, h_{min})+2*t(R_{max}, h_{min})+2*t(R_{max}, h_{max})+t(R_{min}, h_{max})]/6, \qquad (1)$$

where $t(R, h)$ is the time for particle started from the point (R, h); R_{min}, R_{max}, h_{min}, and h_{max} are the minimal and maximal value of radius and depth for particle location in the bulk of propellant specimen, respectively. If L_{tube} and R_{tube} are the length and radius of protective tube and h_{holder} the depth of sample holder cylinder, then

$$R_{min} = 0,$$
$$R_{max} = (R_{tube} - 1\ mm),$$
$$h_{min} = (L_{tube} + 1\ mm),$$
$$h_{max} = (L_{tube} + h_{holder} - 1\ mm).$$

The location of these characteristic points are pictured in Fig. 1.10.
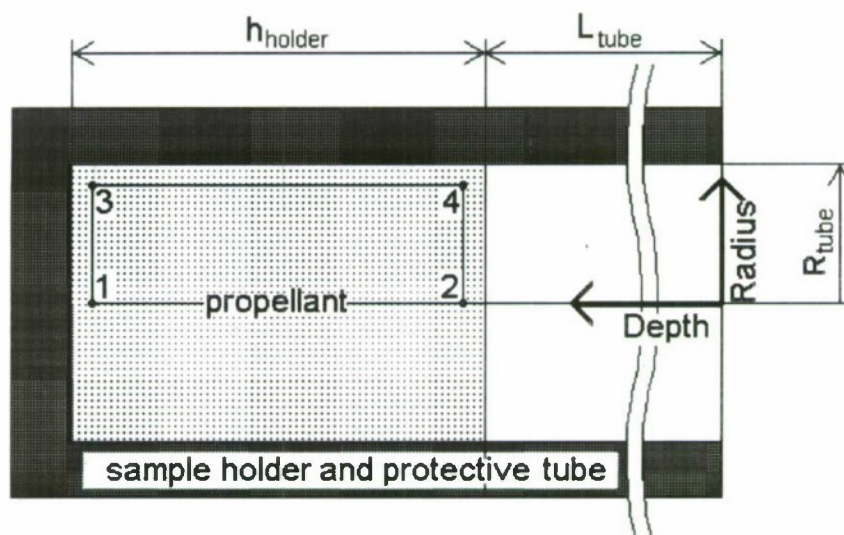
Fig. 1.10. The location of the characteristic points used in averaging procedure of the residence time calculation.

Point No.	Radius	Depth
1	0	$L_{tube}+h_{holder} - 1\ mm$
2	0	$L_{tube} + 1\ mm$
3	$R_{tube} - 1\ mm$	$L_{tube} + 1\ mm$
4	$R_{tube} - 1\ mm$	$L_{tube}+h_{holder} - 1\ mm$

Finally, *Step 5* on residence time calculation is the application of the formula (1) to each test run. Further, when talking about resident time, or simply "time" we will omit the subscript "mean".

1.5. Experimental results

1.5.1. Definitions and designations

The following definitions and designations are used below:

P = pressure;

N = number of cubic metalized inclusions (MI) in sample of super heterogeneous propellant;

m_0 = mean mass of one MI in sample, m_0 = (total mass of MI in sample)$/N$;

$\%Al_0$ = initial mass fraction of aluminum in MI, $\%Al_0 = 42.6\%$;

$\%MI$ = mass content of MI in super heterogeneous propellant sample;

$\%Al$ = mass fraction of unburnt aluminum in sampled agglomerates;

m = mean agglomerate mass, m=(total mass of sampled agglomerates)$/N$;

m_{Al} = mass of unburnt aluminum in sampled agglomerate, $m_{Al} = m \cdot [\%Al/100\%]$;

m_{Al}^0 = initial mass of aluminum in MI, $m_{Al}^0 = m_0 \cdot [\%Al_0/100\%]$;

m_{Al}^b = mass of aluminum consumed (burnt), $m_{Al}^b = m_{Al}^0 - m_{Al}$;

η = incompleteness of aluminum combustion, $\eta = m_{Al} / m_{Al}^0$;

$\xi = 1-\eta$ - efficiency of aluminum combustion or aluminum depletion degree or extent of aluminum conversion, $\xi = (m_{Al}^0 - m_{Al}) / m_{Al}^0 = m_{Al}^b / m_{Al}^0$;

m_{ox}^{full} = theoretical mass of oxide provided that the whole aluminum initially contained in MI has burnt out, $m_{ox}^{full} = (100/54) \cdot m_{Al}^0$;

m_{ox}^{exp} = expected mass of oxide forming in course of combustion of mass of aluminum m_{Al}^b, $m_{ox}^{exp} = (100/54) \cdot m_{Al}^b$;

m_{ox}^{ag} = mass of oxide in agglomerate, $m_{ox}^{ag} = m - m_{Al}$;

φ = mass fraction of oxide deposited on agglomerate, $\varphi = m_{ox}^{ag} / m_{ox}^{exp}$;

χ = relative mass of oxide, ratio of mass of oxide formed in combustion and theoretical oxide mass, $\chi = m_{ox}^{exp} / m_{ox}^{full}$. $\chi = \chi^{out} + \chi^{back}$, where:

χ^{out} = relative mass of oxide that left the agglomerate, $\chi^{out} = (m_{ox}^{exp} - m_{ox}^{ag}) / m_{ox}^{full}$;

χ^{back} = relative mass of oxide that is accumulated on agglomerate, $\chi^{back} = m_{ox}^{ag} / m_{ox}^{full}$;

D_{mn} = characteristic mean diameter of sampled agglomerates.

ρ = density of agglomerate.

$t = t_{mean}$ = calculated residence time of agglomerates in combustion products before extinction.

Experimental results are summarized in Table 1.3 which contain data on combustion conditions (pressure P and geometry type that includes diameter and length of protective tube and sample mounting holder depth, see Fig. 1.6), the propellant specimen formulation specification (m_0, N, $\%MI$), sampled agglomerate characteristics (D_{mn}, ρ, $\%Al$, η, φ), and calculated residence time for agglomerates burning in combustion products (t).

Additionally, the dependence of burning rate on pressure is presented in Fig. 1.11. The burning rate values were measured directly in sampling experiments.

17
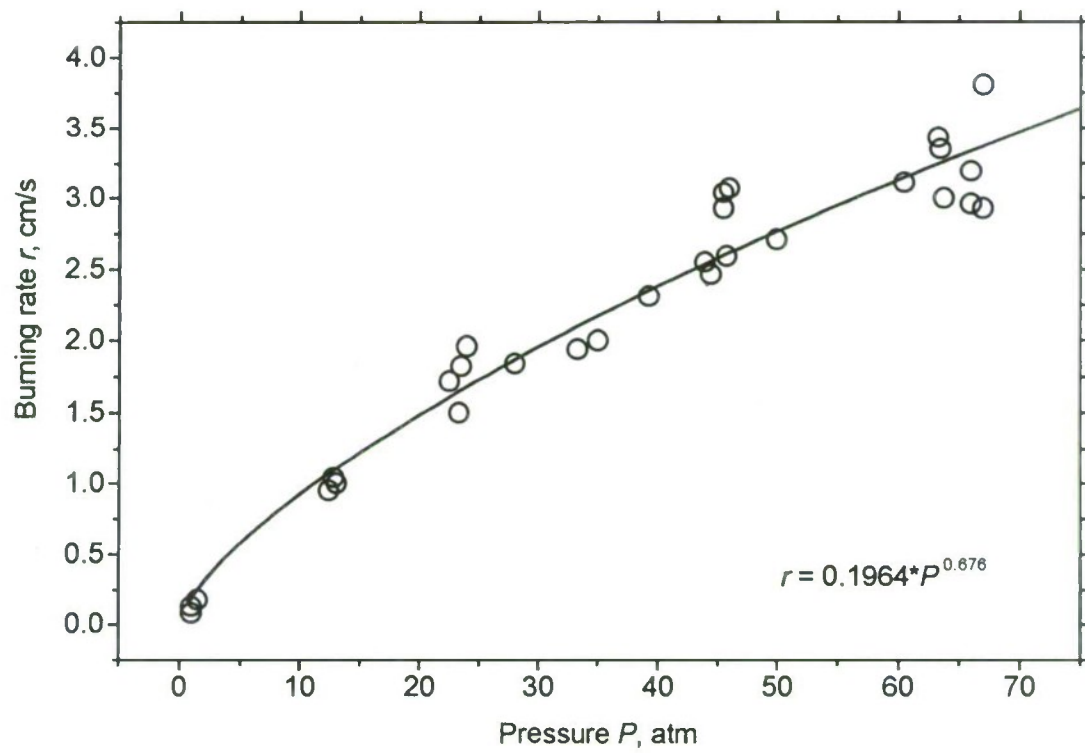
Fig. 1.11. Dependence of burning rate of heterogeneous propellant on pressure.

Table 1.3. Experimental conditions and main results

Run Id	Geom type	P, atm	m_0, mg	N	%MI	m, mg	%Al	η	D_{10}, μm	D_{43}, μm	ρ, g/cm³	φ	t, ms
1670	D	45.8	21.08	120	1.6	13.46	33.4	0.2483	468	473	2.48	0.825	59.0
1667	E	66	22.95	100	1.5	13.72	19.7	0.2502	462	467	2.63	0.690	85.2
1669	C	67	20.29	120	1.5	13.50	20.5	0.2872	464	469	2.55	0.800	43.2
1622	C	45.5	34.82	85	1.8	18.75	27.5	0.2988	521	527	2.5	0.611	42.4
1668	D	66	22.17	120	1.7	14.10	24.0	0.3253	471	478	2.54	0.768	62.4
1623	E	39.3	30.71	85	1.6	16.81	31.8	0.3685	503	512	2.48	0.634	80.4
1621	E	50	29.88	85	1.6	16.28	33.6	0.3724	505	512	2.38	0.632	82.8
1620	B	60.5	27.65	85	1.5	18.06	32.4	0.4093	500	503	2.75	0.852	22.1
1624	B	35	30.41	85	1.6	15.06	39.0	0.411	487	493	2.46	0.546	78.9
1380	C	1	30.63	80	1.5	12.09	55.4	0.4504	459	466	2.35	0.349	61.8
1617	A	63.5	30.57	70	3.2	17.97	40.4	0.5152	515	520	2.48	0.746	17.2
1625	E	28	19.30	100	1.2	11.49	40.5	0.5263	445	454	2.44	0.766	72.2
1660	E	13	36.78	90	2.1	16.41	54.9	0.5267	496	503	2.53	0.442	76.0
1338	B	46	45.20	100	2.9	24.72	47.2	0.5312	543	565	2.83	0.671	19.3
1659	D	23.3	37.75	120	2.8	19.22	50.4	0.5451	536	541	2.36	0.583	67.0
1662	C	12.4	32.72	90	1.9	14.88	51.2	0.5503	494	500	2.33	0.464	37.6
1618	A	63.8	33.36	70	3.3	21.48	44.4	0.5514	540	553	2.54	0.947	17.8
1616	A	63.3	26.57	70	3.0	15.78	42.1	0.5607	490	501	2.5	0.771	15.8
1661	D	13	32.22	90	1.8	16.56	51.9	0.5747	490	495	2.66	0.597	60.8
1374	B	23.5	27.50	64	1.1	15.10	52.0	0.5865	491	497	2.41	0.696	18.5
1378	B	12.8	41.63	80	2.1	21.91	56.3	0.6097	539	552	2.61	0.642	20.1
1376	B	12.8	40.69	80	2.0	20.40	61.4	0.6332	539	547	2.45	0.575	19.8
1375	A	22.5	30.75	67	2.4	17.01	57.0	0.6493	504	510	2.5	0.738	19.4
1665	D	1	27.11	90	1.5	12.89	59.1	0.6662	462	474	2.43	0.502	21.2
1379	B	1.5	15.38	160	1.6	7.74	64.6	0.6691	395	404	2.35	0.587	15.9
1666	C	1	25.90	100	1.7	13.72	61.3	0.6865	473	473	2.52	0.673	16.7
1663	A	5.4	40.17	90	4.8	19.79	60.4	0.6881	542	548	2.31	0.548	13.7

The experimental data available can be treated from the point of view of consumption kinetics of metal that is important for calculation of total heat release in combustion. Another point of interest is mass (size) kinetics of burning agglomerates which is important for slag formation in solid rocket motors. Both aspects are analyzed on the basis of data reported in Table 1.3.

1.5.2. Kinetics of metal consumption

Experimentally determined mass of unburnt aluminum in sampled agglomerates gives a measure for combustion incompleteness determined as the ratio of mass of free aluminum in agglomerates and mass of initially stored aluminum in specimen: $\eta = m_{Al}/m^0_{Al}$. In our experiments this can be varied mainly by pressure and agglomerate residence time. The composition of combustion products is determined by the formulation of non-metalized matrix. Indeed, the mass fracture of insertions (%MI) did not exceed 3.5%. Therefore the mass content of oxidizing species was kept at the same level during firing of individual agglomerates. The parameters of gaseous combustion products (temperature, specific heat, molar mass) were calculated on the basis of thermodynamics. Additionally, the partial consumption of plexiglas (PMMA) based protective tube and specimen holder (made also of plexiglas) was taken into account.

When treating experimental data, we neglect usually size distribution of agglomerates. Real variation of sampled agglomerate size and density was in the range $D_{10} = 400 \div 540$ μm and $\rho = 2.3 \div 2.8$ g/cm³. However, calculation of residence time of agglomerates was made based on real size and density of individual particles.

Figure 1.12 represents dependencies of aluminum combustion incompleteness on agglomerate residence time at different pressures. For the sake of simplicity, all data are divided into 4 groups: in the pressure ranges 1-7, 16-28, 29-56, and >56 atm.

It is seen that in particular pressure range the aluminum combustion incompleteness decreases with residence time for agglomerates. Besides, combustion incompleteness decreases with pressure in the pressure range 15-80 atm. However, the data obtained at lower pressures (1-7 atm) exhibit some different behavior, which is analyzed below.

The estimate for reproducibility of experimental data on aluminum combustion incompleteness can be made by examination of 3 experimental points circled at the left hand side curve of $\eta(t)$ dependence for pressure range >56 atm, Fig. 1.12. The experiments (runs 1616, 1617, 1618) were conducted under similar conditions (geometry type A, $N=70$) and the following variation of the parameters was realized, (see Table 1.3): $P = 63.3 \div 63.8$ atm, %MI = $3.0 \div 3.2$%, $m_0 = 27 \div 33$ mg, $m = 16 \div 22$ mg, %Al = $40.4 \div 44.4$%, $\eta = 0.52 \div 0.56$, $D_{10} = 490 \div 540$ μm, $\rho = 2.48 \div 2.54$ g/cm³, $\varphi = 0.75 \div 0.95$, $t = 15.8 \div 17.8$ ms.

Note that instrumental error of determining the mass of unburnt aluminum in agglomerates, when using permanganatometric method [4], amounts ~15 relative percent, another typical errors are $\Delta D \sim 15 \div 30$ μm, $\Delta \rho \sim 0.2 \div 0.3$ g/cm³.

Analysis of experimental results for pressure range 15-80 atm allows to construct approximate expression for η in dependence of t and P:

$$\eta(t, P) = A \cdot t^b \cdot P^c$$

Matching with experimental data gives the following values for coefficients:

$$
\begin{aligned}
A &= 2.86, \\
b &= -0.28, \\
c &= -0.20.
\end{aligned}
$$

Function $\eta = \eta(t, P)$ is presented as a surface in 3D space in Fig. 1.13 while experimental points and equal level lines are presented in Fig. 1.15. Based on examination of significant number of experimental data it is possible to treat correlation for $\eta(t, P)$ as universal for formulation studied and use it to calculate η at arbitrary magnitude of parameters P and t. At the same time it is worth to note that the above correlation does not work at low pressures (1-7 atm).

There are several reasons for specific combustion behavior of metal at low pressures. First of all, one has to take into consideration the fact that the temperature of the burning surface depends on pressure. At low pressure estimated temperature of the burning surface does not exceed 450÷550°C which is considerably lower than the melting point of aluminum (660°C). This gives one of the possible explanations for sometimes observed in video registration an ejection of non-ignited MI. Their ignition occurred at the distance of 5÷8 mm far from the burning surface. A few of non-ignited MI were detected in sampled condensed combustion products (see Fig. 1.14). These were characterized by rectangular shape with smoothed melted edges. Non-ignited MI can be easily destroyed by slight pressing with needle that means that they have not established metal bridges. At the same time, relatively small value of aluminum combustion incompleteness at lowest pressures can be owed to relatively large residence time of agglomerates on the burning surface and relatively high mass exchange rate due to large velocity difference between burning agglomerate and combustion products gas flow. It is known that for propellant under study the velocity of gases issued from the burning surface at low pressures is higher than that at high pressures (by approximately twice in pressure range 1÷70 atm).
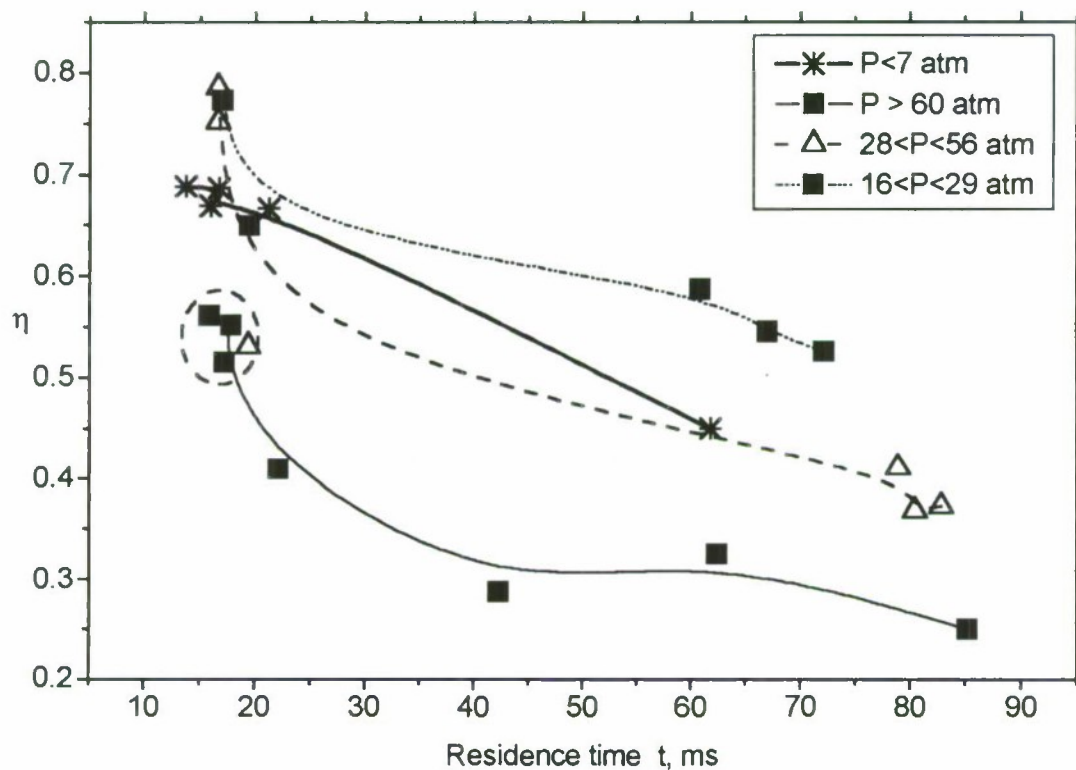
Fig. 1.12.

The dependencies of aluminum combustion incompleteness on agglomerate residence time at different pressures. The data are divided into 4 groups corresponding to four pressure ranges.

Three black square points in the oval corresponding to runs 1616, 1617, and 1618 are obtained under similar experimental conditions, see Table 1.3.
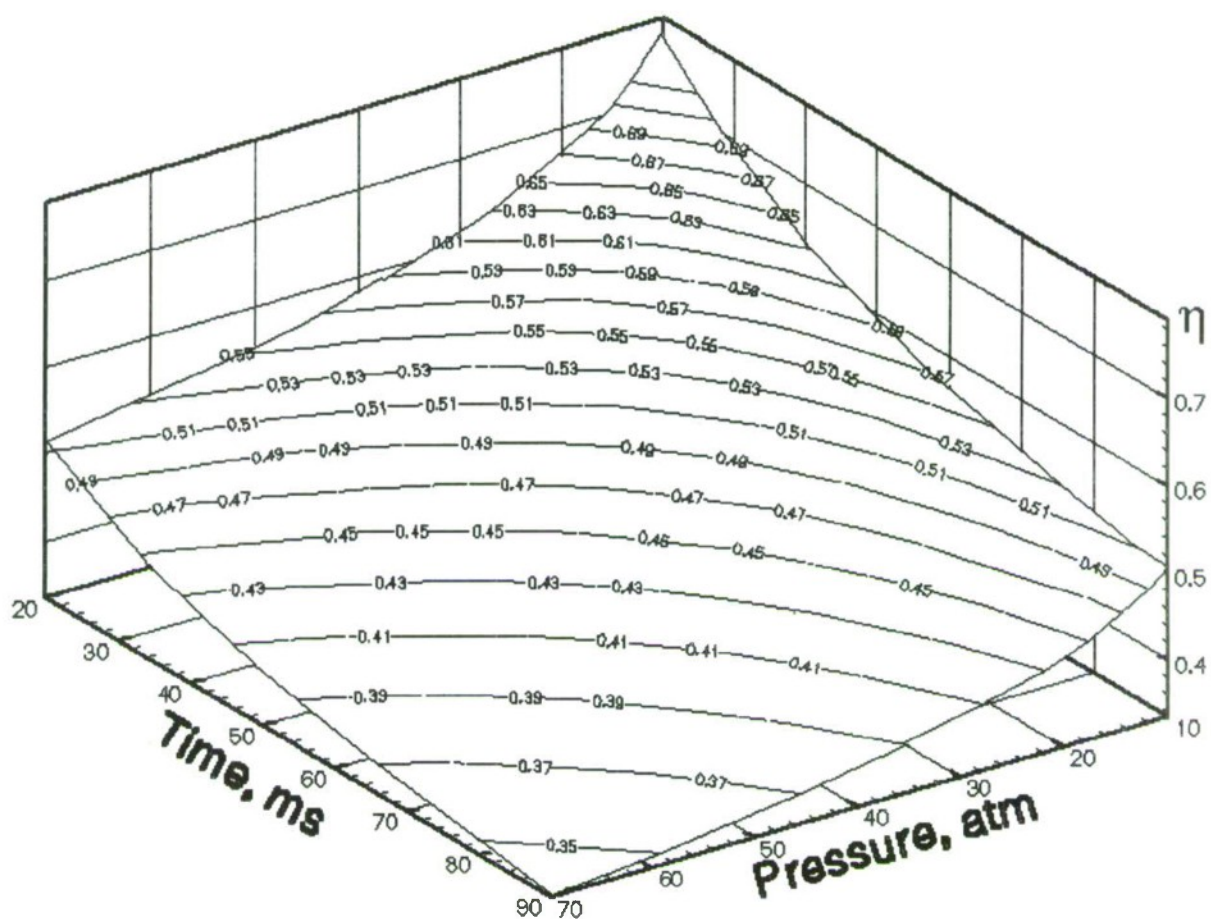
Fig. 1.13.
Dependence of incompleteness of aluminum combustion on pressure and residence time:
3D view of approximating function

$$\eta(t, P) = A \cdot t^b \cdot P^c$$
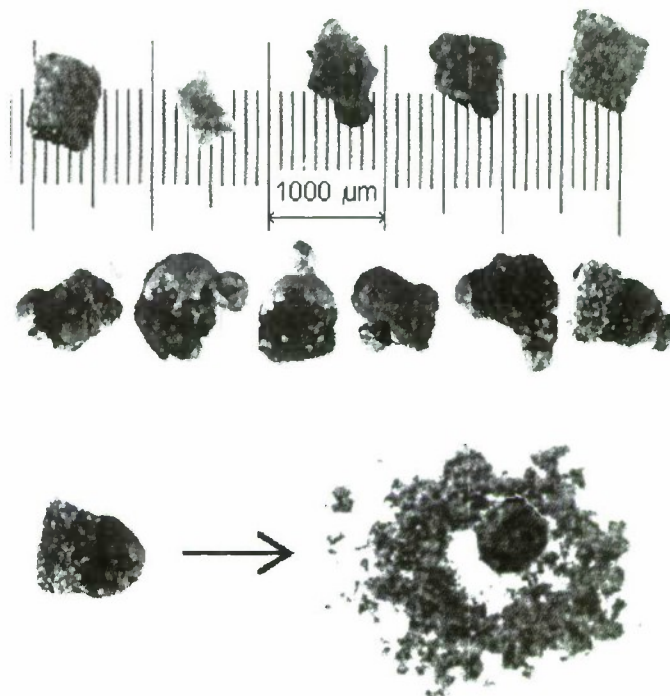
Fig. 1.14.
Accumulated over several experiments non-ignited and partially ignited metalized inclusions.

Upper line: shape of sampled particles is similar to original one. For two particles one can see the rounded melted edge.

Middle line: approximately one half of particle looks like initial cube, another half looks like an agglomerate (fused and round shaped).

Bottom line: semi melted particle before and after crash by slight touch.
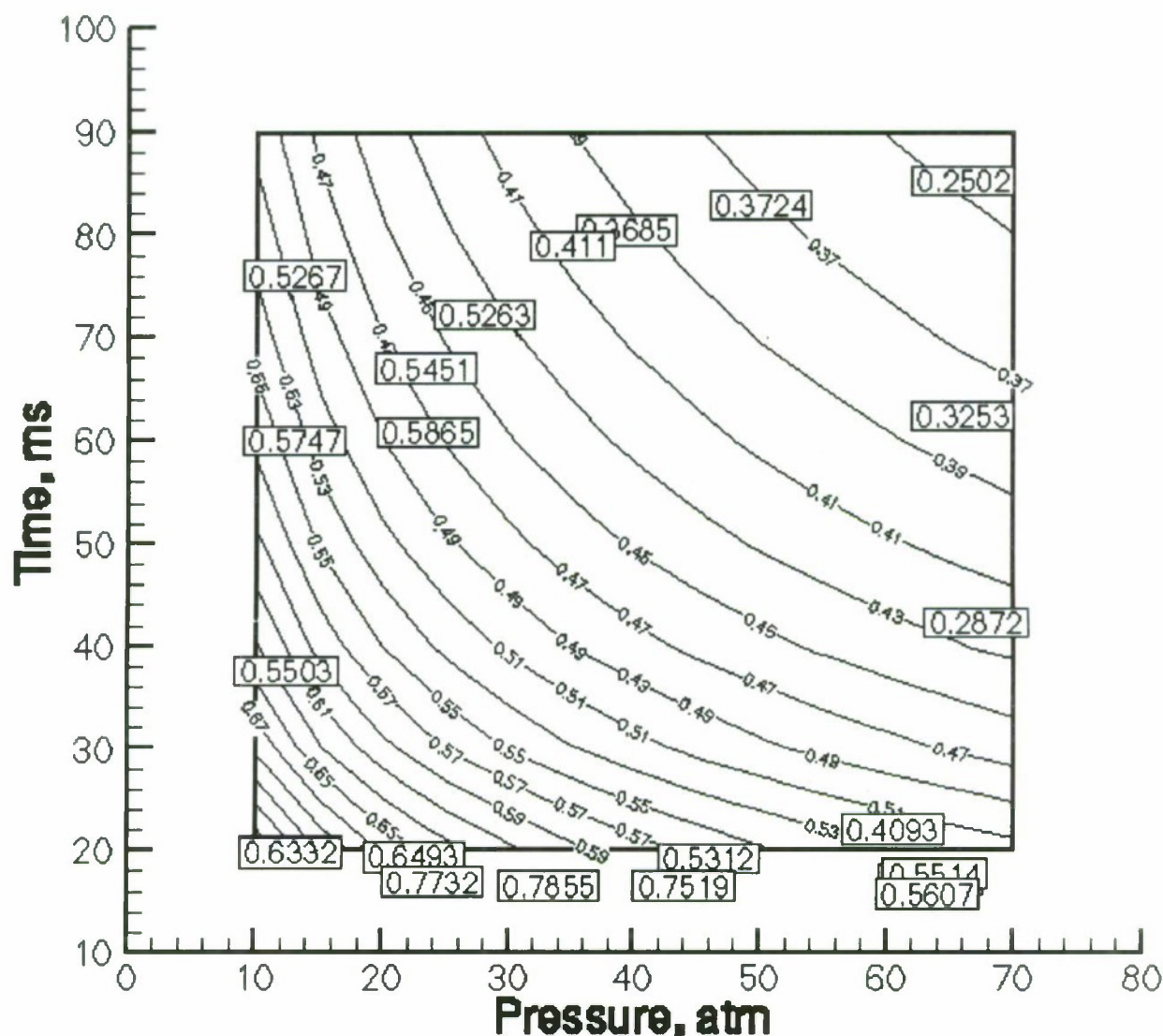
Fig. 1.15.

Dependence of incompleteness of aluminum combustion on pressure and residence time.

The calculated isolines (or equal level lines $\eta = const$ for function $\eta = \eta(t, P)$ presented as surface in 3D space in Fig. 1.13) and experimental points (rectangles). The point's location on the plane corresponds to values of t and P, the measured value of η is shown inside the rectangle. To be punctual, the point location is on the crossing the rectangle diagonals.

1.5.3. Evolution of agglomerate mass in time.

One of the principal problems in mathematical modeling of combustion of metal agglomerate is accumulation of oxide on the surface of burning particle. This is important feature of the process under investigation because it determines temporal evolution of agglomerate mass that allows to calculate velocity field of agglomerates and slag formation in rocket motor chamber. There are several questions which still have no clear answer:

- What is the law of agglomerate mass time evolution (increase, decrease, or neutral form)?
- How is deposited oxide distributed over agglomerate particle surface?
- Is it possible for metal combustion to cease due to accumulation of large portion of oxide?

Obviously, experimental data the only may give answers on those questions. The analysis of results obtained in experiments with well characterized and strictly controlled conditions is helpful in this respect. Figure 1.16 presents a dependence of oxide fraction φ deposited on agglomerate versus magnitude of completeness of aluminum combustion ξ. It is seen that the amount of deposited oxide is relatively high and is in the range $0.4 \div 0.85$ (compare with theoretical value of $0.1 \div 0.3$ reported in [7, 8]). There is observed moderate rise of φ with degree of metal consumption.

The dependence of deposited oxide fraction on pressure is presented in Fig. 1.17. It is clearly seen that this fraction increases with pressure that correlates with experimentally observed [9] behavior of φ. Unfortunately, there are no more available data in the literature on $\varphi(P)$ dependence. It should be mentioned, however, that the data [9] were obtained in different experimental conditions: under microgravity and with combustion of large aluminum particles in model oxidizing media (mixture $O_2 + N_2$, mixture $O_2 + Ar$, and CO_2). Therefore, detailed comparison with data [9] can not be performed.

Figure 1.18 presents dependence of density of agglomerates on content of unburnt aluminum in agglomerate. It is seen that density increases when amount of unburnt aluminum decreases. Maximal density obtained by extrapolation to zero the content of aluminum equals to 2.76 g/cm^3. Suprisingly that this value correlates well with that determined under microgravity conditions in [9].

Fig. 1.19 presents the agglomerate mass dependence on the extent of the aluminum conversion. The mass dynamic is described by the value m/m_0, where m is the mean mass of sampled agglomerate, m_0 is the mean initial mass of MI before combustion. Linear fitting the data being extrapolated to minimal degree of metal conversion ($\xi=0$) gives the value $m/m_0=0.46$ that equal to initial aluminum content in propellant for MI (46.2%). In another words, the agglomerate mass slightly increases with extent of the aluminum conversion and its evolution starts from $m=0.46 \cdot m_0$ (approximately half of mass of original MI) but not from $m=m_0$. This was confirmed by weighing the mass of a very few non-ignited MI sampled in combustion at low pressures. These facts show that original MI are subjected in combustion wave first to pyrolysis of energetic binder and fine AP particles (like as volatile components release from coal) and then aluminum particles start to merge, melt and ignite. Melting of aluminum and formation of global agglomerate takes finite time interval. That is why non-ignited MI particles even after passing through the flame can be easily divided by slight pressing, see Fig. 1.14.

The number of data obtained allows to analyze in detail the dependencies of oxide flows from and to the original agglomerate. It was already mentioned that the total mass of agglomerate in conditions of our experiments increases with extent of metal conversion (Fig. 1.19) due to oxide accumulation. At the same time it is well known [10, 11] that for most propellants the mass of

smoke oxide (or dispersed oxide particles in gas flow surrounding the agglomerates) increases with aluminum combustion completeness, for example, with pressure. Does this fact contradict the observed behavior of the fraction of oxide deposited on agglomerate with aluminum conversion extent $\varphi(\xi)$? The answer is "no". Figure 1.20 shows that both amounts of aluminum oxide – accumulated on agglomerate surface ("back") and leaving the surface ("out") – increase with extent of aluminum conversion. However, the dependence for deposited oxide fraction is steeper that leads to observed positive dependence of total mass of agglomerate on aluminum conversion degree.
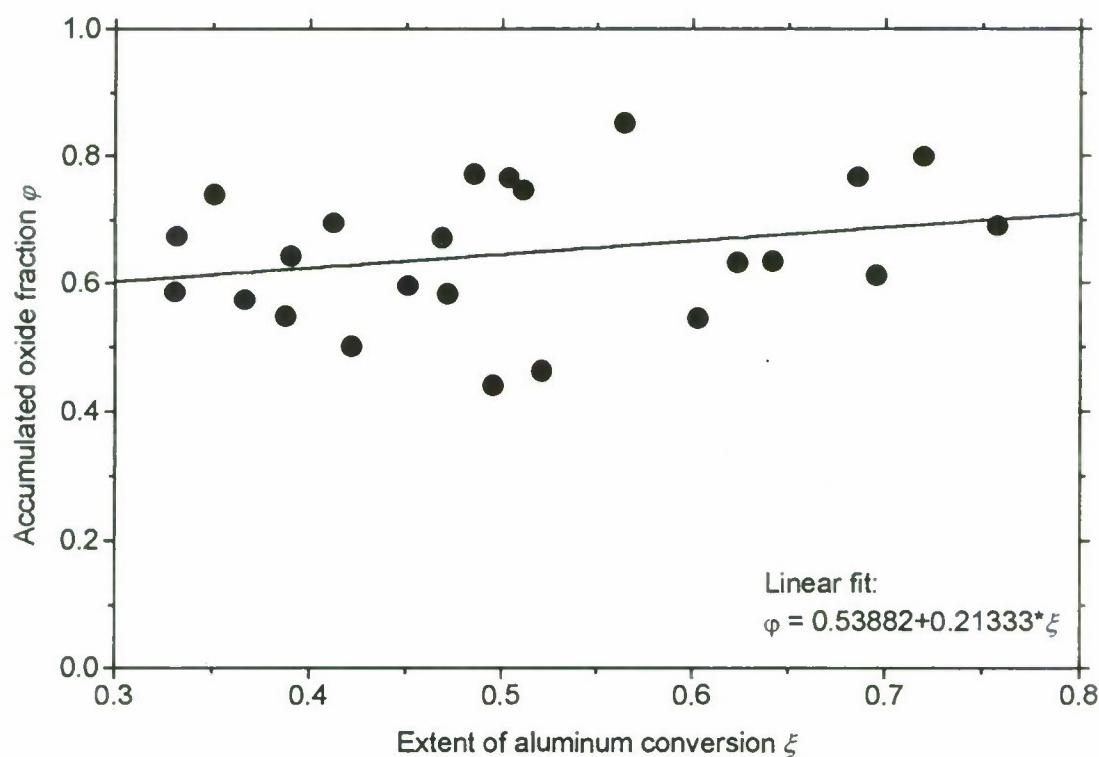
Fig. 1.16.
Mass fraction of formed oxide accumulated on the burning agglomerate *vs* aluminum combustion completeness.
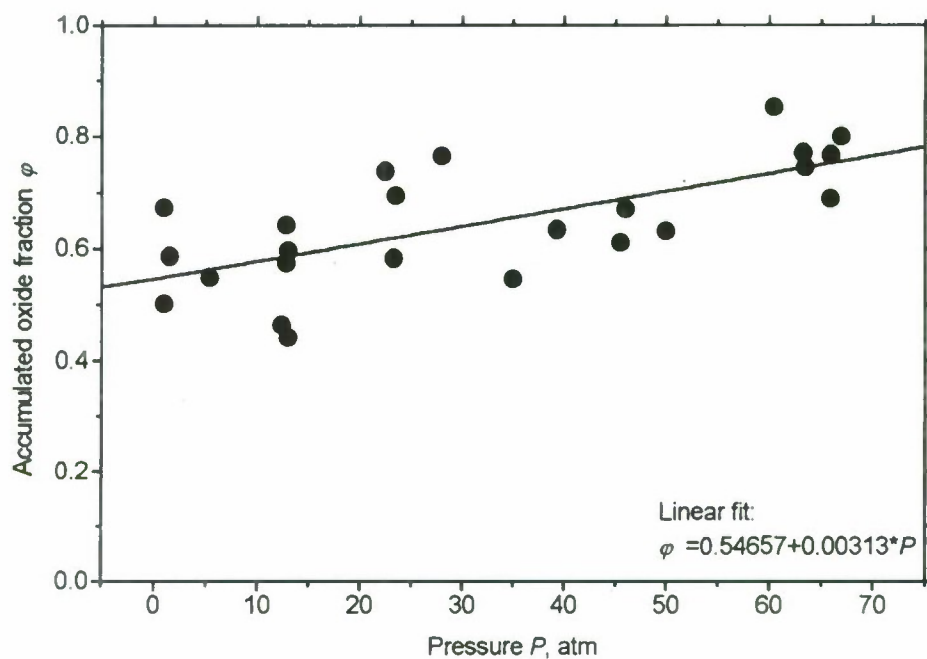
Fig. 1.17. Mass fraction of formed oxide that was accumulated on burning agglomerate. The dependence on pressure.
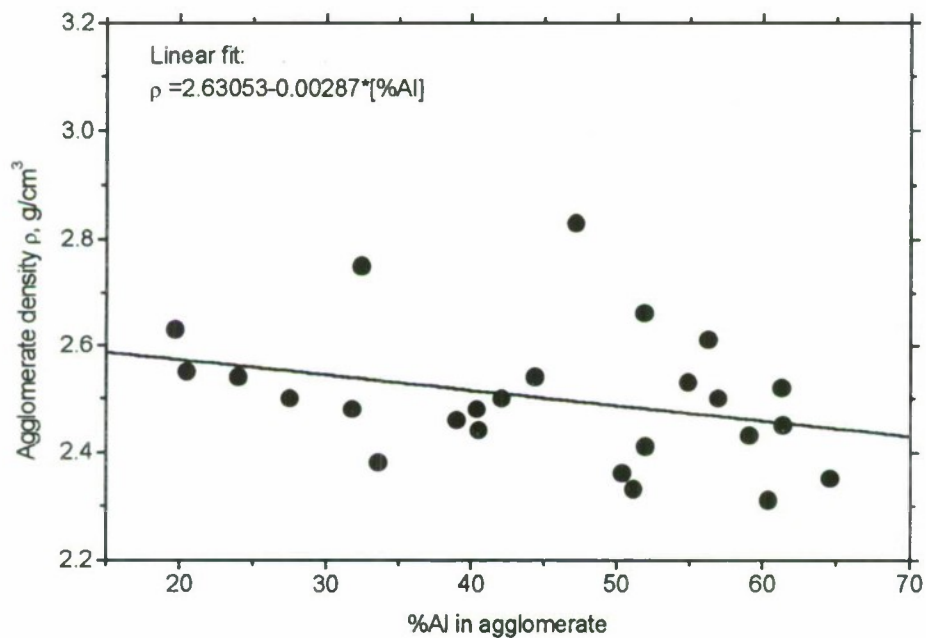
Fig. 1.18. The dependence of agglomerate density on free aluminum content in agglomerates.

28
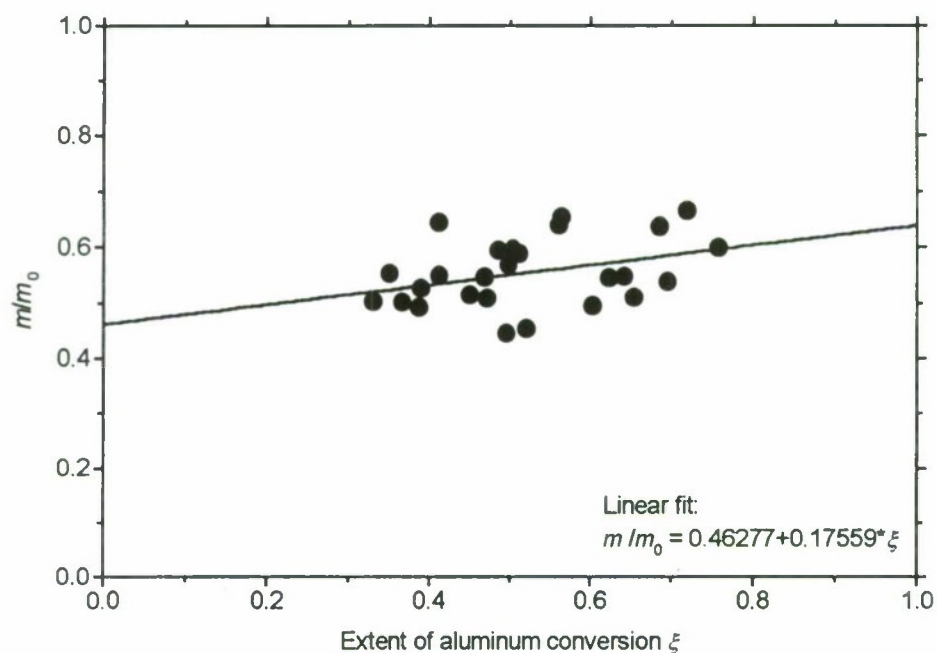
Fig. 1.19. Agglomerate mass dependence on aluminum combustion completeness.
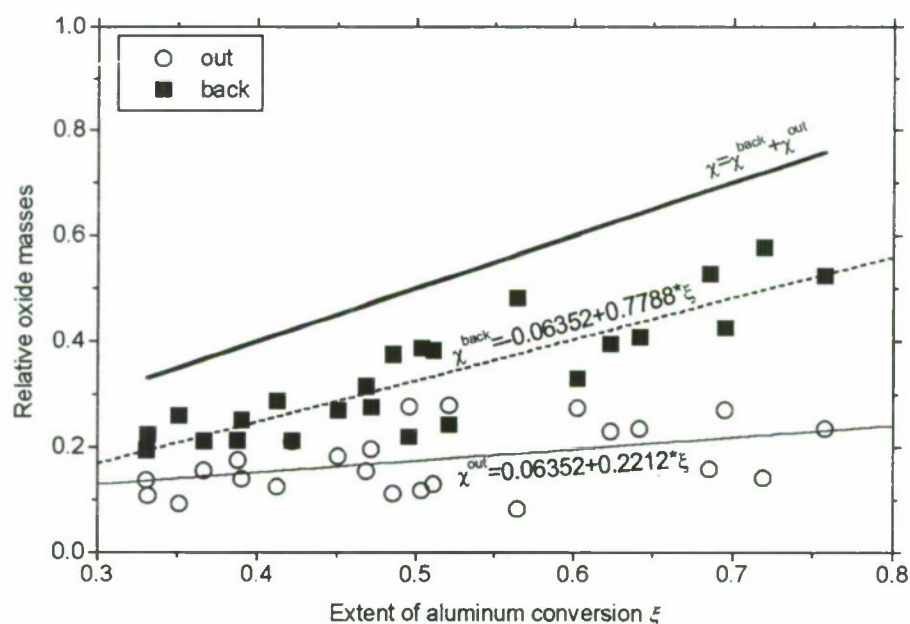
Fig. 1.20. Relative masses of oxide vs aluminum combustion completeness.
χ^{out} - relative mass of oxide that left the agglomerate,
χ^{back} - relative mass of oxide accumulated on agglomerate,
$\chi = \chi^{out} + \chi^{back}$ - total relative oxide mass.

2. STUDYING THE MOTION OF THE BURNING AGGLOMERATES.

2.1. Background

Development of realistic mathematical model of metal agglomerate evolution has to be based both on the laws of agglomerate combustion and motion in combustion products of solid propellant [12].

One of determining parameters of particle motion in two phase flow is a drag coefficient, C_D. It plays important role in calculation of particle velocity according to kinematics law (vertical motion):

$$\frac{dV}{dt} = C_D \frac{Re}{24} \frac{18\mu}{\rho_p d^2} (V_g - V) \pm g. \qquad (2.1)$$

Here d is the diameter of particle; V and V_g are the velocities of particle and gas, respectively; ρ_p and ρ_g are the densities of particles and gas, respectively; μ is the gas viscosity; g is the gravity acceleration; $Re = \rho_g d |V_g - V|/\mu$ is the Reynolds number. Sign "+" is chosen in Eq. (2.1) when direction of vectors of particle velocity and gravity force coincide.

Note that burning agglomerates move in combustion chamber with Re in the range $1\div500$. It is usual to express C_D as a function of Re, $C_D = f(Re)$. In particular, in case of small Re there is the Stokes law in the form $C_D = 24/Re$.

In the literature, there are numerous formulas for $C_D(Re)$ depending on the value of Re. Several examples of such formulae are presented below. Most of them, except last two ones, correspond to the motion of inert spherical particle in isothermic conditions.

$$C_D = \frac{24}{Re}\left[1 + \frac{\sqrt{Re}}{6}\left(1 + \frac{\sqrt{Re}}{10}\right)\right] \qquad [13],$$

$$C_D = \frac{24}{Re}\left(1 + 0.179\sqrt{Re} + 0.013Re\right) \qquad [15],$$

$$C_D = \frac{24}{Re} + \frac{4}{\sqrt[3]{Re}}, \quad 3 < Re < 400 \qquad [16, 17],$$

$$C_D = \frac{24}{Re}\left(1 + 0.125Re^{0.72}\right) \qquad [18],$$

$$C_D = \frac{24}{Re}(1 + 0.1935Re^{0.6305}), \quad 20 < Re < 260 \quad [19],$$

$$C_D = \frac{24}{Re}(1 + 0.15Re^{0.687}), \quad Re < 800 \quad [14, 20, 21],$$

$$C_D = \begin{cases} 28 Re^{-0.85}, & Re < 10 \\ 12.5 Re^{-0.5}, & 10 < Re < 1000 \end{cases} \qquad [22],$$

$$C_D = \begin{cases} 27 / Re^{0.84}, & Re \le 80 \\ 0.271 Re^{0.217}, & 80 < Re < 10^4 \end{cases} \qquad [23 - 27],$$

$$C_D = \begin{cases} 52 / Re, & Re \le 50, \\ 2 / Re^{0.2}, & Re > 50 \end{cases} \qquad [28, 29].$$

In the paper of American researchers [30] the coefficient of drag in the burning particle was assumed to be approximately 2.5 times the value for a non-burning particle with the same Reynolds number. More detailed description of C_D for burning (liquid) particles is given in [12, 21, 31]. For reacting liquid droplets, the drag coefficient needs to be modified in order to take account of combustion. The modified drag coefficient C_D^* is given by $C_D^* = C_D/(1+B)$ [10], where C_D is the drag coefficient for solid spherical nonreacting particle and B is the transfer number [12, 21, 31]. For a unity Lewis number ($Le = 1$), this transfer number is given by

$$B = \frac{\Delta H f_e Y_{O,\infty} + c_g (T_\infty - T_B)}{L + c_p (T_B - T_R)} \, ,$$

where ΔH is the droplet heat of combustion, f_e is the coefficient describing the stoichiometric chemical reaction between fuel and oxygen (f_e grams of fuel + 1 gram of oxygen → $(1 + f_e)$ grams of products), $Y_{O,\infty}$ is the oxygen mass fraction of the oxidant (for air, $Y_{O,\infty} = 0.233$), c_g and c_p are the mean specific heats of the gas and the droplet, respectively, T_∞, T_B, and T_R are the gas, the liquid boiling, and the liquid reference temperatures, respectively, and L is the latent heat of vaporization. Values of f_e and B are tabulated for several liquid fuels burning in air, assuming $T_\infty = T_R = 20^0C$ and $c_g = 0.31 cal/(g \cdot K)$ [31]. For simple evaporation without combustion, the first term in the numerator on the right-hand side of equation for B equals zero.

Note that these results were obtained in experiments with burning drops of liquid hydrocarbon fuels [12, 21, 31, 32]. Similar conclusion on reducing the drag coefficient in the case of reacting liquid particles was made on the basis of theoretical simulation [33].

However, in experiments with burning coal particles [28, 29], it was established enhanced value of drag coefficient in the form $C_D = 52/Re$, where gas viscosity is calculated at the particle surface temperature.

Thus, one may conclude that there is no ubique recommendation in the literature how to evaluate C_D for reacting particle. Therefore the experimental determination of C_D for burning agglomerates under moderate Reynolds number (1÷500) corresponding combustion of real propellants in solid motors is actual problem.

2.2. Experimental.

The motion of monodisperse agglomerates of aluminum in flame of non-metalized propellant (see Chapter 1) was studied by video recording using technical CCD camera "Chiper" (Taiwan). A set of color filters was used in order to reduce self-illumination of flame at wavelength exceeding 390 nm. The optical scheme is shown in Fig. 2.1. Mechanical modulator in the form of slotted disc provided intermitted registration of burning particle with frequency 320 Hz (exposure time 0.5 ms). The visualized field of view having dimensions of 21×16 mm^2 was localized at the flush of the sample holder quartz tube that simultaneously played the role of inhibiting layer of propellant sample. Thus, the recorded particle trajectories were inside the flow core of gaseous combustion products without mixing with ambient gas. Example of video record of burning particle is presented in Fig. 2.2. The distance between neighbor particle images gives value of actual velocity of particle.
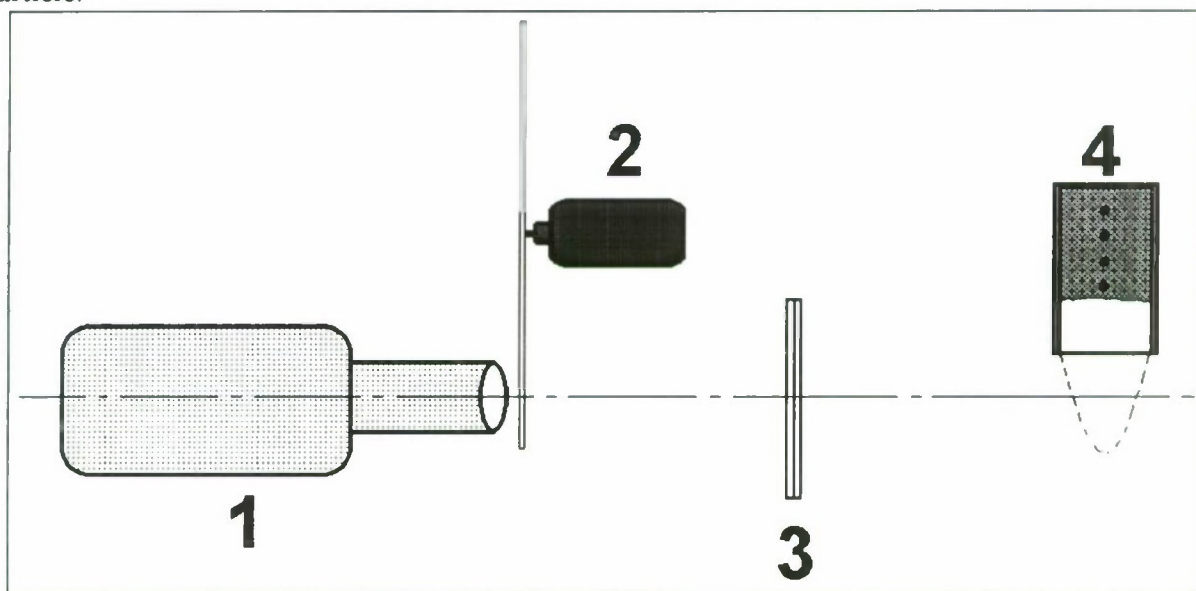
Fig. 2.1. Optical scheme for visualization of burning agglomerates:
1 - CCD-video camera,
2 - mechanical modulator,
3 - set of optical glass filters,
4 - propellant sample (flame directed downward).

For these experiments special model propellant samples were manufactured. Schematic sketch of their structure is shown in Fig. 2.3. Main part of a sample consists of non-metalized propellant matrix based on fine AP, HMX and energetic binder (see the propellant formulation in detail in Section 1.2). Along axis of sample the special insertion plate is mounted. It consists of cured non-metalized matrix with inclusions of highly metalized propellant simulating material of "pockets" in real propellant. The coordinates of these inclusions were used in further calculations. On the top of protruding insertion plate a reference mark (hole) was made that allowed to evaluate distance for each inclusion in the bulk of sample.
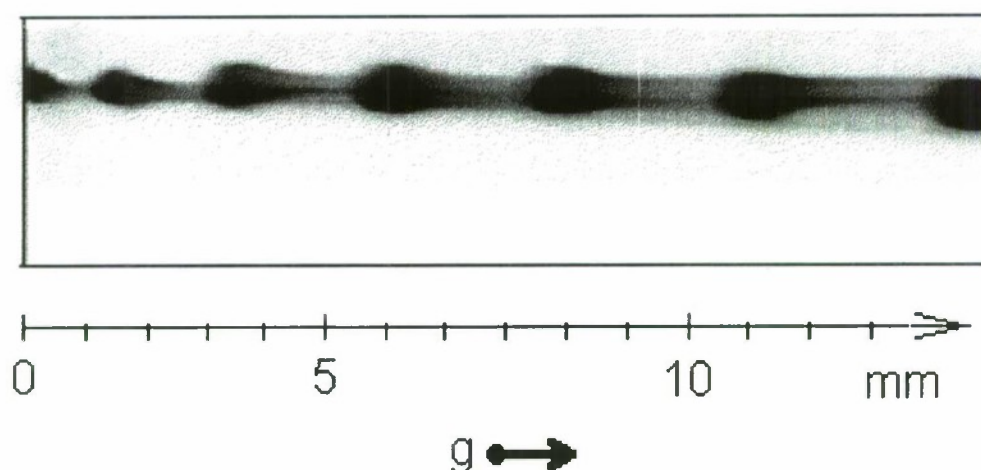
Fig. 2.2. Video record of agglomerate trajectory in flame (modulation frequency 320 Hz, exposure time 0.5 ms). **g** stands for gravity vector.
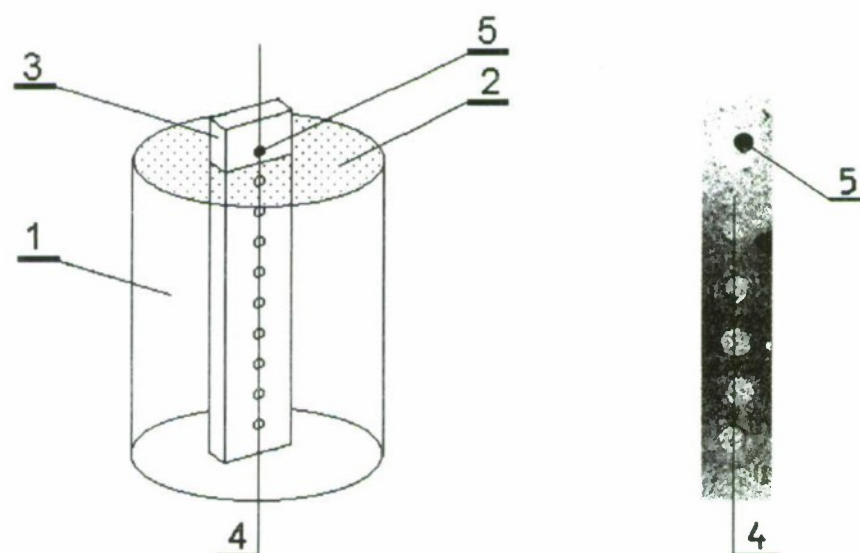
Fig. 2.3. Schematic structure of specimen for visualization (left) and photograph image (right) of central inserted plate containing highly metalized inclusions in the shape of cylinders with diameter 500 μm and height of 500 μm each.

1 - non-metalized propellant sample in cylindrical quartz shell,
2 - open butt-end of non-metalized propellant sample,
3 - protruding end of cured plate containing highly metalized inclusions,
4 - axis of sample,
5 - reference hole.

3. Experimental data treatment.

The video records were used for determining consecutive locations in time of burning agglomerates. These were input data for computer code developed for optimization of drag law for burning particles in flame of solid propellant.

One dimensional motion of vertically falling particle is described by equation (*). The following three independent parameters were chosen as determining the particle motion behavior: r_b, T_g, and M_g, where r_b is the burning rate of propellant, T_g and M_g are the temperature and molar mass of gas mixture, respectively. Then the gas density ρ_g and gas velocity V_g can be calculated by $\rho_g = \dfrac{P_0 M_g}{R_0 T_g}$ and $V_g = \dfrac{\rho_t r_b}{\rho_g}$, where P_0 is the pressure, ρ_t is the density of propellant, R_0 is the universal gas constant.

To solve numerically the above problem the following difference schemes were exploited:

$$V_{i+1} = (V_i - V_g \mp g / A) \exp(-A\tau) + V_g \mp g / A, \quad A = C_D \frac{24}{Re} \frac{18\mu}{\rho_p d^2},$$

$$x_{x+1} = x_i + (V_g \pm g / A)\tau + \frac{V_i - V_g \mp g / A}{A}(1 - \exp(-A\tau)),$$

where τ is the time step.

The input data represented consecutive co-ordinates of burning particles under assumption that diameter of particle remains constant and time between every two neighbor images is identical. The drag coefficient dependence on Re was assumed in the simplest form $C_D = K/Re$ [28, 29], where K is the matched constant. The best value of K was determined as delivering the minimum of functional Φ

$$\Phi = \left\{ \left[\sum_{j=1}^{j=N} \sum_{i=1}^{i=n_j} (X_{ij} - x_{ij})^2 \right] \bigg/ \sum_{j=1}^{N} n_j \right\}^{1/2}$$

in space of variables $\{K, x_{0j}, t_{0j}\}$ for given set of experimental data $j = 1, ..., N$. Here N is the total number of inclusions fired in individual run (usually $5 \div 7$), n_j is the number of trajectory images for j-th agglomerate on the record, X_{ij} is the experimental i-th coordinate of j-th agglomerate, x_{ij} is the calculated i-th coordinate of j-th agglomerate, x_{0j}, t_{0j} – initial trajectory point for j-th agglomerate.

Needed data on T_g, M_g, and μ were obtained using computer code ASTRA-3 in calculations for non-metalized propellant. The size and density of agglomerates were estimated on the basis of results obtained by sampling technique (see Section 1.5 for reference).

3.4. Experimental results.

The video records of combustion were used for determination of mean burning rate r_b of propellant sample at atmospheric pressure. Ccalculated on its basis the velocity of gas was further used in optimization procedure. Example of matching is shown in Fig. 2.4. The best result has been obtained when assuming finite (up to $20 \div 50$ cm/s) initial velocity of particles. Presumably, it can be explained by "shooting" the particles due to fast gas release on the surface at the moment

of ignition of agglomerate. This phenomenon was observed in special experiments with visualization of burning surface.

Figure 2.5 represents the values of coefficient C_D determined in experiments with different Re numbers. It is seen that when Re varies in the range $7 \div 9$ the optimal value of K in the expression $C_D = K/Re$ varies in the range $38 \div 52$. This result is close to the previous finding for burning coal particles [28, 29] and differs significantly of those corresponding to burning drops of liquid fuel [12, 31, 32].
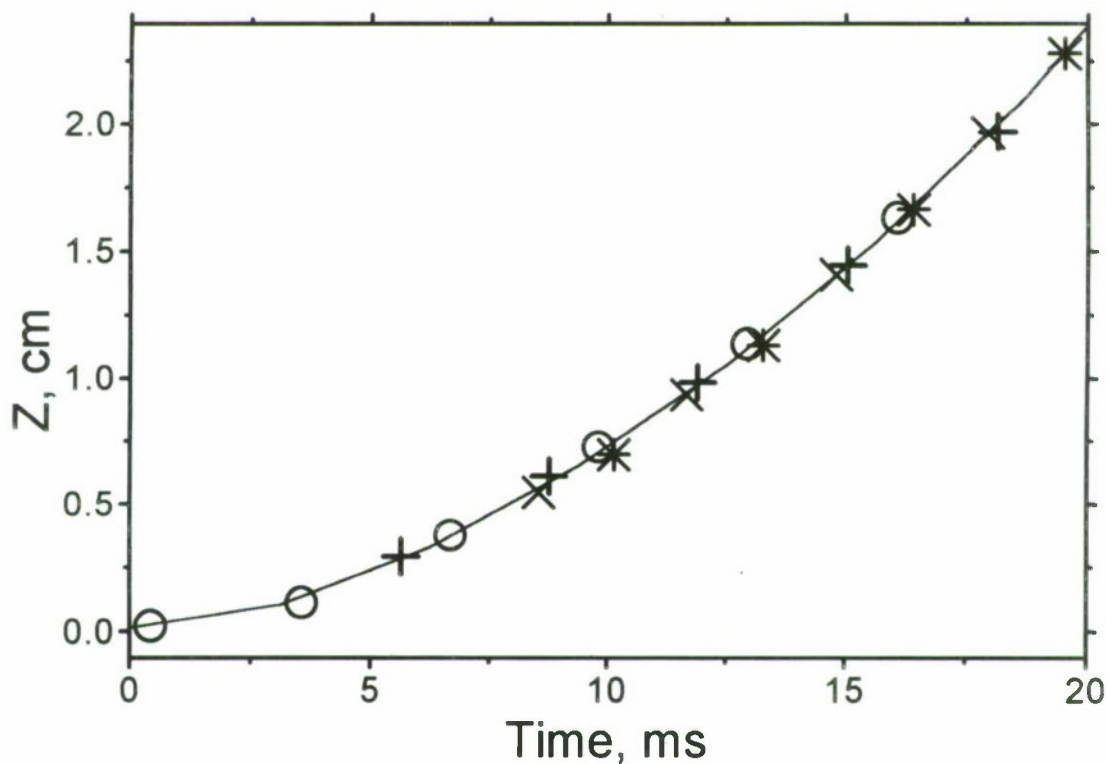
Fig. 2.4. Distance from the burning surface *vs* time for burning agglomerates. Each marker type (cross, circle or star) corresponds to different particle. Solid line represents the calculated approximation curve.
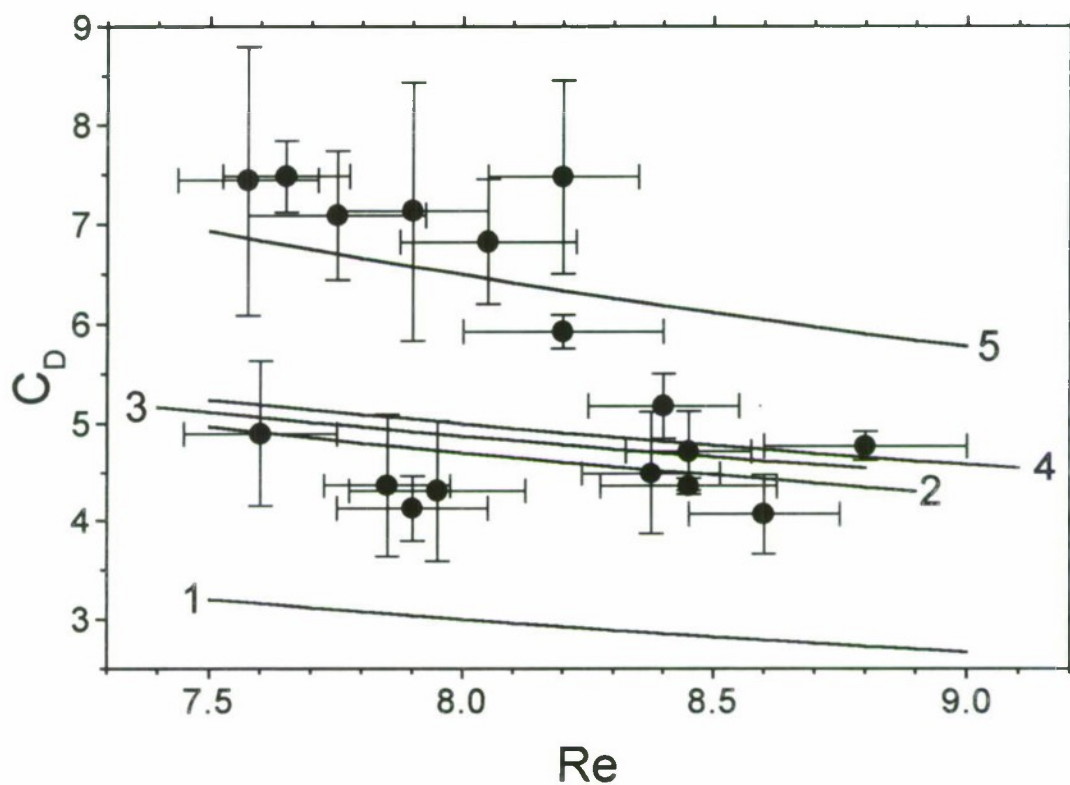
Fig. 2.5.
Drag coefficient of burning agglomerates *vs* Reynolds number.
Solid lines correspond to different drag laws taken from literature:
1 – classical Stokes law, 2 – [23-27], 3 – [14, 20, 21], 4 – [16, 17], 5 – [28, 29].
Vertical and horizontal bars correspond to estimated errors of optimization procedure induced by input data uncertainty.

3. THE STUDY OF CONDENSED COMBUSTION PRODUCTS OF ALEX CONTAINING MODEL PROPELLANTS

3.1. Background and objectives

Agglomeration of metal in combustion wave of composite propellants still remains unsolved problem because of great complexity of the physicochemical processes and the lack of data on behavior of metal particles under fast heating in oxidizing media. Using ultra fine metal particles gives additional possibility to affect the process of agglomeration due to enhanced chemical reactivity of metal and resulting increase of heat release in the vicinity of the burning surface. It is expected that this may facilitate an ignition of original metal particles as well as agglomerates on the burning surface resulting in decrease of size and total mass of agglomerates. The short literature survey and some previous results concerning Alex containing propellants combustion are reported in [34].

The objective of the present work was to measure condensed combustion products parameters (both for agglomerates and fine oxide particles) in combustion at elevated pressure of AP/HMX based propellants that contain Alex (aluminum exploded) and commercial aluminum in different proportions. The experiments have been performed in different gaseous media (argon or nitrogen) to estimate of environment effect on condensed combustion products (CCP) characteristics. The original sampling method [2] was used. The particle size distribution and unburnt aluminum content are the basic CCP characteristics that have been measured and that are discussed in this Chapter.

3.2. Manufacturing the model propellants and propellant ingredients characterization

The propellant formulations are presented in Table 3.1. They can be divided into two "lines" – propellants with HMX and without HMX. In each line the proportion of Alex and commercial aluminum has been varied. Additionally, we used ultra fine aluminum powder (UFA) which was slightly differ of Alex in size distribution and aluminum content in order to estimate the effect of fine aluminum properties. Powder of UFA was obtained by the method of electrical arc plasma re-condensation [35].

The results of particle size distribution analysis of cyclotetramethylene tetranitramine (HMX), ammonium perchlorate (AP), and aluminum (Al, Alex, UFA) are shown in Figs 3.1- 3.4. Two techiniques were employed for particle size analysis – optical microscope for coarse powders and Malvern 3600E sizer for fine powders. The following substances were used as carried liquid in Malvern analysis: hexane for AP, water for Al, acetone for Alex, UFA and CCP particles. In all cases the suspensions were subjected to ultrasound treatment during 40 second before measurement and the mechanical mixer was in action during measuremen. The particle size distribution for aluminum powders obtained using Malvern sizer are presented in Table 3.2. It should be noted that for normal functioning of the Malvern sizer the first and last size intervals must be empty (zero). With small size Alex or UFA powders this condition is not realized. Thus, the mass size distribution functions obtained for fine aluminum powders – Alex and UFA – have meaning of estimate only. However, one can see from these data at least the true upper limit size of particles.

In addition, the results chemical analyses for commercial and fine aluminum powders are presented in Table 3.3. The methods used are described in [36-38].

Mixing of components was performed in mortar made of teflon by summary weight of 100 g per batch. Curing of cylindrical propellant samples was performed individually in teflon forms with open ends in air at 70°C during 170 hours. The propellant density was determined on cured propellant samples.

It should be noted that the production of Alex containing propellant meets considerable difficulties due to large specific area of the Alex powder that results in poor mixing of components. Therefore, the acetone was used in mixing process as liquefying agent. Then acetone has been evaporated during curring. In this case one may expect appearance of porosity in the bulk of propellant. Sometimes the cavities with size up to 0.7 mm on lateral surface of cured samples were observed. The data on propellant density can be useful to evaluate the effect of this imperfection for each formulation. Therefore the scatter of experimental data on burning rate was relatively high as compared with ordinary propellant formulations. Nevertheless, the formulation effects discussed below take place at good coinciding burning rate in different series of experiment. The burning rate was calculated on the basis of known sample length and measured burning time derived from pressure-time record obtained in course of firing tests in sampling bomb.

Table 3.1. Propellant formulation (% mass.) for Alex effect studies

Batch #	Density, g/cm³	Alex/Al proportion	EB[1]	AP S = 6700 cm²/g	AP 160-315 µm	HMX commer-cial	Al D_{30} ~15 µm	Alex or UFA[2]
19	1.62±0.04	0/100	20	21	41	-	18	-
20	1.59±0.02	30/70	20	21	41	-	12.6	5.4
21	1.52±0.04	100/0	20	21	41	-	-	18
22	1.59±0.02	0/100	20	9	18	35	18	-
23	1.64±0.03	30/70	20	9	18	35	12.6	5.4
25	1.56±0.02	8.3/91.7	20	9	18	35	16.5	1.5
26	1.56±0.03	30/70	20	9	18	35	12.6	5.4[2]

Comments:
1) EB is the energetic binder based on nitryl rubber plastisized by diethylene glycol dinitrate (DEGDN) (98%) with additives (2%).
2) UFA was used in the batch #26 only.
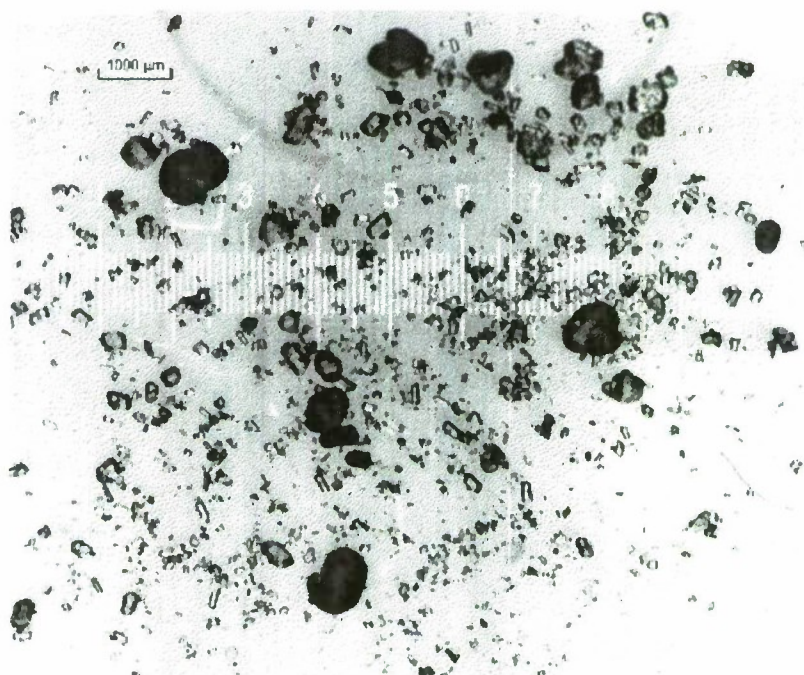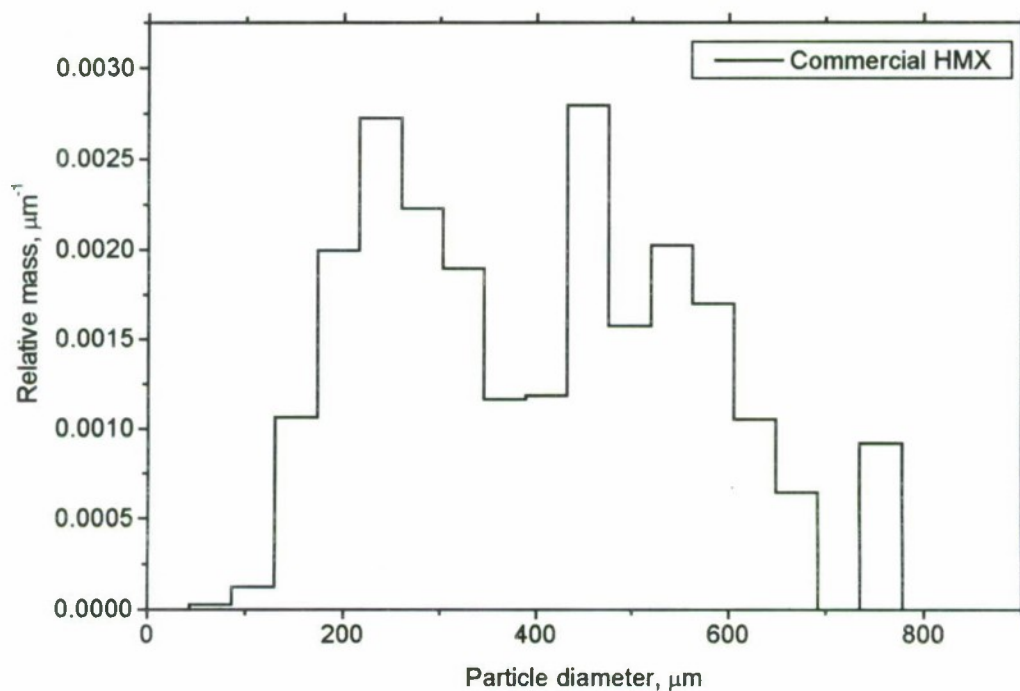
Fig. 3.1. Mass size distribution and photography image of commercial HMX powder used in manufacturing the model propellants.

Measurements were made by optical microscope.

D_{mn}, µm: D_{10}=211; D_{20}=236; D_{30}=264; D_{21}= 265; D_{32}=330; D_{43}=402; D_{53}=434.
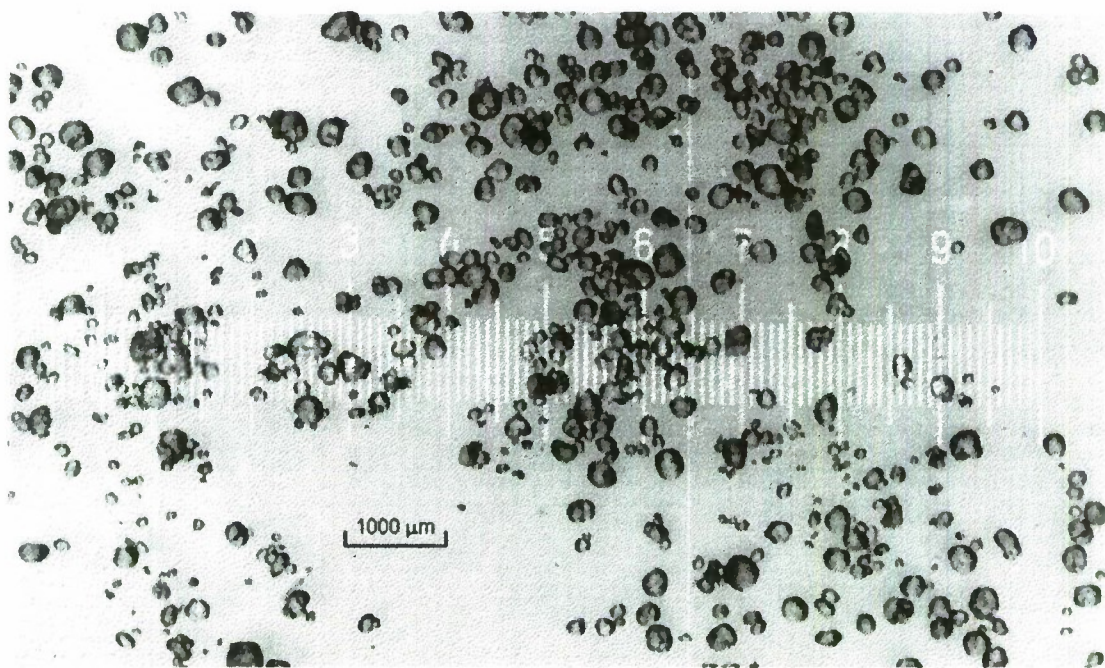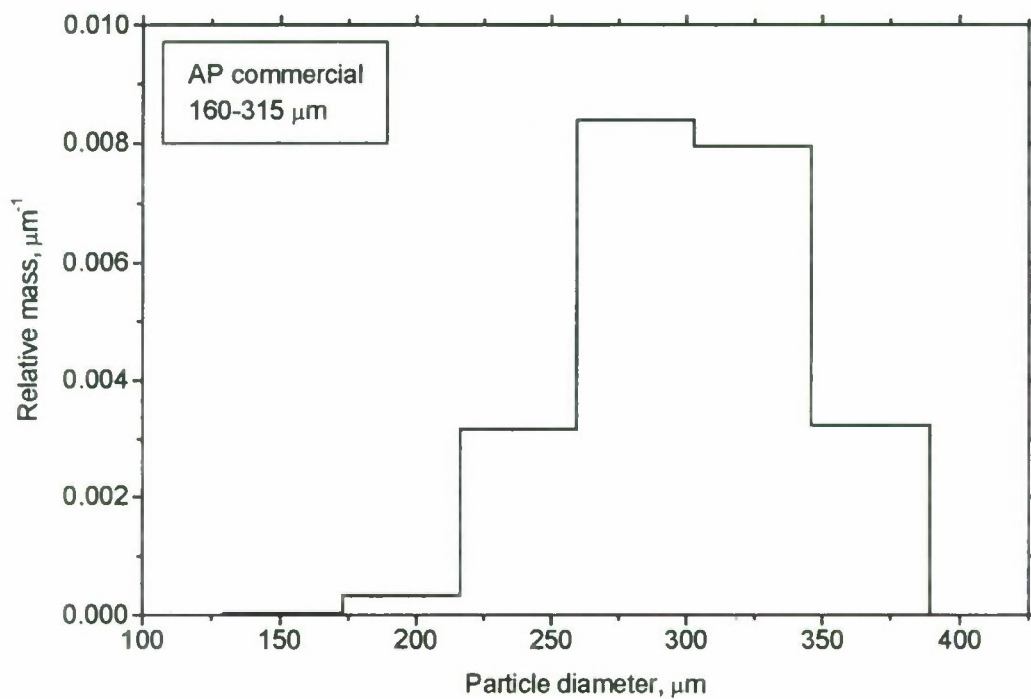
Fig. 3.2. Mass size distribution and photography image of commercial AP 160-315 μm particles used in manufacturing the model propellants.

Measurements were made by optical microscope.

D_{mn}, μm: D_{10}=282; D_{20}=285; D_{30}=288; D_{21}=288; D_{32}=294; D_{43}=301; D_{53}=304.
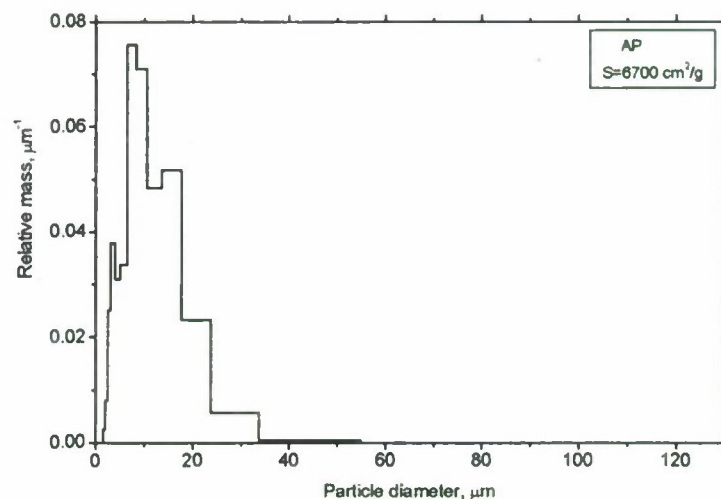
Fig. 3.3. Mass size distribution for fine AP with S = 6700 cm^2/g used to manufacture the model propellants.

Measurements were made by Malvern 3600E in hexane after treatment of suspension with ultrasound during 40 seconds, mixer ON, size range 0.5-118 μm.

D$_{mn}$, μm: D$_{10}$=4.5; D$_{20}$=5.4; D$_{30}$=6.6; D$_{21}$=6.5; D$_{32}$=9.6; D$_{43}$=13.1; D$_{53}$=14.8.
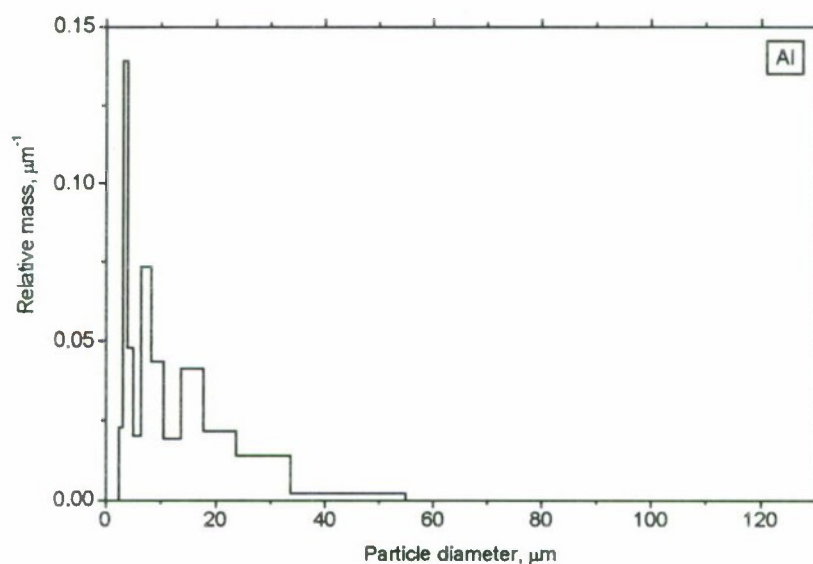
Fig. 3.4. Mass size distribution for commercial aluminum used in manufacturing the model propellants.

Measurements were made by Malvern 3600E in water after treatment by ultrasound during 40 seconds, mixer ON, size range 0.5-118.4 μm.

D$_{mn}$, μm: D$_{10}$=4.2; D$_{20}$=4.8; D$_{30}$=5.9; D$_{21}$=5.5; D$_{32}$=8.8; D$_{43}$=15.2; D$_{53}$=18.7.

41
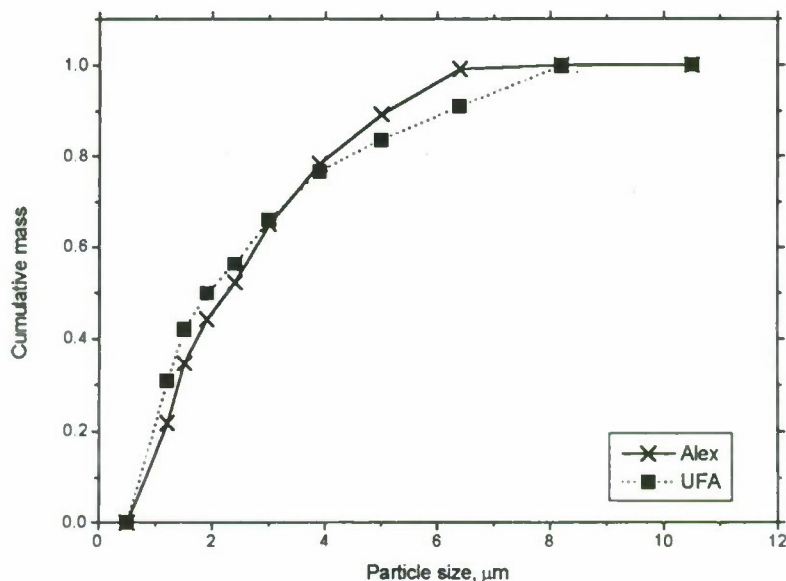
Fig. 3.5. Cumulative mass size distribution for Alex and UFA powders used in manufacturing the model propellants.

Measurements were made by Malvern 3600E in acetone after treatment by ultrasound during 40 seconds, mixer ON, size range 0.5-118.4 μm.

Table 3.2. Mass size distribution of aluminum powders - Malvern 3600E results

Channel No.	Histogram size range		Mass fraction in given size range, %		
	Left bound, μm	Right bound, μm	Commercial Al	Alex	UFA
1	0.5	1.2	0	21.8	30.7
2	1.2	1.5	0	12.8	11.2
3	1.5	1.9	0	9.7	8.0
4	1.9	2.4	0	8.0	6.4
5	2.4	3.0	1.5	12.8	9.7
6	3.0	3.9	12.5	13.3	10.6
7	3.9	5.0	5.0	11.0	7.1
8	5.0	6.4	2.9	9.8	7.3
9	6.4	8.2	13.6	0.8	8.8
10	8.2	10.5	9.8	0	0.2
11	10.5	13.6	5.7	0	0
12	13.6	17.7	17.3	0	0
13	7.7	23.7	13.2	0	0
14	23.7	33.7	13.7	0	0
15	33.7	54.9	4.8	0	0
16	54.9	118.4	0	0	0

Fig. 3.6. Three electron microscope images of Alex powder.

Microscope JEM-100SX, magnification 5600^X. Probe preparation – precipitation from air flow.

One can see individual round shape particles with size about 1 μm within large amount of small (<0.1 μm) particles.

Table 3.3. Chemical analysis data (% mass.) for commercial aluminum and fine aluminum powders used in propellant manufacturing

Ingredient	Method	Commecial Al	Alex	UFA
Metallic Al	permanganatometric	97.8±0.9%	82.2±0.3%	85.5±0.7%
Total Al	gravimetric	98.65±0.05%	92.5±0.2%	93.3±0.3%
AlN	ammonia distillation	NA	0.63%	NA
Al_2O_3	calculated from mass balance	2.2%...3.3%	17.8%...15.9%	14.5%...14.2%

3.3. The set up and experimental procedure

The original technique designed for simultaneous sampling of agglomerates and oxide particles in one run followed by size distribution and chemical analyses has been described previously [2-4]. Below we observe briefly the specific features of approach used in this part of work deal with Alex containing propellants.

• The blow through bomb (Fig. 3.6) consists of massive case *1* supplied with gas inlet *12* and outlet *7* valves which allow to maintain an appropriate gas flow rate in the bomb. Inside the bomb there is a steel cylinder *4* of 50 mm in diameter. The propellant specimen *9* mounted in the top cover *2* inside of cylinder *4* via cylindrical holder with conic cowling *11* that fixed within the ring slot *10* of cover *2* by three spokes *3*. The slot dimension is ($\varnothing 40 - \varnothing 30$) mm. The bottom of a cylinder is supplied with a set *5* of wire mesh screens and aerosol analytical filter AFA *6*. The propellant specimen is ignited by nichrome wire *8* and the flame torch is directed downward. The cylinder *4* interior blow through continuously during the experiment by inert gas. The diameters of the propellant specimen *9* and cylindrical holder *11* were equal. The propellant sample diameter was fixed by its butt-end on holder with fast drying glue "Moment-2".
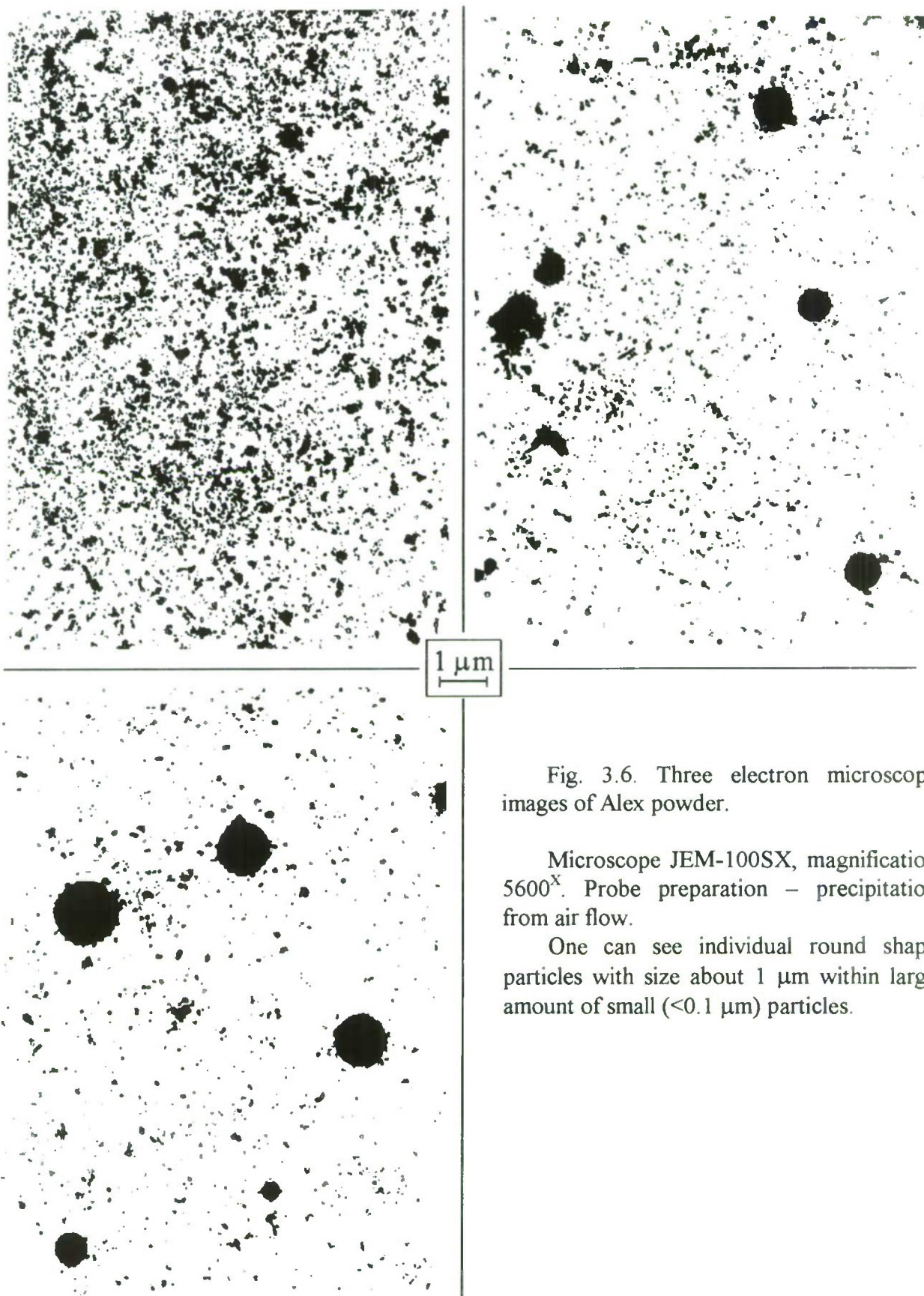
• Two duluting/quenching gases – argon or nitrogen - were used for pressurization the bomb.

• Samples for the firing tests have cylindrical shape with diameter 7.8 mm and length 16-18 mm. The lateral surface was inhibited by vacuum oil Alcaren® to prevent contamination of condensed combustion products with product of pyrolysis of the hard inhibition layer made, for example, made of plexiglas or teflon. Additionally, the weak gas flow (~ 1 cm/s, total mass flow rate of inert gas through the bomb is about 1.8-2 g/s) was along the lateral sample surface directed from cold to hot end. Obviously, the oil drops were trapped by wire mesh screens and by filter but special tests have shown that oil did not make effect on particle size distribution and on chemical analysis results. Unfortunately, the presence of oil in sampled products caused the change for the worse the scatter of experimental data on weight characteristics for total sampled mass and mass of fine particles.

• Each experimental series consisted of 3 propellant samples with total mass about 4 g which were consecutively combusted under identical conditions that provided generation of 1.4-2 g of CCP used for further analyses.

• The thin (~ 1 mm) layer of non-metalized propellant matrix (see Chapter 1) was attached to the butt end of propellant specimen to make easier the ignition.

• The burning rate was calculated as specimen length divided by the burn out time. The last one was determined from pressure-*vs*-time record obtained in course the sampling test.

• The initial pressure at all experiments was 40 atm, the maximum rise of pressure during the combustion run was 11-12 atm. The characteristic pressure in the individual run was taken as a half of sum of initial and final pressures. The characteristic pressure and burning rate for given series were chosen as arithmetical mean values of characteristic pressure and burning rate for individual runs.

• The nominal mesh sizes of wire screens in the stack installed inside the bomb were 130, 150, 300, and 450 μm.

• The CCP particles captured by wire screens in the bomb were divided into fractions via dry and wet sieving in acetone by using sieves with the same mesh sizes. The particles caught by the filter were extracted by way of dissolving the filter matter in acetone. After that and then they were added to the sieve fraction <130 μm. The mass of particles trapped by filter was calculated as difference of filter mass before and after the experiment. All sieved fractions of CCP particles were weighed after drying with accuracy of no less than 0.00015 g and then were subjected to particle size and chemical analysis. The latter was made by permanganatometric method [4] that allowed typically to determine 0.5÷45 mg of the unburnt aluminum with accuracy 3÷15 relative % at aluminum content 10÷30% In special cases the more complex analysis was performed for determine the nitride or oxinitride in fine fraction of CCP via chemical and RFA methods.

• The fine (< 130 μm) particles were analyzed with commercial sizer Malvern 3600E using acetone as carrier liquid after 40 seconds treatment with ultrasound and with continuous mechanical mixing of suspension. 16 channels were employed with exponential incrementing width in size range 0.5-118.4 μm.

• Particle size analysis for particles 130-450 μm was performed using optical microscope. The accuracy of size measurement estimated as a half of histogram sub-range was equal 9 μm for fractions in the size range 130-300 μm, and 22 μm for fractions 300-450 μm.

• The density of fine (< 130 μm) particles was assumed to be equal 3.71 g/cm^3 while the mean density of coarse (> 130 μm) particles was determined individually in each sieved fraction via procedure described above in Chapter 1.
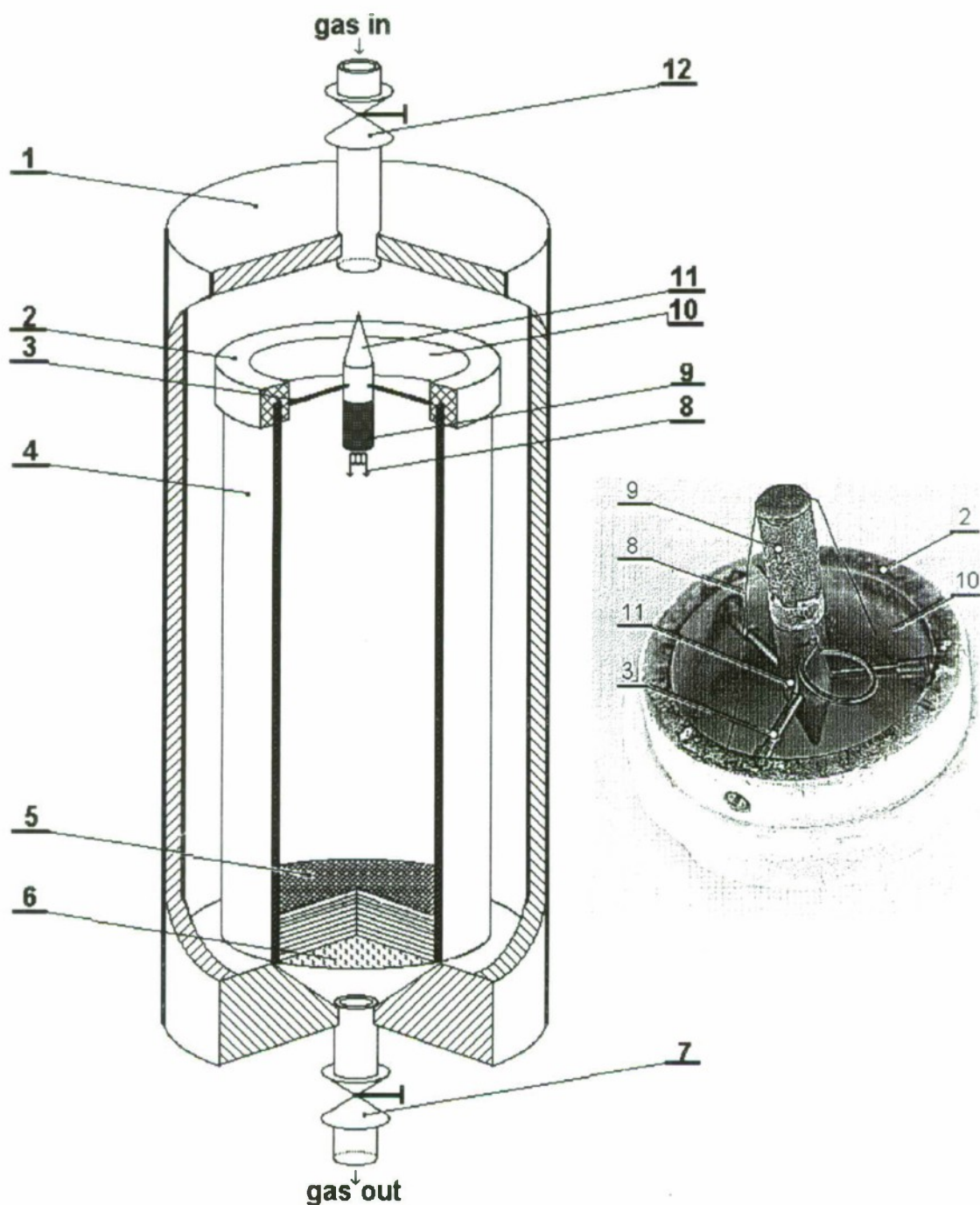
Fig. 3.6. Chart of the flow bomb for CCP particle sampling and photograph images of cover *2*.

1	-	bomb body,
2	-	top cover of the cylinder *4*,
3	-	one of three spokes,
4	-	thin wall cylinder,
5	-	stack of wire mesh screens,
6	-	filter,

7	-	gas outlet valve.
8	-	ignition wire,
9	-	propellant specimen,
10	-	ring slot for blowing the cylinder *4*,
11	-	specimen holder with conic cowling
12	-	gas inlet valve.

46

3.4. Definition of the parameters used to characterize CCP particles.

Based on the results of above mentioned particle size analysis and chemical analysis of sieved fractions of CCP, the two mass size distribution functions were calculated using original computer code and taking into account the following issues:

- mass contribution of individual fractions and their size distribution;
- mean particle density in given sieve fraction of the CCP;
- overlapping the histograms corresponding to different sieve fractions.

Mass size distribution function for CCP particles, $f(D)$, in the form of distribution of relative mass of CCP, is defined as $f_i(D) = m_i / (M_{prop} \cdot \Delta D_i)$, where m_i is the mass of CCP in the i-th histogram sub-range (size interval), and ΔD_i is the width of i-th size interval.

Mass size distribution function for unburnt aluminum in CCP, $f_i^{Al}(D)$, is defined as $f_i^{Al}(D) = f_i(D) \cdot \varepsilon_j^{Al}$, where $f_i(D)$ is the histogram of relative mass of CCP, ε_j^{Al} is the mass content of aluminum in the j-th sieve fraction. Index i is omitted below.

D_L and D_R bound sizes. In accordance with chemical analysis results and commonly used notion the whole population of CCP particles was treated as consisting of *coarse* and *fine condensed combustion products*.

The CCP particles with size exceeding D_L are called here the *coarse* particles or ***agglomerates***. The particles with size $D<D_L$ are called *fine* or *oxide* particles.

For propellants under study bound size D_L can be easy establish as local minimum in mass size distribution function, $f(D)$, for CCP particles, because for most propellants there is the size interval with $f(D) \approx 0$. This size interval is commonly localized in the range 33-127 μm.

When calculating the mean diameters for agglomerates, the upper limit size D_R was used. This size is the maximal size of agglomerates that is determined as right end of monotonous portion of the normally filled with particles $f(D)$ curve. Actually, single particles with size greater than D_R were excluded from calculations of the characteristic mean sizes D_{mn} of agglomerates. In previous our report [3] it was proposed that extended right hand side tail in mass size distribution can be caused by transient combustion of propellant sample when burning surface reaches sample holder plate. The another source of huge particles is the nichrome wire used for sample ignition [39]. After ignition the wire remains in two phase flow of hot combustion products and burns out. The ends of wire are fused and get spherical shape, see Fig. 3.7. Then these spheres may detach from wire and enter into gas flow. It is important that these particles are usually coated with aluminum and aluminum oxide and can not be distinguished of true agglomerates by visual analysis. That is why it is necessary that these particles were also subjected to chemical analysis for determining the aluminum content in CCP. Meanwhile, the nichrome containing "wrong" particles might be easily recognized after density measurement. Typically, their mean density is about 4.5-6 g/cm³.

In general, the procedure for D_R establishment in not free of some arbitrariness.

Dimensionless mass characteristics of CCP

The following mass characteristics were calculated for fine (smoke aluminum oxide) and coarse (agglomerate) particles on the basis of experimental mass size distribution functions for CCP particles $f(D)$ and for aluminum in CCP particles $f^{Al}(D)$. These parameters are scaled by M_{prop}, where M_{prop} is the total mass of propellant burnt. For example, $m_f = M_f/M_{prop}$ where M_f is the mass of fine particles.

m_f – dimensionless mass of fine particles,

m^{Al}_f – dimensionless mass of free aluminum in fine particles,

m_{ag} – dimensionless mass of agglomerates,

m^{Al}_{ag} – dimensionless mass of free aluminum in agglomerates,

$m_{ccp} = m_f + m_{ag}$ – total dimensionless mass of CCP,

$m^{Al}_{ccp} = m^{Al}_f + m^{Al}_{ag}$ – total dimensionless mass of aluminum in CCP,

m^{Al}_{prop} – dimensionless initial mass of aluminum in propellant,

m_{ag}/m_{ccp} – relative mass fraction of agglomerates in CCP,

m_f/m_{ccp} – relative mass fraction of fine particles in CCP,

$[Al]_f = (m^{Al}_f/m_f) \cdot 100\%$ - percentage of free aluminum in fine particles,

$[Al]_{ag} = (m^{Al}_{ag}/m_{ag}) \cdot 100\%$ - percentage of free aluminum in agglomerates,

$[Al] = (m^{Al}_{ccp}/m_{ccp}) \cdot 100\%$ - percentage of free aluminum in CCP,

m^{Al}_f/m^{Al}_{prop} - relative quantity of free aluminum in fine particles,

$m^{Al}_{ag}/m^{Al}_{prop}$ - relative quantity of free aluminum in agglomerates[*],

$m^{Al}_{ccp}/m^{Al}_{prop}$ - total relative quantity of unburnt aluminum in CCP,

$m_f : m_{ag}$ - mass ratio of fine particles and agglomerates in CCP,

$m^{Al}_f : m^{Al}_{ag}$ - mass ratio of free aluminum in fine particles and in agglomerates.

Mean diameter (size) of CCP particles, D_{mn}, is calculated by

$$D_{mn} = {}^{m-n}\!\!\sqrt{\left(\sum_{i=1}^{k} D_i^m \cdot N_i\right)\Big/\left(\sum_{i=1}^{k} D_i^n \cdot N_i\right)} \, ,$$

where D_i is the midrange and N_i is the number of particles in i-th size range. To calculate mean size D_{mn} on the basis of experimentally determined mass size distribution we used following formula to obtain effective number of particles N_i in a given i-th size interval:

$$N_i = \frac{m_i}{\frac{\pi}{6} D_i^3 \rho_p} \, ,$$

---

[*]) This parameter (incompleteness of aluminum combustion) was used in our previous works [3, 39] being designated as "η".

where density of CCP particles ρ_p was assumed to be equal 2.4 g/cm^3 for agglomerates and 3.7 g/cm^3 for oxide particles.

The mean diameters for fine particles were calculated in the size range from 0.5 μm to D_L. The mean diameters for agglomerates were calculated in the size range from D_L to D_R, where D_R is an effective maximum size of agglomerates. The procedure for determining D_R is described above.
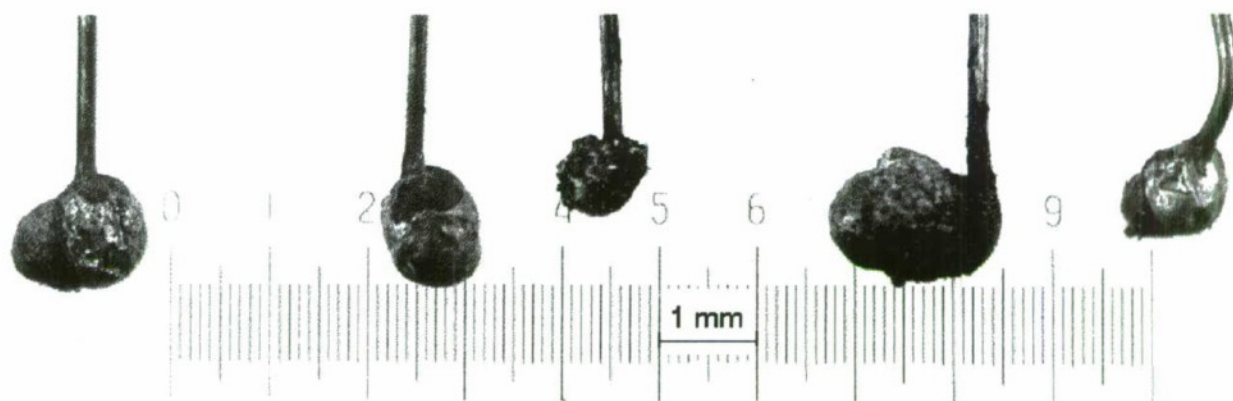
Fig. 3.7. Huge particles formed through the fuse of the end of nichrome igniting wire.

3.5. Experimental program.

The detailed mass size distribution in the size range from 0.5 μm to maximum sampled particle diameter for condensed combustion products and for unburnt aluminum in condensed products was determined in 13 series listed in Fig. 3.8. The series identifier consists of letter A (Argon) or N (Nitrogen) and the number, which represents batch # from Table 3.1.

The effect of the commercial aluminum replacement by Alex has been studied in series consequence A19-A20-A21 and N19-N20-N21 for Ar and N$_2$ gaseous media for propellant formulations without HMX.

Analogous approach was used in series N22-N25-N23 (A23) for propellant formulations with HMX.

The experimental series A23, N23, A26 and N26 was performed to estimate fine aluminum type effect. For this UFA was used in formulation #26. The experimental conditions in series N26D (the letter "D" means "duplicate") were chosen as an exact copy of the conditions in series N26. Thus, the comparison the results of N26 and N26D series gives the notion about general reproducibility of experimental and treatment procedures.

It should be remembered that all series were carried out practically at the same pressure level (46-50 atm) that gives a basis for reliable comparison of the results.

Formulations without HMX

Alex/Al →   0/100   30/70   100/0

A19	A20	A21
N19	N20	N21

HMX containing formulations

Alex/Al →   0/100   8.3/91.7   30/70

A23

N22   N25   N23

A26

N26, N26D
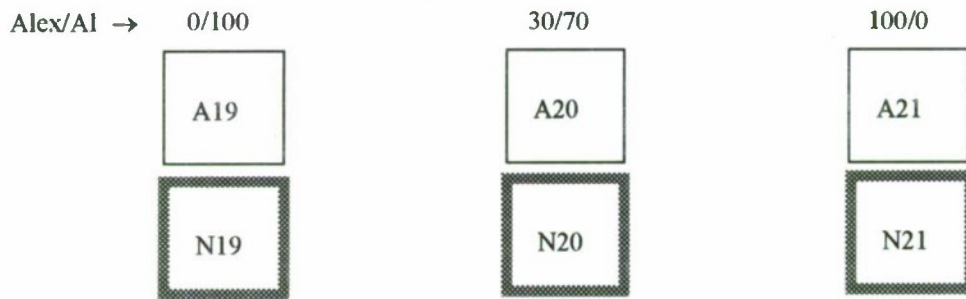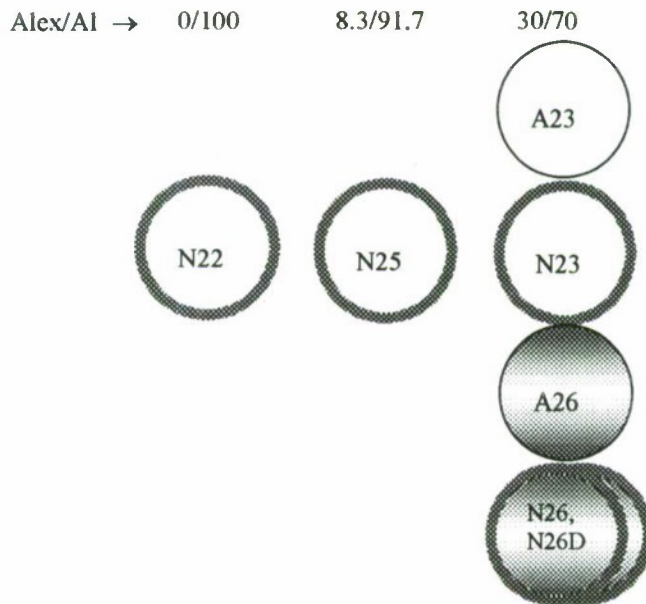
Fig.3.8. The set of experimental series.

Figure legend (propellant type, gaseous environment, Alex type):
     Form:
         Square – formulation without HMX,
         Circle – HMX containing formulations.
     Bound:
         ――― – argon environment,
         ▬▬▬ – nitrogen environment.
     Shadowed figures: UFA containing formulation.

3.6. General characteristics of sampled CCP.

The example of mass size distribution function for sampled CCP particles is presented in Fig. 3.9 in linear (*a*) and logarithmic scale (*b*). The plots represent the results obtained in series N25 (pressure 46 atm) but they demonstrate all common features of the results obtained for propellants #19 - #26. This can be also seen from the data presented in Table 3.3. Examining experimental data, one may conclude:

• The propellants exhibit very effective aluminum conversion and low intensity of the agglomeration process. The agglomeration behavior obeys to early described [40] *weakly agglomeration scenario*. This scenario is characterized by high efficiency of aluminum conversion into oxide particles and moderate size of agglomerates. Their formation is relatively rare event that brings small contribution of the agglomerates mass into total CCP mass.

• The total range of CCP particle sizes is wide enough with maximum size of agglomerates about 950 μm, but main contribution into agglomerates mass is provided by particles with size up to approximately 300-400 μm.

• There is well pronounced boundary D_L (~ 100 μm) between coarse and fine CCP particles in the mass size distribution function.

• For most propellants the main portion of non-consumed aluminum is presented in agglomerates. Detailed data on content of unburnt aluminum in CCP are reported in Table 3.4.

• In Fig. 3.9b one can see that the mass size distribution function for fine (oxide) CCP particles has the main peak located in the range 3÷3.9 μm of Malvern's histogram. This fact was observed also in our previous investigations and by other authors. The mechanism of formation of oxide particles with such size is not clear yet.

In order to describe the experimental data on sampled CCP particles in more detail we will discuss separately the results corresponding to the coarse and fine size CCP. The reason for this is the natural division of CCP into 2 global modes by its nature and by size scale that is seen from plots in Fig. 3.9.
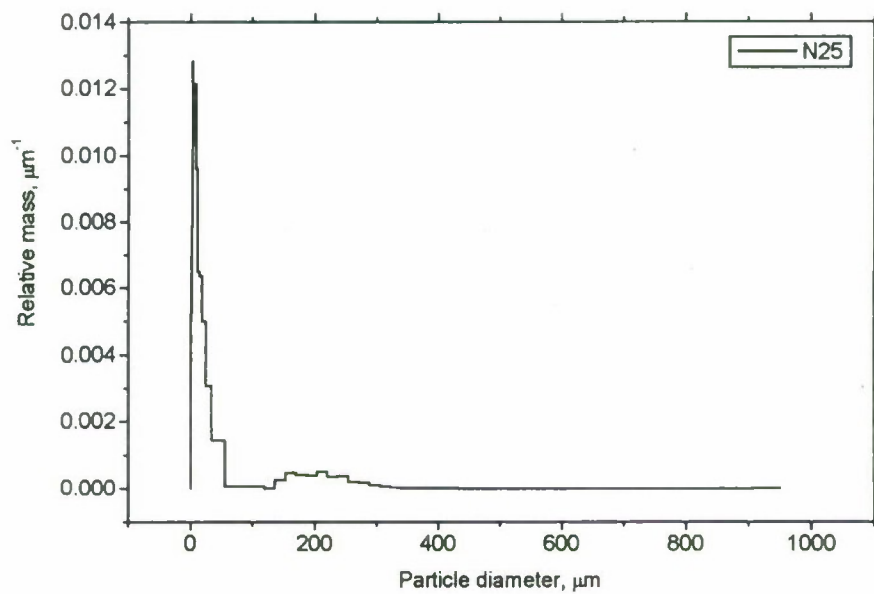
a)
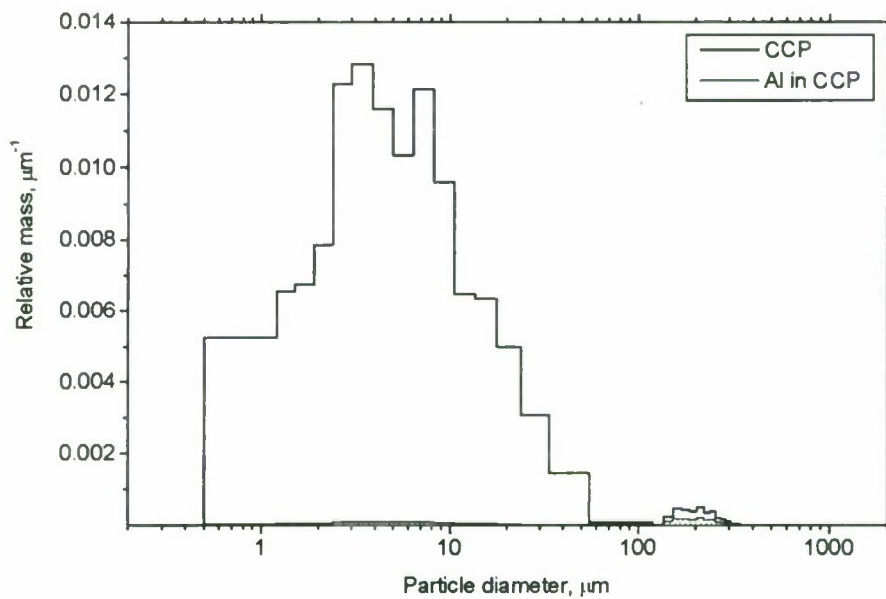
b)

Fig. 3.9.

Typical relative mass size distribution $f(D)$ of CCP particles plotted in linear (a) and in logarithmic (b) scale. Additionally, in Fig. (b) the mass size distribution $f^{Al}(D)$ of free aluminum in CCP is pictured (bottom shadowed histogram). It should be noted that in the case (b) the area under histogram curves is **not** directly proportional to the value of mass of particles.

Table 3.3. Test conditions – pressure P and burning rate r – and total CCP characteristics

Series	P, atm	r, mm/s	m_{ccp}	m^{Al}_{ccp}	$m_f{:}m_{ag}$	$m^{Al}_f{:}m^{Al}_{ag}$	$m^{Al}_{ccp}/m^{Al}_{prop}$
A19	49	39±10	0.514	0.0104	97:3	10:90	0.058
N19	46	48±9	0.371	0.0146	89:11	7:93	0.081
A20	49	61±6	0.374	0.0066	96:4	14:86	0.037
N20	44	60±6	0.289	0.0093	90:10	6:94	0.052
A21	50	290±40	0.442	0.0015	98:2	80:20	0.008
N21	46	290±50	0.542	0.0029	99:1	76:24	0.016
N22	46	22±2	0.297	0.0347	69:31	4:96	0.193
A23	46	41±4	0.365	0.0129	91:9	15:85	0.072
N23	46	46±7	0.433	0.0154	88:12	7:93	0.085
N25	46	35±3	0.306	0.0271	80:20	7:93	0.150
A26	47	40±6	0.288	0.0124	90:10	16:84	0.069
N26	46	40±4	0.452	0.0148	90:10	12:88	0.082
N26D	46	50±6	0.370	0.0150	88:12	9:91	0.084

Table 3.4. Chemical analysis data on unburnt aluminum for individual sieve fractions of CCP particles and averaged over all sampled CCP (% mass.)

Series	< 130 μm	130-150 μm	150-300 μm	> 300 μm	$[Al]_{ccp}$
A19	0.21	57.0	57.4	~2	2.0
N19	0.30	33.4	39.7	7.7	3.9
A20	0.26	47.0	37.0	0	1.8
N20	0.22	35.0±1.2	39.4	5.2	3.2
A21	0.27	2.8	3.1	~4	0.3
N21	0.42	8.0	~14	~6	0.5
N22	0.63	37.4±1.0	38.2±0.5	33.8±1.6	11.7
A23	0.58	36.5	33.4	0	3.5
N23	0.30	24.5±0.5	31.2±0.3	~5.6	3.5
N25	0.78	39.4±0.5	43.8±0.3	24.0	8.9
A26	0.79	40.0	39.6	3.7	4.3
N26	0.32	25.1±0.1	39.4±0.2	4.7	3.3
N26D	0.42	29.3	33.2±0.5	6.7	4.1

Comments:
1. In most cases the data presented correspond to the mean result of analyses of two independent probes. The figure after sign ± corresponds to standard error of determined value. This figure is not written if mass of given fraction of CCP was too small to repeat an analysis and only one determination was made.
2. The sign ~ in some boxes corresponds to low accuracy data due to small absolute mass of the probe (fraction).

3.7. Agglomeration characteristics.

3.7.1. Morphological description and particle density

It has to be underlined that all propellants demonstrate very weak agglomeration ability and high efficiency of aluminum conversion. The mass fraction of agglomerates in CCP is relatively low, see Table 3.5. Thus, agglomerate analysis in this Chapter is performed mainly to in order to give general idea

The CCP coarse particles (> 130 μm) were examined by optical stereoscopy microscope with magnification up to 56^X. The major condensed products of combustion are classical agglomerates (**Ag**), i. e. the particles of spherical shape covered with hard surface layer of dark gray or black color. Occasionally, the ejected grains of oxidizer (**Oxz**) were observed in fractions 130-150 μm and 150 -300 μm and white colored oxide particles (**Ox**) were observed in fraction 130-150 μm. In all cases the content of **Ox** particles did not exceed 0.5% by number. The weight characteristics of agglomerate particles and the fact of observation of the particle types different from **Ag**-type are presented in Table 3.5. Additionally, in last column the event of post-oxidation is marked. The post-oxidation manifests itself as friable surface coating during long storage of particles at room conditions. In this case decrease of fraction weight up to 10% was detected.

Analyzing the data in Table 3.5, the following trends have been noticed:

- The presence of ejected oxidizer grains and post-oxidation is characteristic of HMX-containing formulations.
- The presence of coarse white color oxide spheres is typical for formulations that demonstrate highest efficiency of aluminum combustion.

Table 3.7 presents complete data set on the mean density of particles *vs* particle diameter in sieved fractions of CCP, including the extra large particles that are not "normal" agglomerates (mainly in fractions 300-350 μm and >450 μm) and contain nichrome. The origination mechanism of these particles was described in Section 3.4. Note that namely the abnormal high density was a criterion for exclusion of such particles from consideration in calculation based on size distribution function.

The method to obtain density value for a given CCP fraction is described in Section 1.3. One can see that for normal agglomerates the mean density is about 2.1÷2.3 g/cm³, except series A21 and N21 (formulations with 100% Alex). In these cases the density equals 1.3÷2.0 g/cm³. It should be added that sampled agglomerates in series A21 and N21 have rough surface which is coated with flakes attached to the surface. One may propose that in combustion of this formulation a partial destruction of the burning surface, i. e. dispersion, does occur. Presumably, some part of agglomerates finish their own formation not in condensed phase but later in gas phase. This is why the appearance and density for these agglomerates have distinctive features. There are following arguments to demonstrate the disturbance of layer-by-layer character of combustion of the formulation based on pure Alex:

- The damage of interior components of the bomb, see Fig. 3.10. During the firing tests a loud sound (like explosion) was observed.
- The sampled condensed combustion products partially consist of powder that looks like crushed propellant specimen matter. This powder can be dissolved in acetone and in water. The chemical and RFA analyses show the presence of AP (up to 27% mass. in the case of propellant #21) in this powder matter.

Table 3.5. Weight characteristics of agglomerates and observed particle types.

Series	D_L-D_R, μm	m_{ag}	m^{Al}_{ag}	$[Al]_{ag}$	Particle type			Post oxidation
					Ag	Oxz	Ox	
A19	34-289	0.018	0.0094	52.5%	+			
N19	100-289	0.040	0.0136	34.2%	+		+	
A20	24-433	0.015	0.0057	38.0%	+		+	
N20	118-238	0.026	0.0087	33.5%	+		+	+
A21	34-433	0.010	0.0003	2.9%	+		+	
N21	24-306	0.007	0.0007	10%	+			
N22	118-736	0.093	0.0334	35.9%	+			+
A23	34-306	0.033	0.0110	33.3%	+			
N23	118-325	0.052	0.0143	27.5%	+	+		+
N25	118-605	0.061	0.0252	41.3%	+			+
A26	34-736	0.030	0.0104	34.7%	+		+	
N26	118-303	0.043	0.0135	31.4%	+	+		
N26D	118-306	0.047	0.0136	28.9%	+			

Table 3.6. Mean size D_{nm} for agglomerate particles calculated in size interval D_L-D_R.

Propellant and series	D_L-D_R, μm	D_{10}, μm	D_{20}, μm	D_{30}, μm	D_{21}, μm	D_{32}, μm	D_{43}, μm	D_{53}, μm	D_{43}/D_{10}
A19	34-289	167	168	170	170	174	179	181	1.07
N19	100-289	165	168	170	170	174	180	182	1.09
A20	24-433	172	174	176	176	181	186	190	1.08
N20	118-238	162	163	164	164	166	169	170	1.04
A21	34-433	188	194	202	201	217	237	248	1.26
N21	24-306	162	164	167	167	173	180	184	1.11
N22	118-736	212	220	230	229	250	274	288	1.29
A23	34-306	183	186	189	189	195	201	205	1.10
N23	118-323	174	177	180	180	186	193	196	1.11
N25	118-605	186	190	195	195	205	218	225	1.17
A26	34-736	171	174	179	177	188	212	239	1.24
N26	118-303	170	173	175	175	181	187	190	1.10
N26D	118-306	171	174	177	177	183	189	192	1.11

Table 3.7.

Mean density and diameter of agglomerate particles in individual sieved fractions of CCP

Series	130-150 μm	150-300 μm	300-450 μm	> 450 μm
A19	$D_{10}=156\pm9$	$D_{10}=197\pm9$	$D_{10}=479\pm22$	$D_{10}=1200\pm22$
	$\rho=2.3\pm0.4$	$\rho=2.1\pm0.3$	$\rho=5.4\pm0.8$	$\rho=4.7\pm0.3$
N19	$D_{10}=152\pm9$	$D_{10}=196\pm9$	$D_{10}=456\pm22$	$D_{10}=973\pm22$
	$\rho=2.2\pm0.4$	$\rho=2.1\pm0.3$	$\rho=3.0\pm0.4$	$\rho=4.7\pm0.3$
A20	$D_{10}=159\pm9$	$D_{10}=192\pm9$	$D_{10}=378\pm22$	$D_{10}=1100\pm22$
	$\rho=2.1\pm0.3$	$\rho=2.1\pm0.3$	$\rho=4.7\pm1.0$	$\rho=5.6\pm0.4$
N20	$D_{10}=153\pm9$	$D_{10}=185\pm9$	$D_{10}=473\pm22$	$D_{10}=822\pm22$
	$\rho=2.2\pm0.4$	$\rho=2.2\pm0.3$	$\rho=0.9\pm0.2$	$\rho=5.7\pm0.4$
A21	$D_{10}=163\pm9$	$D_{10}=232\pm9$	$D_{10}=400\pm22$	-
	$\rho=1.3\pm0.2$	$\rho=1.6\pm0.2$	$\rho=0.7\pm0.1$	
N21	$D_{10}=152\pm9$	$D_{10}=194\pm9$	$D_{10}=395\pm22$	-
	$\rho=2.0\pm0.3$	$\rho=2.3\pm0.3$	$\rho=1.1\pm0.2$	
N22	$D_{10}=158\pm9$	$D_{10}=233\pm9$	$D_{10}=346\pm22$	$D_{10}=595\pm22$
	$\rho=2.2\pm0.4$	$\rho=2.0\pm0.2$	$\rho=2.5\pm0.5$	$\rho=1.6\pm0.2$
A23	$D_{10}=162\pm9$	$D_{10}=211\pm9$	$D_{10}=843\pm22$	-
	$\rho=2.2\pm0.4$	$\rho=2.1\pm0.3$	$\rho=3.1\pm0.2$	
N23	$D_{10}=154\pm9$	$D_{10}=204\pm9$	$D_{10}=364\pm22$	$D_{10}=775\pm22$
	$\rho=2.3\pm0.4$	$\rho=2.2\pm0.3$	$\rho=3.5\pm0.6$	$\rho=3.9\pm0.3$
N25	$D_{10}=158\pm9$	$D_{10}=217\pm9$	$D_{10}=353\pm22$	$D_{10}=676\pm22$
	$\rho=2.2\pm0.4$	$\rho=2.1\pm0.2$	$\rho=2.5\pm0.5$	$\rho=4.2\pm0.4$
A26	$D_{10}=157\pm9$	$D_{10}=198\pm9$	$D_{10}=328\pm22$	$D_{10}=702\pm22$
	$\rho=2.3\pm0.4$	$\rho=2.4\pm0.3$	$\rho=2.3\pm0.5$	$\rho=6.8\pm0.3$
N26	$D_{10}=155\pm9$	$D_{10}=201\pm9$	$D_{10}=366\pm22$	$D_{10}=705\pm22$
	$\rho=2.3\pm0.4$	$\rho=2.0\pm0.3$	$\rho=3.1\pm0.5$	$\rho=3.6\pm0.3$
N26D	$D_{10}=153\pm9$	$D_{10}=201\pm9$	$D_{10}=411\pm22$	$D_{10}=768\pm22$
	$\rho=2.6\pm0.4$	$\rho=2.2\pm0.3$	$\rho=1.5\pm0.5$	$\rho=3.6\pm0.3$

Comments:
1) The sign (-) means the absence of particles in given sieved fraction.
2) The error of particle size measurement is estimated as a half of histogram size interval.
3) The error of density measurement is estimated taking into account the errors in particle size and weighing accuracy which is equal to 0.00015 g (scale characteristic).
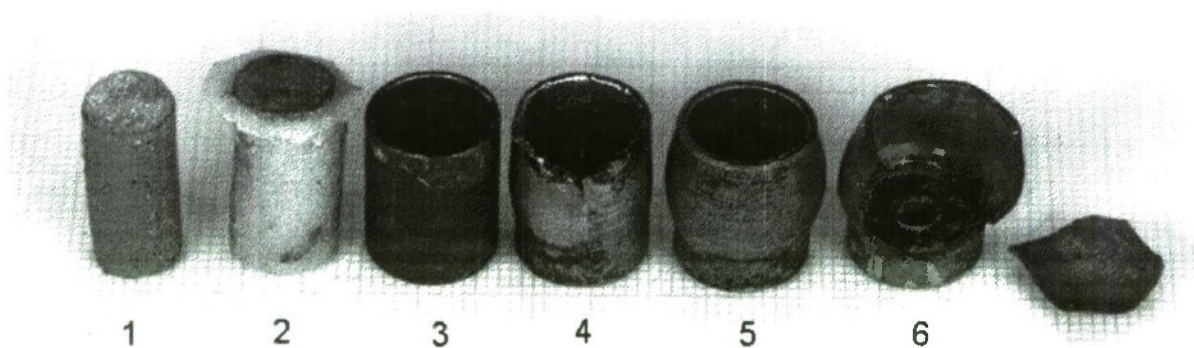
Fig. 3.10. The damage of specimen holder in combustion of samples with 100% replacement of commercial aluminum by Alex (batch #21):

1   -   propellant specimen before inhibiting,
2   -   propellant specimen inhibited by epoxy glue,
3   -   non-damaged sample holder (cylinder with wall of 1 mm thick made of bronze),
4, 5, 6   -   damaged holders.

Note: The propellants specimen geometry in this figure corresponds to geometry used in sampling bomb. Inhibited with epoxy glue specimens and sample holders have been used in the bomb intended for burning rate evaluation.

The basic tendencies revealed in agglomerate characteristics behavior are briefly described below.

3.7.2. Replacement of aluminum by Alex and overal agglomeration intensity.

Analysis of experimental data reported in Tables 3.3, 3.5, 3.6 and in Figs. 3.11-3.13 shows that replacement of commercial aluminum by Alex leads to increase of burning rate, decrease of agglomeration intensity and increase of metal conversion degree. For propellants without HMX the characteristic sizes D_{mn} for different propellants do not differ significantly (excluding propellant #22) and increase of metal completeness is achieved mainly due to decrease of mass fraction of agglomerates. The most pronounced example of such behavior demonstrates propellant #21 where ratio $m_f{:}m_{ag}$ amounts 99:1 (series N21) and 98:2 (series A21), see Fig. 3.11.

The listed above trends are most expressed in combustion of HMX containing propellants which exhibit, as a rule, initially higher agglomeration intensity as compared with pure AP based propellants, Fig. 3.12. Indeed, free aluminum percentage in CCP for propellant N22 is 3 times higher ($[Al_{ccp}]$=11.7%) than that for propellant N19 ($[Al_{ccp}]$=3.9%), Table 3.4. So as the sizes D_{mn} for these propellants are similar the higher incompleteness is the result of bigger mass of agglomerates in the case of propellant N22, see Fig. 3.13.

It is noteworthy to underline that in the case of HMX propellants even small amount of Alex in propellant formulation gives sizable effect in terms of agglomeration behavior (propellant N25).

Note that for all studied propellants the one of the main parameters that characterizes the agglomerate intensity, namely, dimensionless mass of agglomerate m_{ag}, demonstrates practically inversely proportional dependence on burning rate, Fig. 3.15.
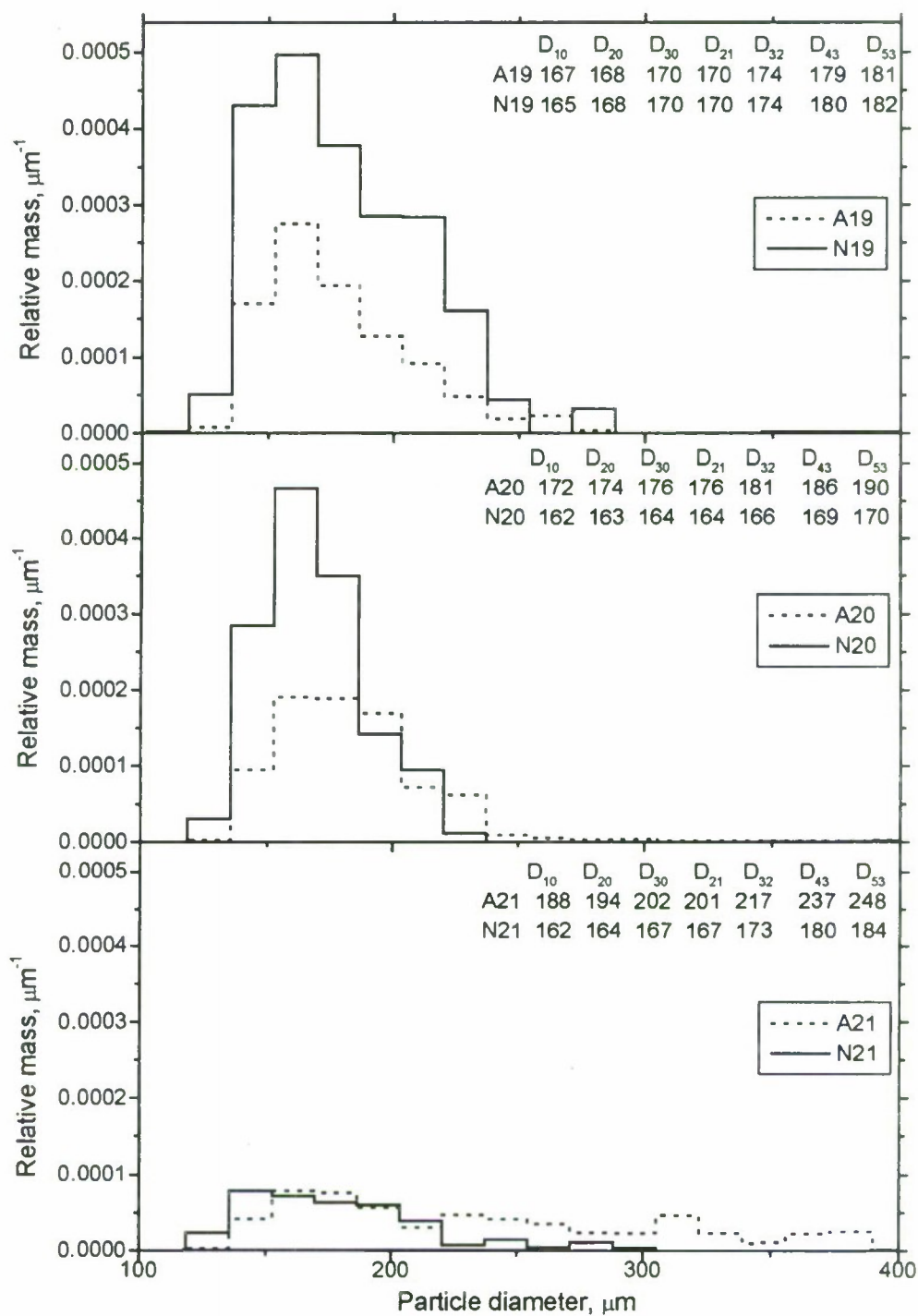
Fig. 3.11.

Mass size distribution and characteristic size for agglomerates in series N19-N20-N21 and A19-A20-A21. The influence of replacement of commercial aluminum by Alex in the case of formulations without HMX.
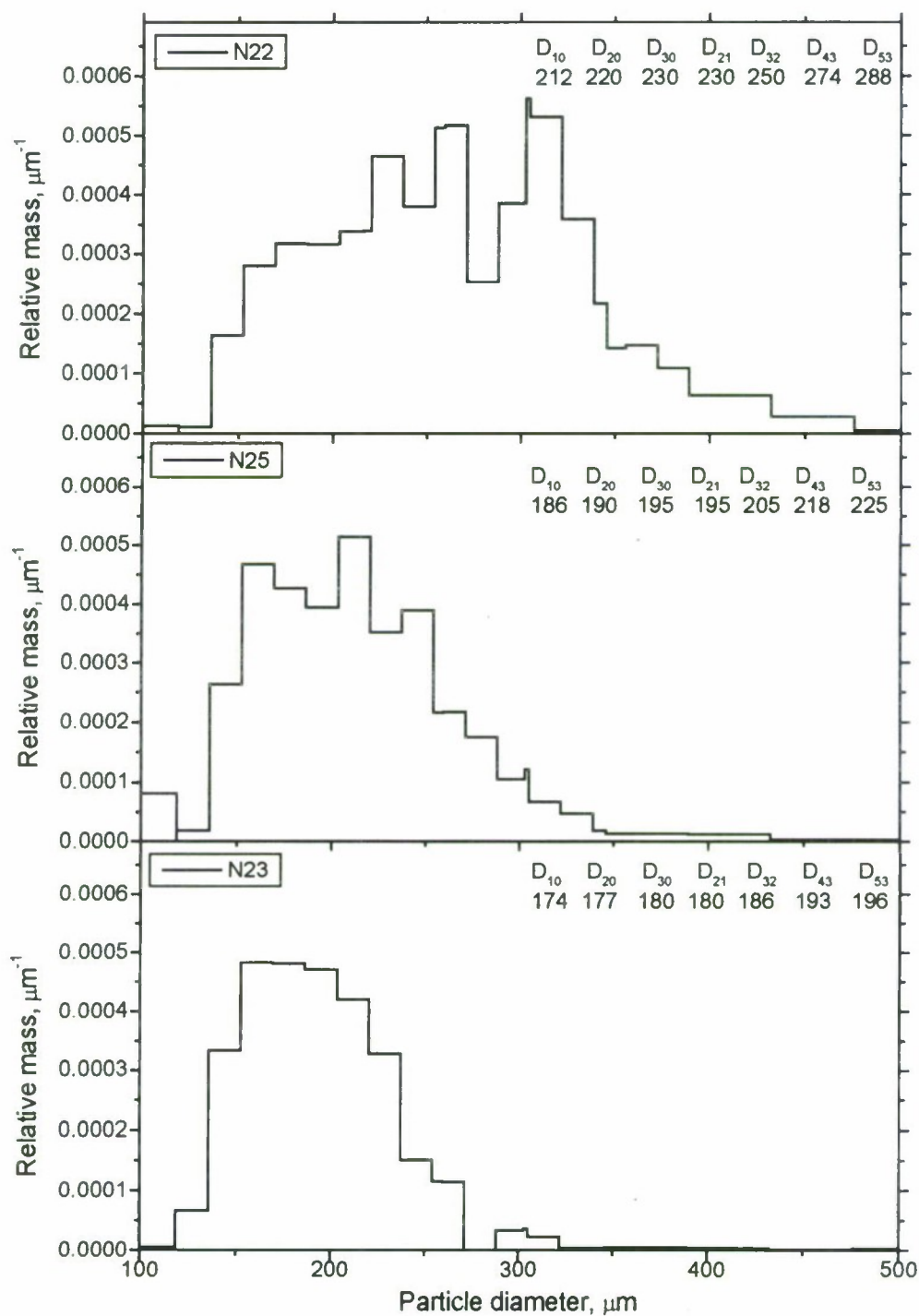
Fig. 3.12. Mass size distribution and mean diameters for agglomerates in series N22-N25-N23. The influence of replacement of commercial aluminum by Alex in the case of HMX-containing formulations.
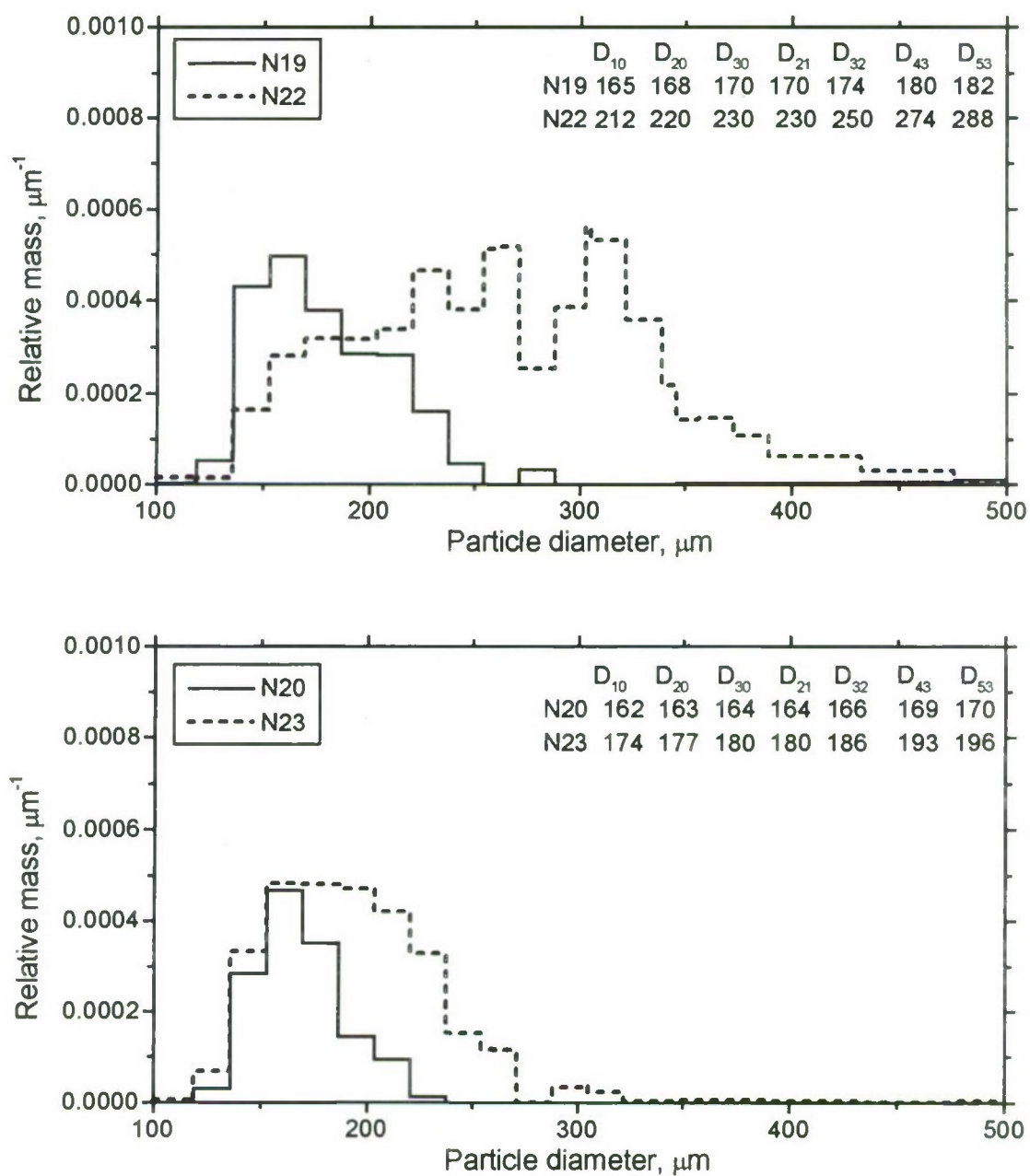
Fig. 3.13. Comparison of agglomeration intensity for the propellant formulations without HMX (N19, N20) and HMX-containing (N22, N23). Alex/Al =0/100 in series N19 and N22, Alex/Al =30/70 in series N20, N23.
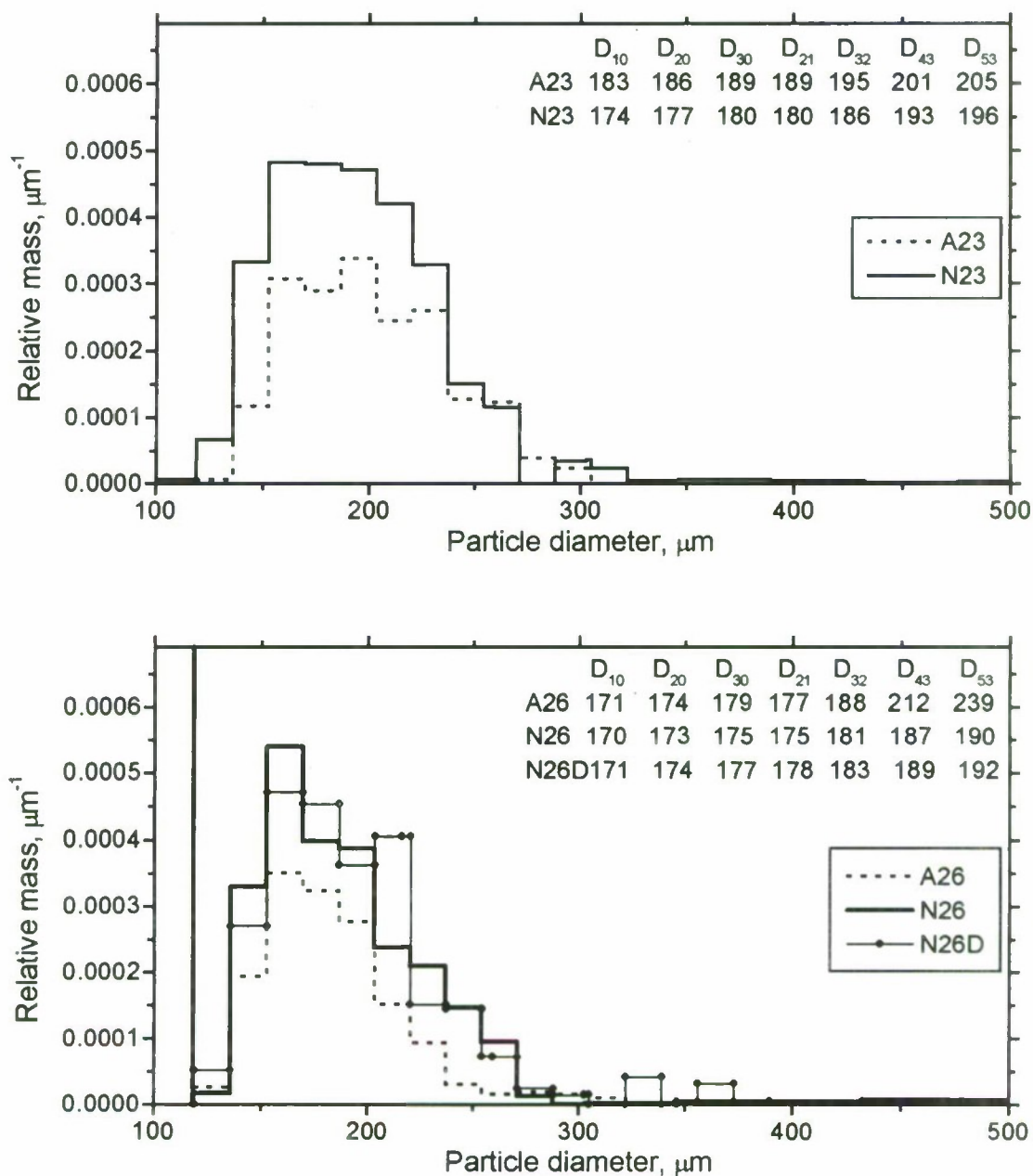
Fig. 3.14. Comparison of agglomerate size distribution histograms and mean diameters obtained in combustion experiments with argon and nitrogen in the case of the HMX-containing propellant formulations. Analogous comparison for the propellant without HMX has shown in Fig. 3.11.

Combustion runs in series N26 and N26D were performed under identical experimental conditions to estimate the scatter of experimental data.

Fig. 3.15. Unified dependence of agglomerate mass on burning rate.

Two round shape circled points corresponding to series N26 and N26D performed under same conditions give estimate for reproducibility of experimental data.

3.7.3. The influence of gaseous environment

Analyzing experimental data in Tables 3.3, 3.5, 3.6 and in Figs. 3.11, 3.14 one can see that in all cases the experiments in argon give lesser value of a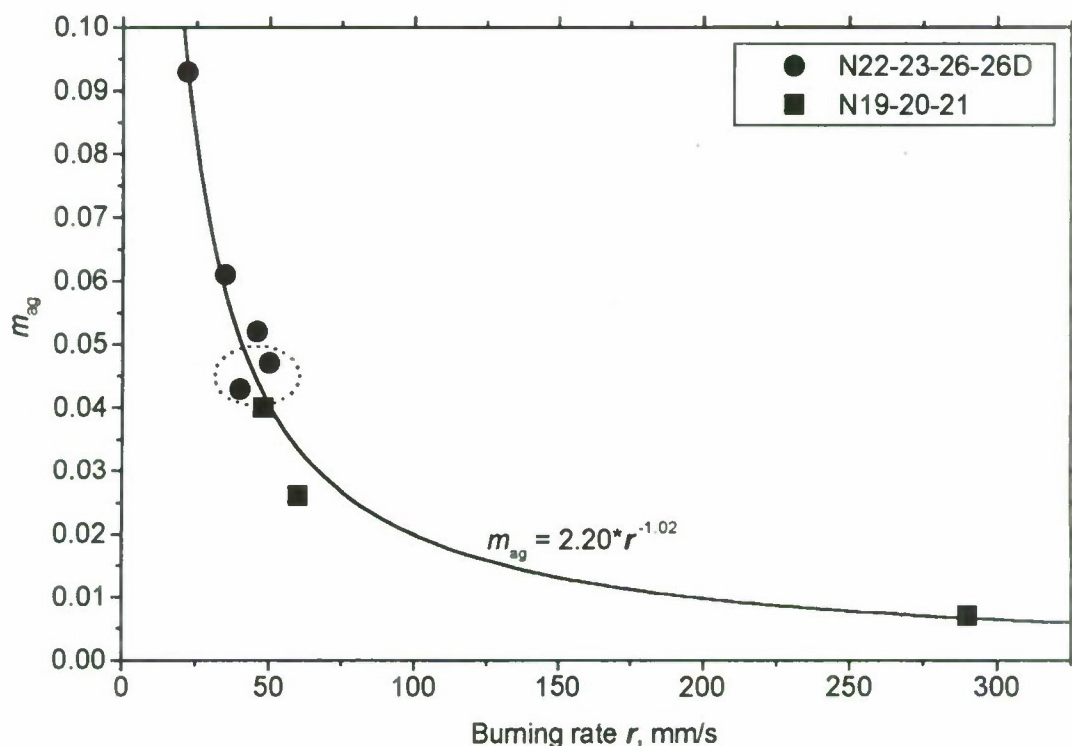gglomerate mass as compared with the experiments in nitrogen though the propellant burning rates practically coincide (in series A20, N20 and A26, N26). In this case a noticeable difference in agglomerate sizes is not observed. The nature of this phenomenon is not clear.

3.7.4. The reproducibility of experimental data.

The above mentioned Tables 3.3, 3.5, 3.6 and in Fig. 3.14 illustrate the reproducibility of common experimental procedure including firing test, particle size and chemical analyses. The burning rate magnitude and the major weight parameters can be characterized as not very good reproducible (compare series made in argon and in nitrogen, #19-23, and N26 and N26D). The difference in burning rates is caused not by environmental gas but by porosity of laboratory scale propellant samples.

As it was mentioned in Section 3.3, the scatter of weight parameters is caused by the contamination of sampled condensed products with vacuum oil used for inhibiting the lateral surface. The total mass of the oil covering three samples which have been fired in series was about

0.17÷0.20 g that contributes 5% of the mass of propellant burnt or 10-17% of the mass of CCP. Besides, the oil mass depends on roughness of the sample surface. Thus, using "soft" inhibiting material was found to be not free of imperfections as compared with the "hard" inhibiror such as teflon, plexiglas or epoxy glue. The imperfection consists in contamination of sampled products. However, there are the following advantages of soft inhibitor: contamination does not affect the size distribution of particles and it does not affect mass characteristics of agglomerates. One can see in Tables 3.3 and 3.5 that values m_{ag}, m^{Al}_{ag}, m^{Al}_{ccp} in series N26 and N26D have fairly good reproducibility.

3.7.5. The fine Al-type effect.

The series N23 and N26 are distinguished by the type of fine aluminum powder used in propellant manufacturing. The particle size distribution and aluminum content for original Alex and UFA powders were close. Actually, no considerable difference in agglomerate behavior has been observed, see Tables 3.3-3.7 and Fig. 3.14. No specific features of different chemical reactivity of Alex and UFA were detected.

3.8. Characteristics of the fine CCP particles.

3.8.1. Particle chemical and size distribution analyses data.

In accordance with division of total CCP particles into agglomerates and fine particles, the particles with size lesser than D_L are considered in this Section.

The main weight characteristics of fine particles and their contribution into total CCP mass are shown in Table 3.8. First of all it should be noted that in all cases the unburnt aluminum content $[Al]_f$ does not exceed 0.8%. Thus, the fine CCP particles consist mainly of oxide formed in course of aluminum burn out. The ratio of fine particle and agglomerate masses $m_f:m_{ag}$ varies from (69:31) to (99:1). At the same time the ratio of free aluminum mass contained in fine particles and in agglomerates, $(m_f:m_{ag})$, for most series varies from (6:94) to (16:84). The propellant sample with total replacement of commercial aluminum by Alex (series A21 and N21, shadowed lines in Table 3.8) exhibit exceptional behavior due to extremely low agglomerate mass and mass contribution of agglomerates into total mass of CCP, $m_f:m_{ag}$ = 98:2 and $m_f:m_{ag}$ = 99:1 for series A21 and N21, respectively.

Table 3.8. Weight characteristics of fine particles among whole sampled CCP.

Series	D_L, μm	m_f	m^{Al}_f	$[Al]_f$	$m_f:m_{ag}$	$m^{Al}_f:m^{Al}_{ag}$
A19	34	0.497	0.0010	0.2%	97:3	10:90
N19	55	0.331	0.0010	0.3%	89:11	7:93
A20	24	0.359	0.0009	0.3%	96:4	14:86
N20	55	0.263	0.0006	0.3%	90:10	6:94
A21	34	0.432	0.0012	0.3%	98:2	80:20
N21	24	0.535	0.0022	0.4%	99:1	76:24
N22	118	0.204	0.0013	0.6%	69:31	4:96
A23	34	0.332	0.0019	0.6%	91:9	15:85
N23	118	0.381	0.0011	0.3%	88:12	7:93
N25	118	0.245	0.0019	0.8%	80:20	7:93
A26	55	0.258	0.0020	0.8%	90:10	16:84
N26	118	0.409	0.0013	0.3%	90:10	12:88
N26D	118	0.324	0.0014	0.4%	88:12	9:91

The size distribution of small particles (sieve fraction < 130 μm) was analyzed with commercial sizer Malvern 3600E using acetone as carrier liquid. The suspension was preliminary treated during 40 seconds by ultrasound and then was mechanically mixed in course of measurement. The total size range 0.5-118.4 μm was divided into 16 channels with exponential increment of sub-range width. The correspondence between size range and its number was shown in Table 3.2. Left bound (0.5 μm) of the first interval has conventional meaning.

In all cases the mass size distribution of fine particles has three characteristic peaks or local maxima which are usually observed for most aluminized propellants [3, 39, 41], Fig. 3.16. Typically these peaks are located in 2nd (1.2-1.5 μm), 6th (3-3.9 μm) and 9th (6.4-8.2 μm) histogram size intervals. The experimental data on fine CCP particles size distributions are presented in Figs. 3.17-3.20 and characteristic sizes D_{mn} calculated in size range 0.5 –118 μm are presented in Table 3.9. Here the value D_L was chosen equal to 118 μm for uniformity. In some cases the relative mass in size range 24-118 μm was zero and using of such option did not play noticlble role. The size range where $f(D)$ =0 is reported in last column of Table 3.9.

Below we will analyze the behavior of oxide particles for different propellant formulations and for two gases – argon and nitrogen – used for bomb pressurization. Remember that all experiments have been carried out at the same pressure about 46 atm.
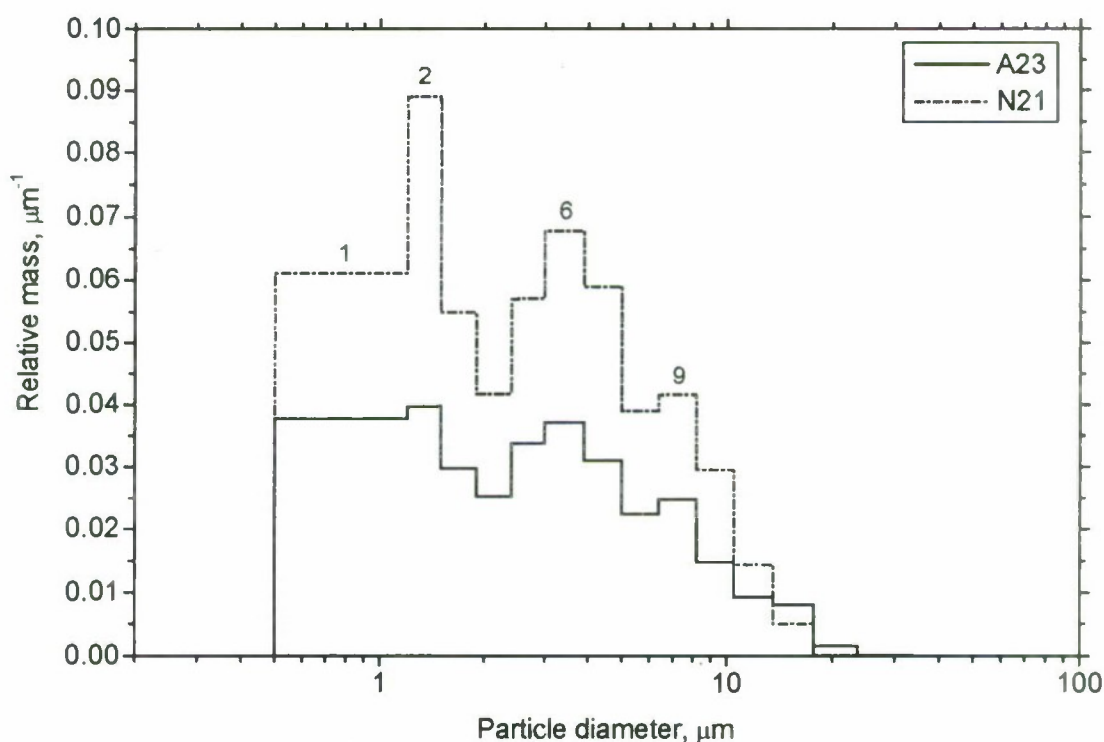

Fig. 3.16. Characteristic peaks on mass size distributions for fine oxide particles. The figures above the curve are the numbers of size interval in Malvern histogram.

Table 3.9.
Mean diameter D_{mn} (μm) of fine CCP particles calculated in the size range 0.5 –118 μm.
The last column reports the size range (μm) where value of mass distribution function $f(D)$
was equal to zero.

Series	D_{10}	D_{20}	D_{30}	D_{21}	D_{32}	D_{43}	D_{53}	$f(D) = 0$ within:
A19	1.1	1.4	1.9	1.7	3.7	7.1	8.5	34-118
N19	1.1	1.3	1.9	1.6	3.8	8.5	10.9	55-118
A20	1.1	1.3	1.7	1.5	2.7	5.4	6.8	24-118
N20	1.3	1.7	2.4	2.3	4.6	8.5	10.6	55-118
A21	1.1	1.3	1.7	1.6	3.1	6.1	7.7	34-118
N21	1.1	1.4	1.8	1.6	3.2	5.8	7.0	24-118
A23	1.1	1.3	1.8	1.6	3.4	6.9	8.6	34-118
N23	1.3	1.8	2.7	2.5	6.2	13.2	16.8	-
N25	1.4	1.9	3.0	2.7	7.5	18.5	24.7	-
N22	1.3	1.8	2.8	2.5	7.1	17.0	21.8	-
A26	1.1	1.3	1.8	1.6	3.4	7.8	10.0	55-118
N26	1.4	2.1	3.7	3.1	11.5	34.5	44.7	-
N26D	1.4	2.0	3.4	2.9	10.0	32.5	43.6	-

The features of fine oxide particles behavior can be summarized as follows:

1) Three-peak structure of mass size distribution of oxide particles remains the same independently of aluminum type (Alex/Al mixture, UFA/Al mixture, pure Al, pure Alex), Figs. 3.17-3.20.

2) In general, the higher aluminum conversion degree, the greater oxide mass in total mass of CCP. In another words, m_f increases with reduction of agglomerate mass m_{ag} and with reduction of incompleteness of aluminum combustion $[(m^{Al}_{ccp}) / (m^{Al}_{prop})]$. The last quantity decreases with burning rate. In the case of experimenting in nitrogen, with consecutive replacement of aluminum by Alex the incompleteness of aluminum combustion $[(m^{Al}_{ccp})/(m^{Al}_{prop})]$ decreases monotonously and mass size distribution $f(D)$ transforms so as at first the right tail becomes shortly and then the magnitude of function $f(D)$ increases in the size range 0.5-1.9 μm, see Figs. 3.17-3.18. This trend takes place for both propellant type - with HMX and without HMX - and caused a specific behavior of mean size D_{43}. that is presented in Fig. 3.21 as the function D_{43} *versus* $[(m^{Al}_{ccp})/(m^{Al}_{prop})]$. Remember that the mean diameter D_{43} is proportional to the mass content in each histogram size interval.

3) For the propellant composition #26 based on UFA the mass size distribution function $f(D)$ has elongated right hand side tail as compared with another series, see Fig. 3.20. This induces abnormally high value of characteristic size D_{43} (see Table 3.9 and two points corresponding to the series N26 and N26D in Fig. 3.21). The reason for such behavior is nor really clear.

4) When the combustion experiments are carried out in argon instead of nitrogen, the function $f(D)$ changes. Namely, in most cases right hand side tail becomes shorter and the

magnitude of function $f(D)$ increases in the size range 0.5-1.9 μm, see Figs 3.17 and 3.20. The mechanism of this influence in not clear.

In Table 3.10 the thermodynamic calculation data made using Russian computer code ASTRA-3 are presented. These data are supplemented by the data on argon and nitrogen properties taken from handbook [42]. It is hard to find any sizable distinctions in combustion product characteristics and in environmental gas parameters that may induce the disparity in combustion mechanism or in freezing rate for aluminum particles.

Table 3.10. Thermodynamics data on combustion products (calculated at 44 atm) and reference data for argon and nitrogen properties.

Combustion products	Batch #19	Batch #22
Flame temperature T_{gp}, K	3752	3697
Viscosity μ, Pa·s	$0.92226 \cdot 10^{-4}$	$0.86133 \cdot 10^{-4}$
Molar mass M_{gp}, g/mol	22.376	20.183
Heat capacity C_p, kJ/(kg·K)	1.9027	1.8418
Mass fraction of substances:		
Condensed products (total)	0.32244	0.30871
Condensed Al_2O_3	0.32244	0.30871
AlN	$0.21635 \cdot 10^{-6}$	$1.7398 \cdot 10^{-6}$
O_2	$0.11201 \cdot 10^{-1}$	$0.48234 \cdot 10^{-3}$
H_2O	0.25787	0.11154
H_2	0.12466	0.23061
HCl	0.12878	0.04875
N_2	0.11468	0.19860
CO	0.14449	0.28044
CO_2	0.03450	0.01579
Al	$0.12751 \cdot 10^{-3}$	$0.82510 \cdot 10^{-3}$

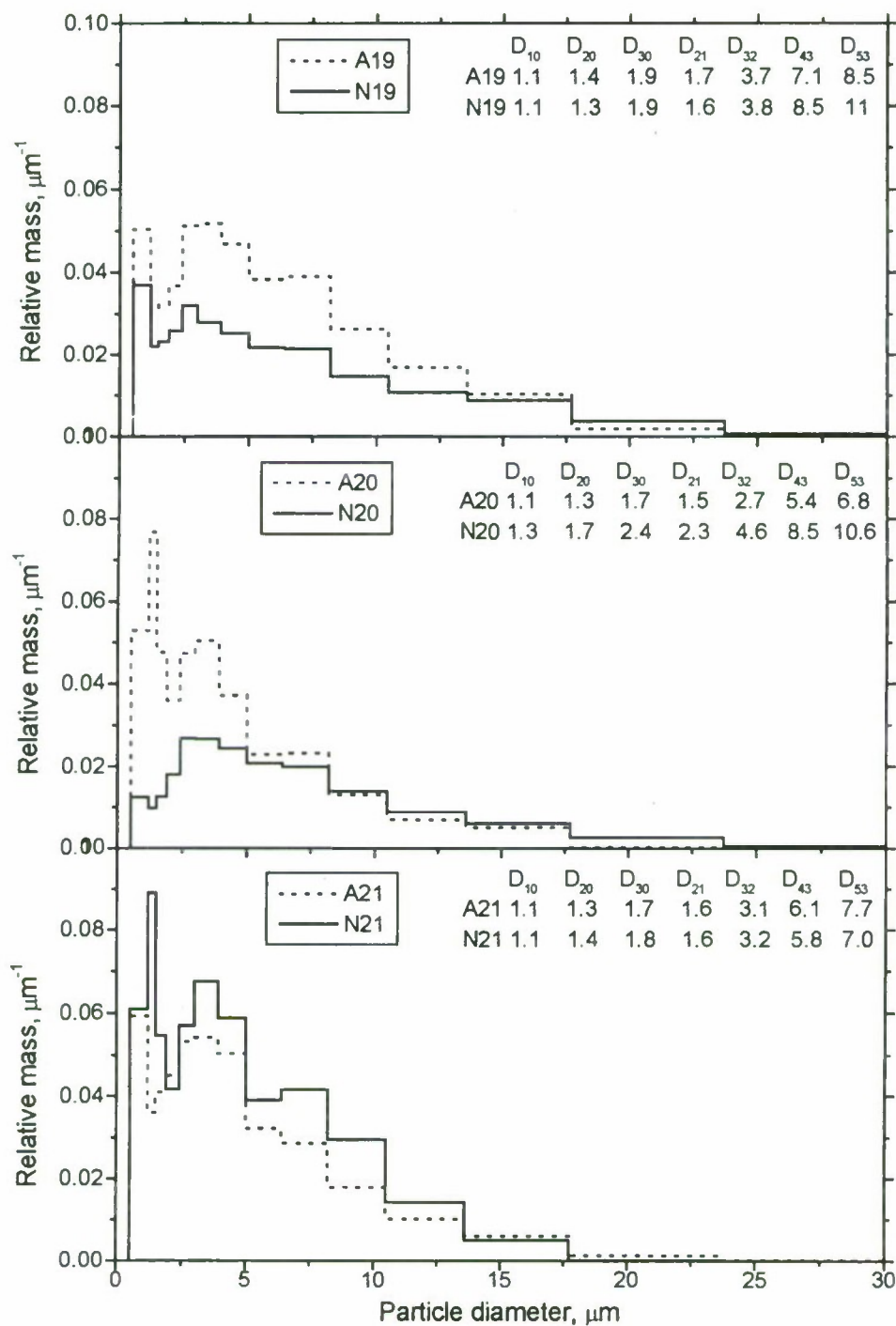| Environmental gas properties	Argon	Nitrogen
Molar mass, g/mol	39.95	28
Heat capacity c, kJ/(kg·K) at 100 atm, 1000 K	0.535	1.176
Thermal conductivity λ, 10^{-3} ·W/(m·K) at 100 atm, 1000 K	0.0449	0.0666
Density ρ, kg/m³, at 1 atm, 273 K	1.7837	1.2506

Fig. 3.17. Mass size distribution of fine CCP particles and characteristic sizes D_{mn} calculated in size range 0.5-118 μm for propellant formulations without HMX. The proportion of Al/Alex in propellant and environmental gas used in firing tests has been varied.

Alex/Al = 0/100, 30/70, 0/100 in series #19, 20, 21, correspondingly.

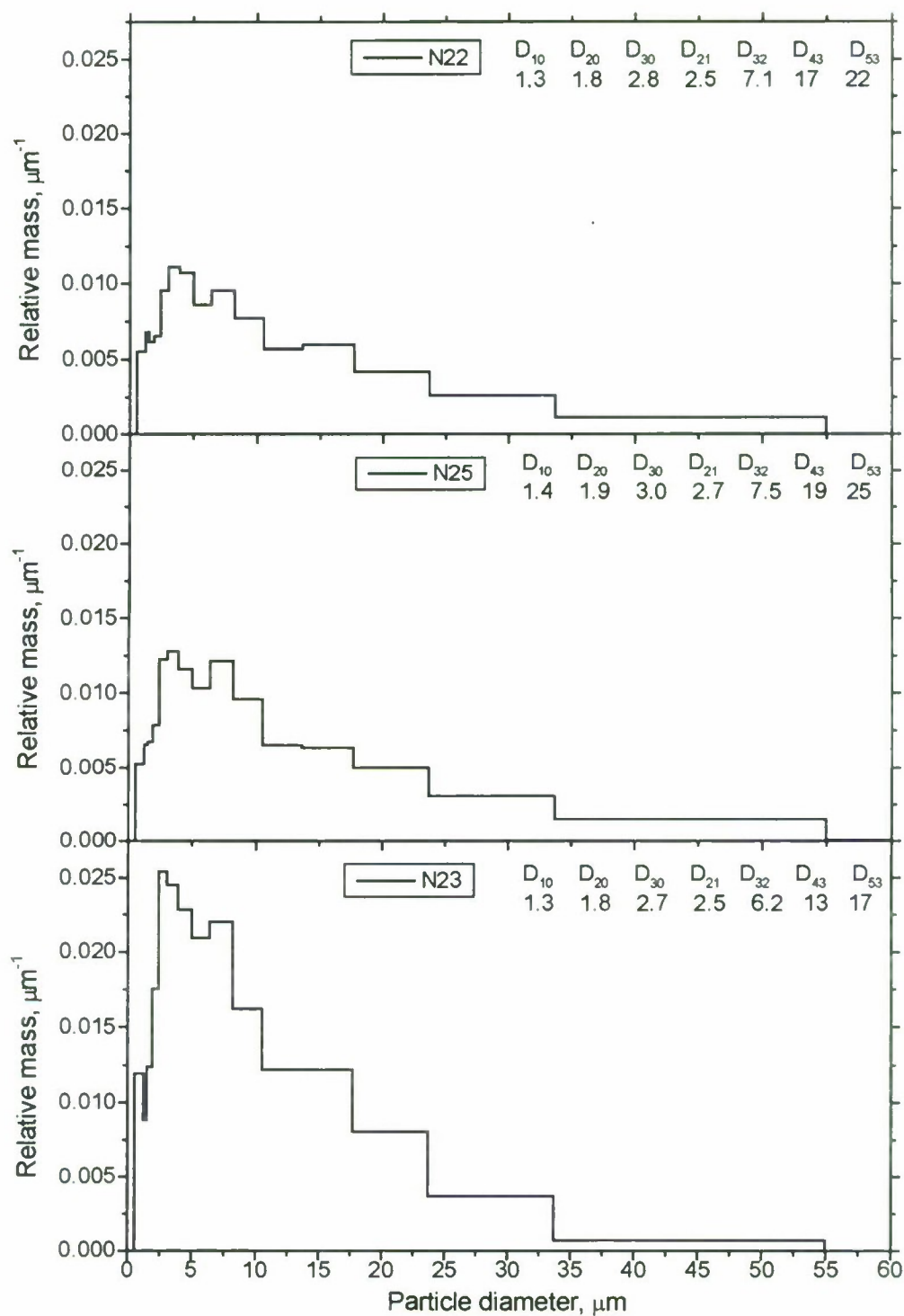"A" series were performed in argon, "N" series – in nitrogen.

Fig. 3.18. Mass size distribution of fine CCP particles and characteristic sizes D_{mn} calculated in size range 0.5-118 μm for HMX-containing propellant formulations. All experiments were conducted in nitrogen. The proportion of Al/Alex in propellant has been varied:

Alex/Al = 0/100, 8.3/91.7 and 30/70 in series N22, N25 and N23, correspondingly.
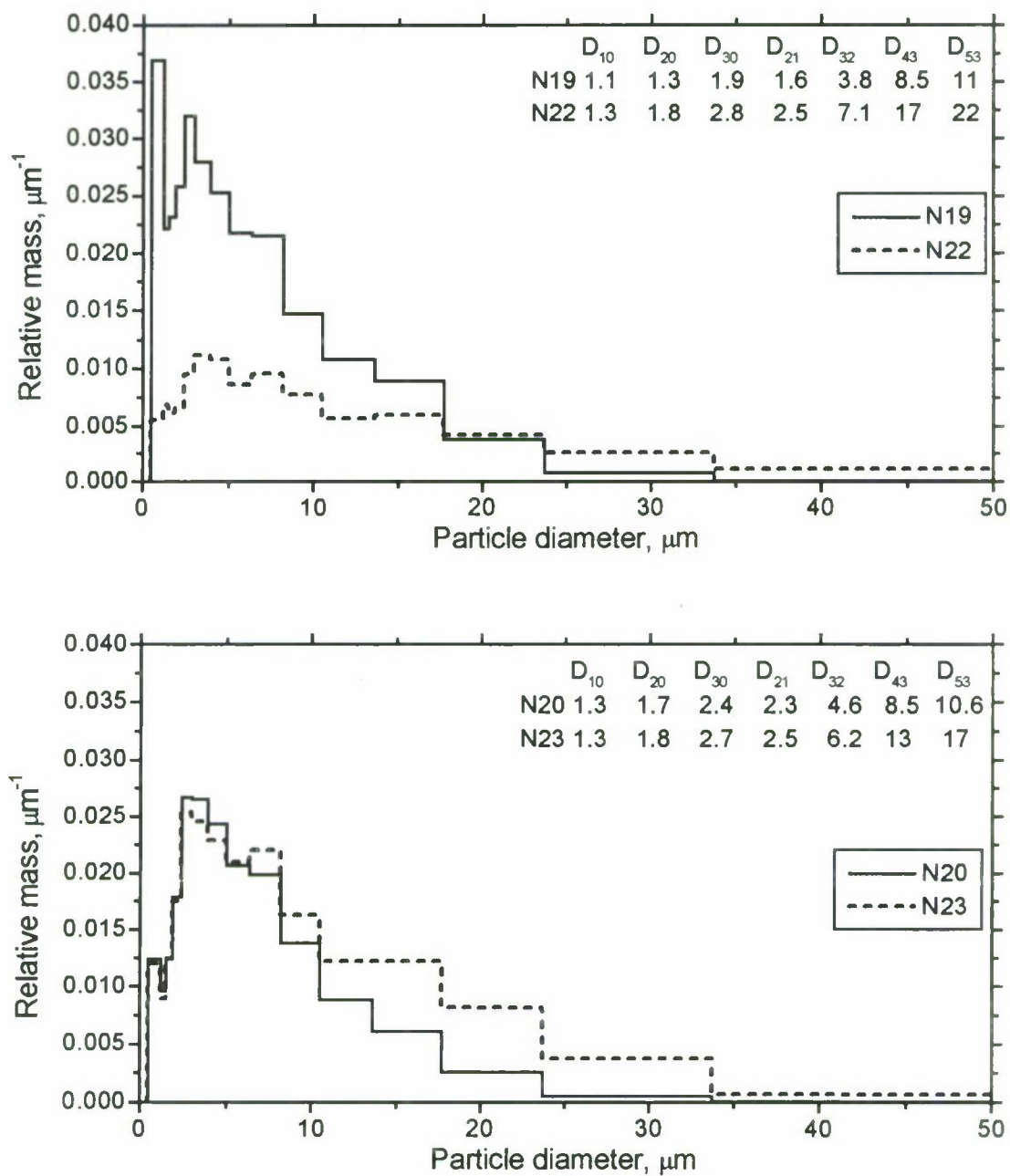
Fig. 3.19. Comparison of mass size distribution of fine CCP particles and characteristic sizes D_{mn} calculated in size range 0.5-118 μm for propellant formulations without HMX (series N19, N20) and HMX-containing propellant formulations (N22, N23). All experiments have been made in nitrogen. The proportion of Al/Alex in propellant has been varied:

Alex/Al = 0/100 in series N19 and N22, Alex/Al = 30/70 in series N20 and N23.
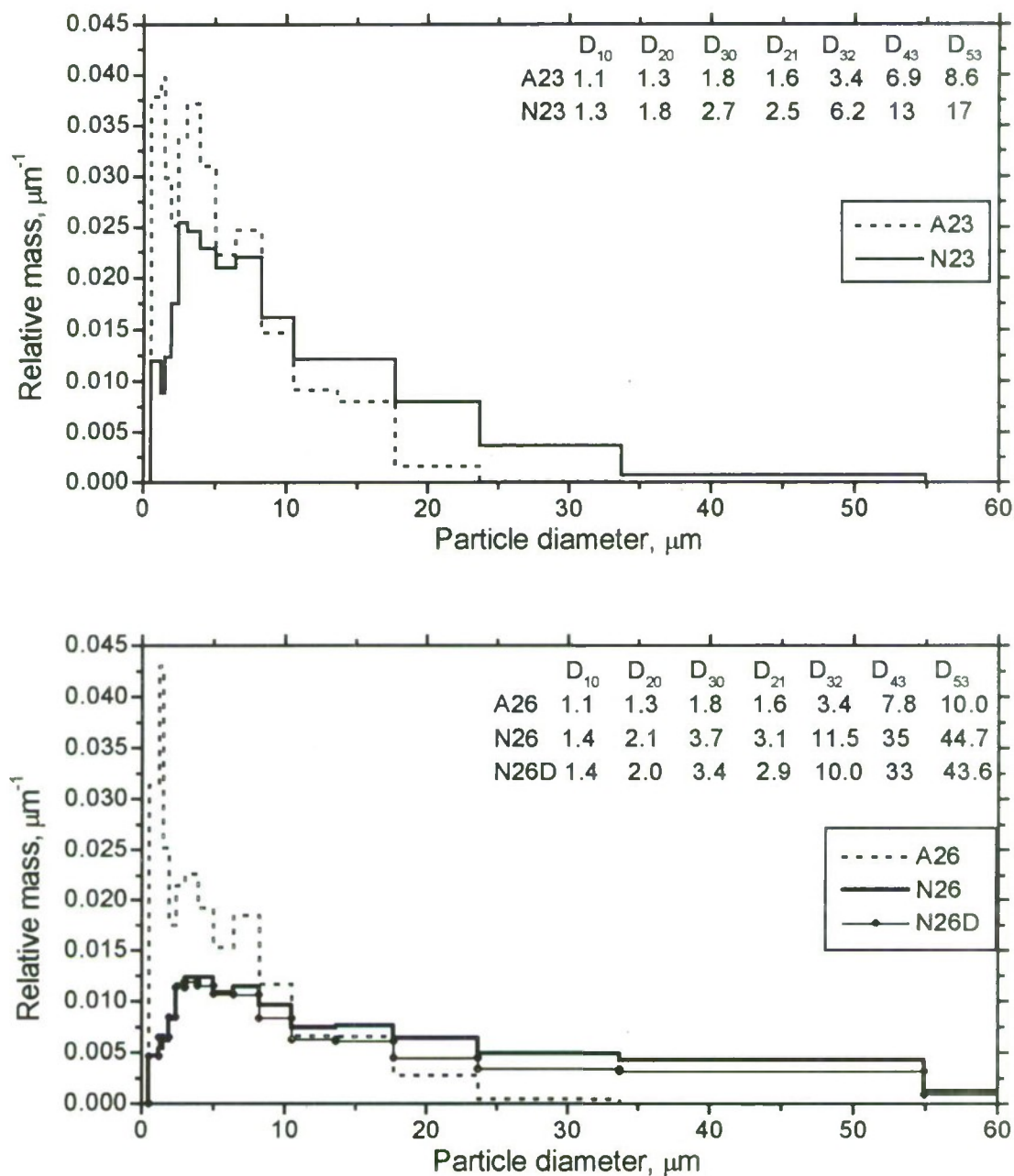
Fig. 3.20. The effect of environmental gas and type of fine aluminum particles on mass size distribution of fine CCP particles and characteristic sizes D_{mn} calculated in size range 0.5-118 µm. The proportion of Al/Alex (or Al/UFA) was 30/70 in all pictured series. The letters A or N in series identifier mean argon or nitrogen environment, in series N26 and N26D UFA was used instead Alex. Series N26 and N26D were performed at identical conditions.
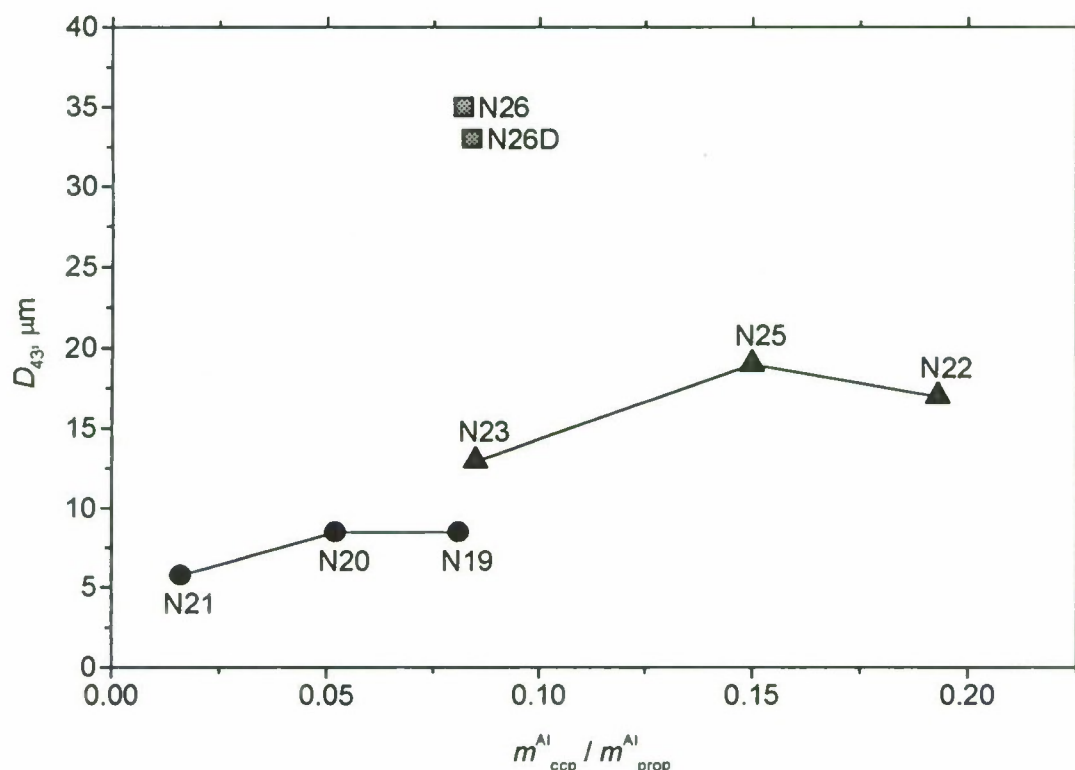
Fig. 3.21. Correlation between mean diameter of fine oxide particles D_{43} and incompleteness of aluminum combustion $[(m^{Al}_{ccp})/(m^{Al}_{prop})]$ for all series made in nitrogen.

D_{43} is calculated in size range 0.5-118 μm. In series N26 and N26D UFA has been used instead of Alex.

3.8.2. Advanced analyses – chemical composition and X-ray diffraction data

Along with ordinary chemical analysis for determining metallic aluminum content made by permanganatometric method [4], the advanced analysis was performed for fine CCP particles to determine the nitrogen compounds.

For qualitative detecting the nitride nitrogen, the method based on ammonia distillation was used [36]. For quantitative measurement of the nitride nitrogen content the method developed by Kehedal [36] was applied.

Additionally, X-ray diffraction measurement was performed. The commercial diffractometer for powder materials Philips APD1700 equipped with a copper source (Cu K_{α}, U= 40 kV, I=35 mA) was used. The following option was used: geometry – Bregg-Bretano, automatic divergence slit, graphite monochromator. Measurements were performed between 5° and 80°, step size – 0.02-0.03°, time of signal accumulation – 1-3 s, experiment duration 120 min. The peak location was determined automatically by maximal intensity of diffracted rays using software APD1700 (SANDMAN code) or manually using data tables JCPDS.

Note that nitrogen in nitride form has been detected chemically in virgin fine aluminum powder. Presumably, this compound was presented in virgin powder in X-ray-amorphous form because no reflexes, except metallic aluminum, were found in X-ray diagnostics.

Nitrogen in nitride form was also detected in CCP (sieved fraction < 130 μm) both in series made in argon and in nitrogen. Obtained X-ray patterns are similar within all series. The presence of following phases has been analyzed: NH_4ClO_4, metallic Al, Al_2O_3 (all modifications), AlN, AlON, $Al_xO_yN_z$ (css), Al_4C_3, Al_2OC, C (graphite), $Al_xO_yC_x$ (css), $Al_xO_yN_zC_u$ (css). Here (css) means the phase with varied compositions, i. e. coring solid solution. Actually, no Al, graphite, carbides and oxicarbides phases was detected.

The identification of the phases with small content (<2-5 % mass.) was practically impossible due to following difficulties in data treatment:

- Bad crystal structure of samples (X-ray amorphopusness).
- Close location of the bands for oxide and nitride phases.
- Presence of the phases in the form of coring solid solutions.

Considerable amount of nitrogen compounds was found by chemical analysis in the fine fraction of CCP. However, the X-ray diffraction measurements showed that at least part of this nitrogen is due to the presence of ammonium perchlorate (AP) in CCP. It was checked by special tests. After washing samples on Buchner funnel with hot water, the mass lost equals to 35-54% that can be treated as the presence in CCP of some other soluble species besides AP. No AP is detected after washing. Nevertheless, the nitride nitrogen has been detected in the probe after washing and drying.

Chemical analysis data are presented in Table 3.11. The analysis does not allow to say in which form the nitrogen is presented. Therefore only assumed amount of nitrogen compounds content is presented in last column of the Table. The results for pure Alex used in propellant manufacturing are presented in the bottom line of Table. One can see that the maximal nitrogen content is found in series N19 and N26 and in most cases the nitrogen content in condensed products exceeds this value for Alex before burning.

The X-ray diffraction data are presented in Table 3.12. The problems of data interpretation are mentioned above. Remind that metallic aluminum, graphite, carbide and oxicarbide phases were not detected in X-ray diffraction measurements. The observed reflexes are produced by various aluminum oxide modifications. Some data can be treated as small content of AlN or AlON but their real presence is still questionable. The angle of maximal reflection intensity $2\theta = 45.81^0$. It can be presumably attributed to oxinitride. However, this band does not directly correspond to the reference data [37, 38] for nitride and oxinitride phases. Nevertheless, in all cases there is detected remarkable reflex with this angle.

Generalizing the X-ray and chemical analyses data one may conclude:

- The presence of nitride phase in CCP is negligibly small in both environmental gases (argon and nitrogen).
- Slightly increased quantity of nitride in series N19 and N21 can be caused by some other reasons than burning environment.
- No evident correlation between nitride presence and mass size distribution function behavior has been observed.

Table 3.11. Nitrogen content (% mass.) in fine CCP (sieved fraction < 130 μm)

Sample/series	Mass lost when washing, %	Measured nitrogen content, %	AlN or AlON calculated, %
A19	38	0.27	0.78 or 1.10
A21	54	0.19	0.56 or 0.77
N19	39	0.59	1.73 or 2.40
N20	40	0.18	0.53 or 0.73
N21	35	0.23	0.67 or 0.94
N26	38	0.76	2.11 or 2.93
Virgin Alex		0.20	0.63 or 0.80

Table 3.12. Results of X-ray diffraction measurements for phase analysis

Sample/series	γ-Al$_2$O	α- Al$_2$O$_3$	δ- Al$_2$O$_3$	AlN	AlON (?)
A19	++	+	−	−	45.73^0
A21	+	++	−	−	45.82^0
N19	++	+	−	+	45.83^0
N20	+	+	+	+	45.76^0
N21	+	++	+	−	45.87^0
N26	+	−	−	+	45.80^0

Comments:
+   low content of given phase.
++   high content of given phase.
−   phase has not been detected.
In last column the diffraction angle corresponding to maximal intensity is presented.

4. THERMAL DECOMPOSITION STUDY

4.1. Experimental approach

Study of thermal decomposition of binders and based on them propellants was undertaken in order to better understand physicochemical mechanism of Al agglomerates formation and evolution. Two heating rates were used in the study: 10 K/min (classical approach) and 300-700 K/s (laser flash-thermolysis). The composition of materials under study is shown in Tables 4.1 and 4.2.

Table 4.1. Formulation of binders studied (% mass)

	A1	A2	A3
Isoprene rubber	26.4	-	-
Polibutadiene rubber	-	19.2	-
Nitryl rubber	-	-	13.7
Transformer oil	69.6	76.8	-
DEGDN	-	-	84.3
Curing agent	4.0	4.0	4.0

Comments: DEGDN = diethylene glycol dinitrate,
Transformer oil = distilled oil fraction with boiling temperature T_b =300-400°C,
Curing agent = quinol ester

Table 4.2. Formulation of propellants studied (% mass)

	P1	P2	P3
Binder A1	23.8	-	
Binder A2	-	23.6	-
Binder A3	-	-	42.6
Al (d_{30}=14μ)	28.6	26.4	42.6
AP (6000 cm^2/g)	42.9	50.0	14.8
Catalyst	4.7	-	-

Comments: AP =ammonium perchlorate, catalyst = ferrocene based compound.

Mixing the components with total mass of 5 g was made in teflon® cup. After mixing the mass was kept under moderate vacuum during 4-5 hours at T=80 °C in order to remove gaseous bubbles from the bulk of material. After vacuum treatment the polymerization was performed under atmospheric pressure in air at T=80 °C during 5 days. Curing was performed using quinol ester.

In slow heating rate DTA-TG experiments the 1 mm thick slices of polymerized samples of 150 mg mass were used. In fast heating rate experiments the specially prepared films of materials under study of 110-180 μm thickness were used. With this thickness the temperature drop across the polymer film did not exceed 25-50 K at heating rates 300-500 K/s.

The procedure for manufacturing thin films was as follows. First, the plastic (Lavsan®) spacer was prepared in the form of ribbon with rectangular cuttings (5×5 mm^2). The spacer was placed on the surface of thin glass plate protected with fine film of Teflon®. Then the drops of given mixture (A1-A3 or P1-P3) were placed into the center of each cuttings and pressed with another glass plate protected by Teflon®. This assembly was kept under moderate pressure for several minutes and then fixed by metallic holders. Prepared in such manner assembly was placed into oven and kept in air during 5 days at the temperature 75-80^{0}C. After polymerization the construction can be easily disassembled without damaging the films.

The film thickness was measured by optical microscope. Typical magnitudes of films were as follows: h = (110±10 μm) for A1 and A3; h = (160±10 μm) for A2; h = (180±15 μm) for P1, P2 and P3. Possible reason for difference in film thickness is viscosity of compositions under study. It was essentially higher in case of A2, P1, P2 and P3.

Just before experiment the film sample was prepared by cutting of size slightly less than that for metallic calorimetric plate. The films had good adhesion to the calorimeter material after slight pressing film to the metal surface. The composition A1, A2 and A3 were transparent and the quality of mechanical contact between metal plate and film can be easily controlled by visual examination. Opaque films P1, P2 and P3 were carefully adjusted to the plate by repeated slight pressing from one edge to another.

4.2. Thermal decomposition at low heating rate

The experiments on thermal decomposition were performed using commercial derivatograph OD 103 (Paulic, Paulic and Erdey, MOM, Hungary). In all runs the heating rate was equal to 10 K/s. The initial weight of samples was equal to 150 mg. Experiments with A1 and A2 were performed in air. All other compositions were tested in Ar enviroment.

Experimental data in the form of DTA, DTG and TG curves are presented in Figs. 4.1-4.6. The value of m is the relative mass of sample, $m = m (t) / m_0$, where m_0 is the initial mass of sample.

Figures 4.1 and 4.2 contain data on decomposition in air of A1 and A2 compositions, respectively. Qualitative behavior of TG and DTA curves is quite similar for these compositions. They start to loose weight at 20^0C and reach the maximum of weight loss rate at about 330^0C. The first exothermic peak is observed at the temperature about 310^0C while second one occurs at the temperature 550^0C. It is worth to note that we did not manage to observe noticeable endothermal evaporation of transformer oil from binder films, which was presumably masked by its oxidation in air [43] and by polymerization of rubber [44]. These processes contributed into the first exothermic peak. The second peak is the result of exothermic oxidation of the rubber residue [45, 46]. This peak is preceded by endothermal peak corresponding to melting/ solidification of rubber. Some distinctive features in behavior of A1 and A2 samples exhibit thermogravimetry. It is seen (TG and DTG curves) that thermal oxidative destruction of isopren rubber based binder A1 proceeds in 2 stages while in case of butadiene rubber based binder A2 it proceeds in 3 stages. After completing heating up to 700 ^0C there is no residue of A2 but in case of A1 some amount of porous residue (~ 2,5 % of initial weight) was observed.

Figure 4.3 collects data on decomposition in Ar of A3 composition based on energetic plasticizer. DTG and TG records has shown that the process is two – stage. The mass loss due to evaporation of DEGDN starts at about 100^0C. The initially endothermal process changes to exothermic one at the temperature $170-190^0C$. In this temperature range the mass loss rate is maximal and mass consumption reaches 88 %. During second stage ($200-600^0C$) there is relatively slow endothermal decomposition of nitryl rubber residue. After heating up to 700^0C, carbonaceous residue consisting of single filaments is observed.

The results on decomposition of P1 and P2 compositions are presented in Figs. 4.4 and 4.5, respectively. Qualitative behavior of both compositions is very similar and is characterized by one exothermic stage, that proceeds at the temperatures 230^0C for P1 and 280^0C for P2. Relatively low starting temperature for P1 can be explained by the presence of ferrocene catalyst in the formulation. One may suppose that this exotherm is mainly due to reaction between fine AP and melting rubber fuel. Important finding is that after exothermic reaction only 5 % of mass remains in derivatograph crucible. It means that gases released may disperse mechanically the heated material.

Thermal decomposition of P3 composition proceeds in 3 stages, as shown in Fig. 4.6. During the first stage ($170-190^0C$) the mass loss reaches 10 % and in the second stage ($240-270^0C$) it reaches 35 %. This approximately corresponds to evaporation /degradation of DEGDN whose content in P3 equals 36 %. The last, third decomposition stage is characterized by slow rate of mass loss (up to 37-38 % only) and negligible thermal effect. This is not clear why decomposition

of P3 does not continue at temperatures higher 300 ^{0}C. Therefore, it will take in the future special efforts to investigate in detail slow decomposition of P3 composition.
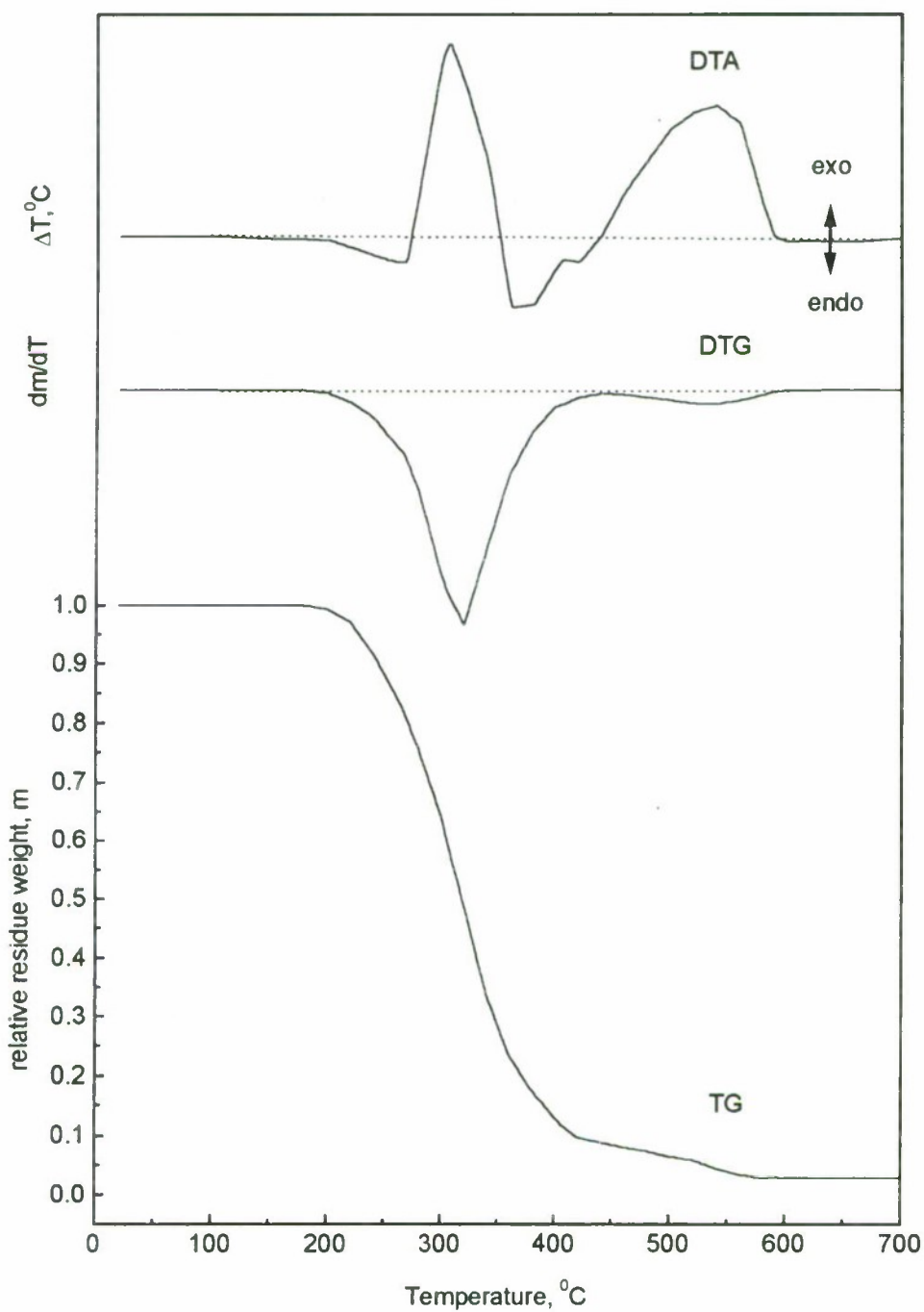

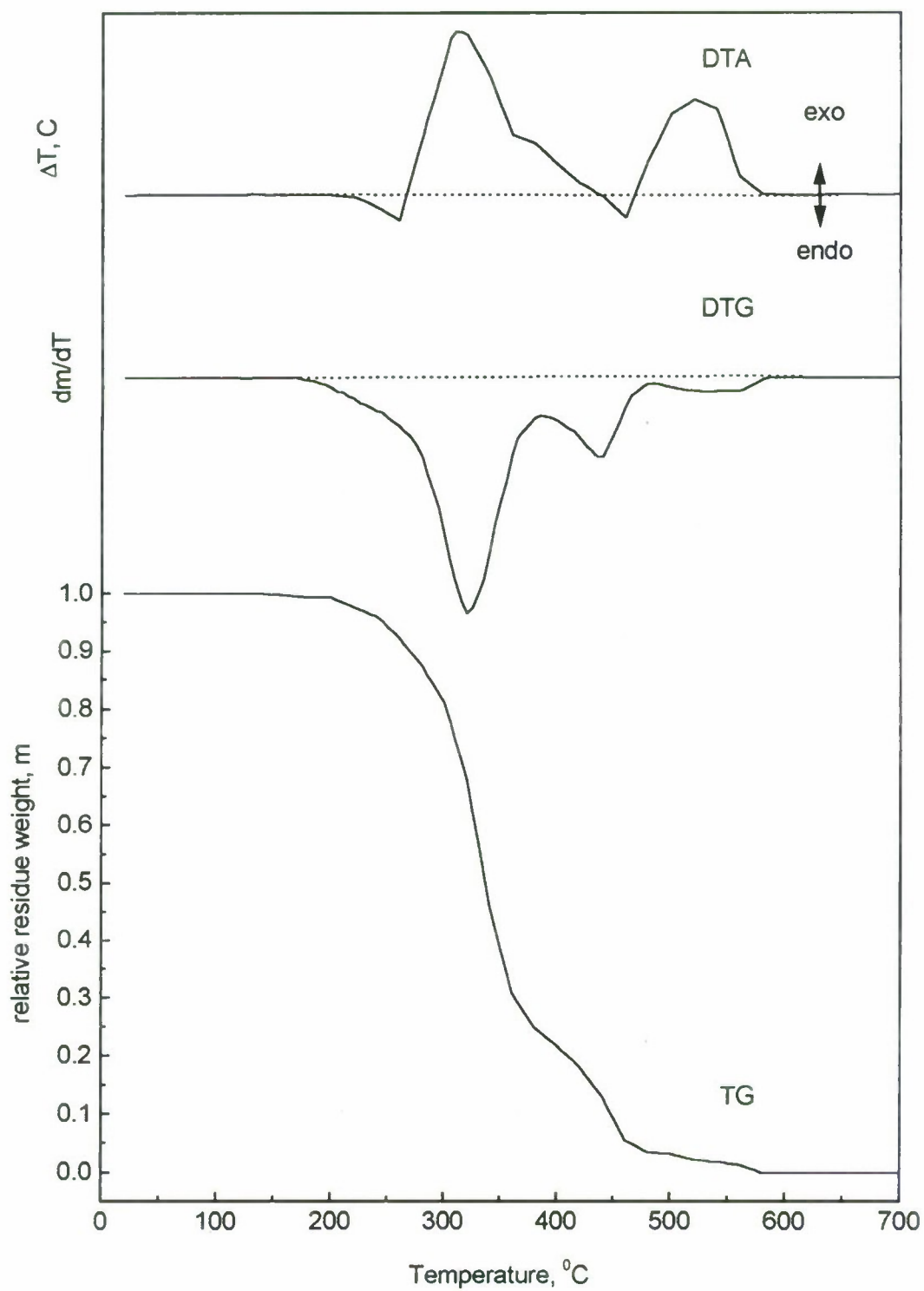Fig.4.1. DTA, TG and DTG traces for A1 composition at heating rate 10^{0}C/min in air.

Fig.4.2. DTA, TG and DTG traces for A2 composition at heating rate 10^0C/min in air.
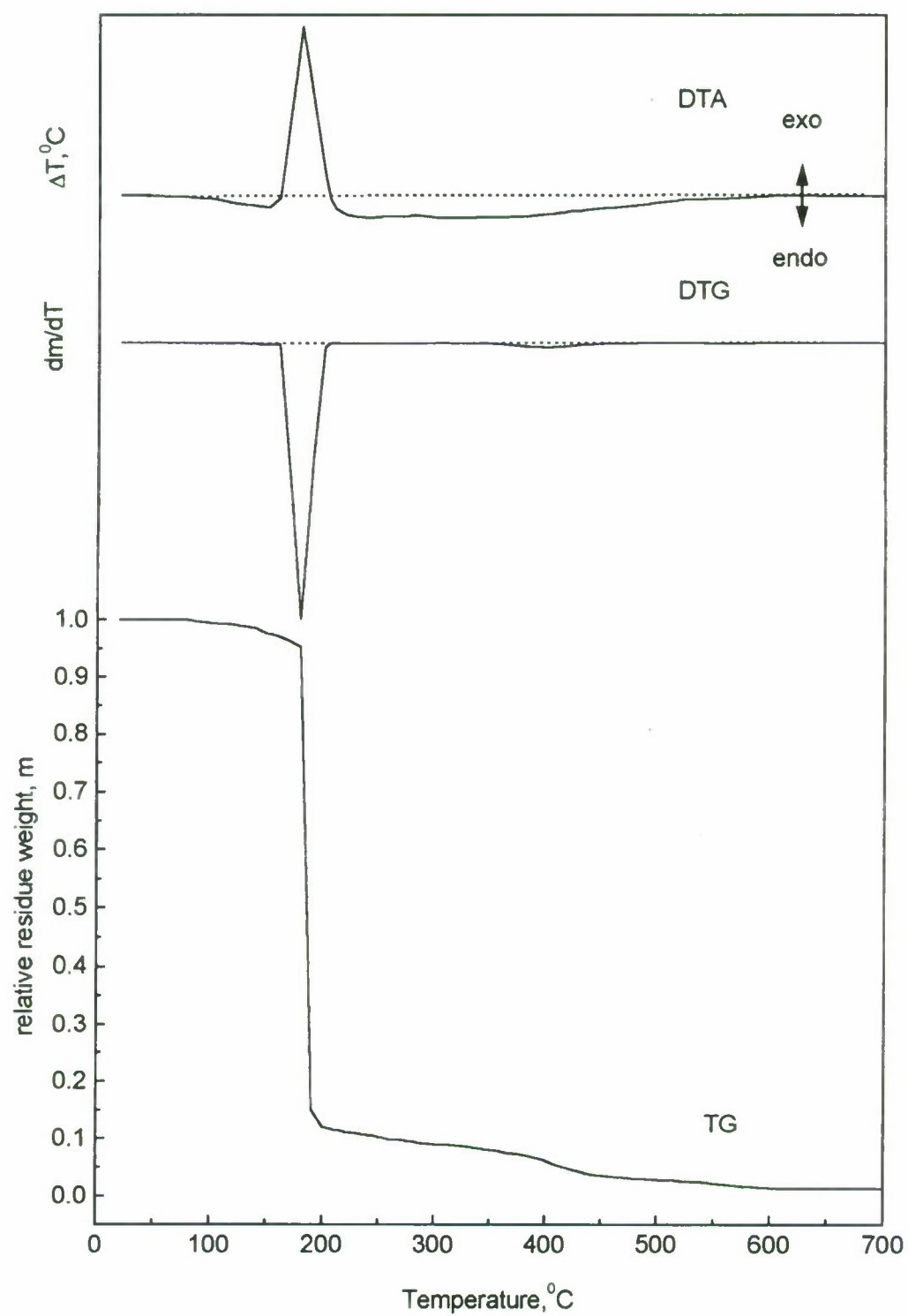
Fig.4.3. DTA, TG and DTG traces for A3 composition at heating rate 10^0C/min in argon.
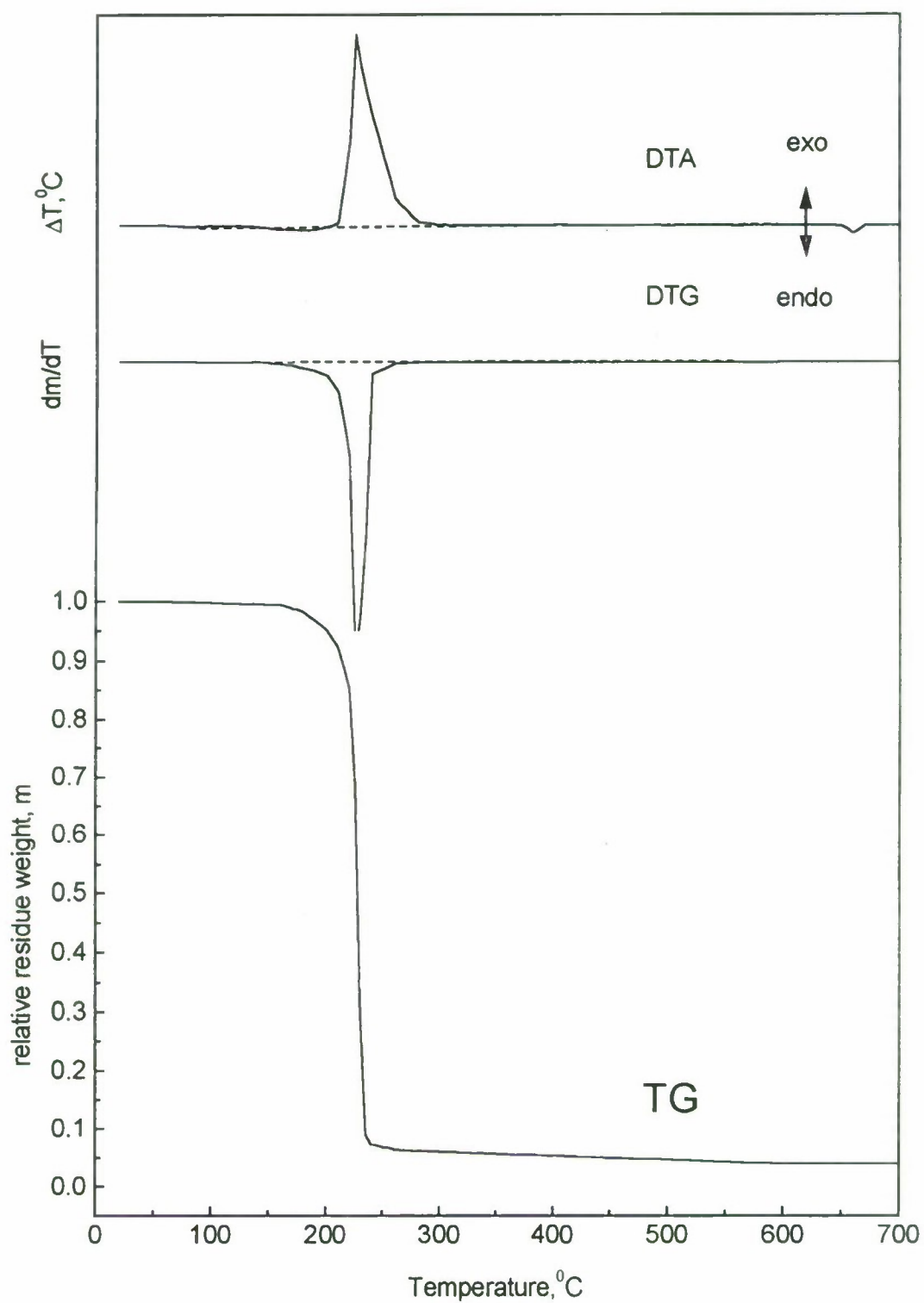
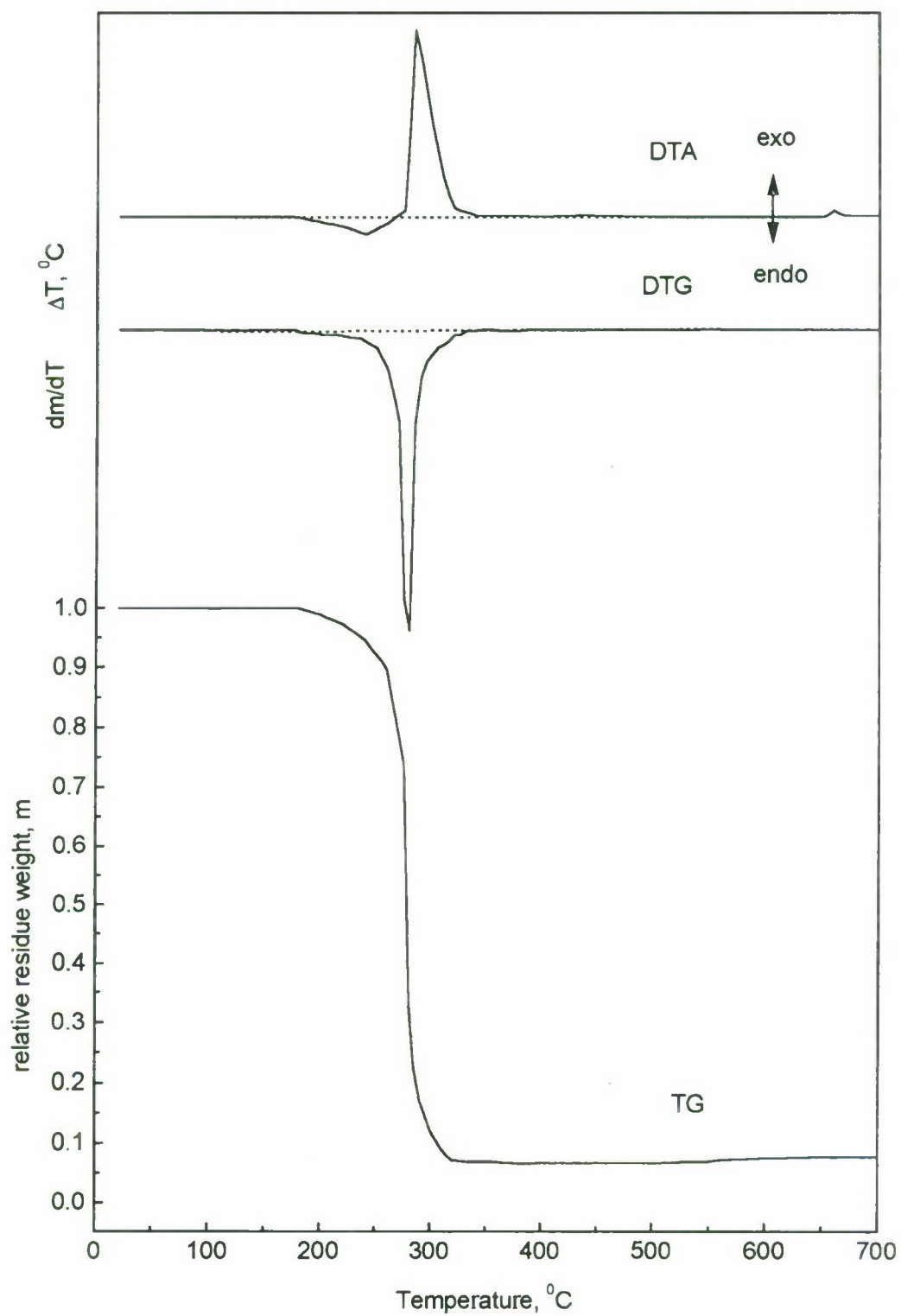Fig.4.4. DTA, TG and DTG traces for P1 propellant at heating rate $10^0C/min$ in argon.

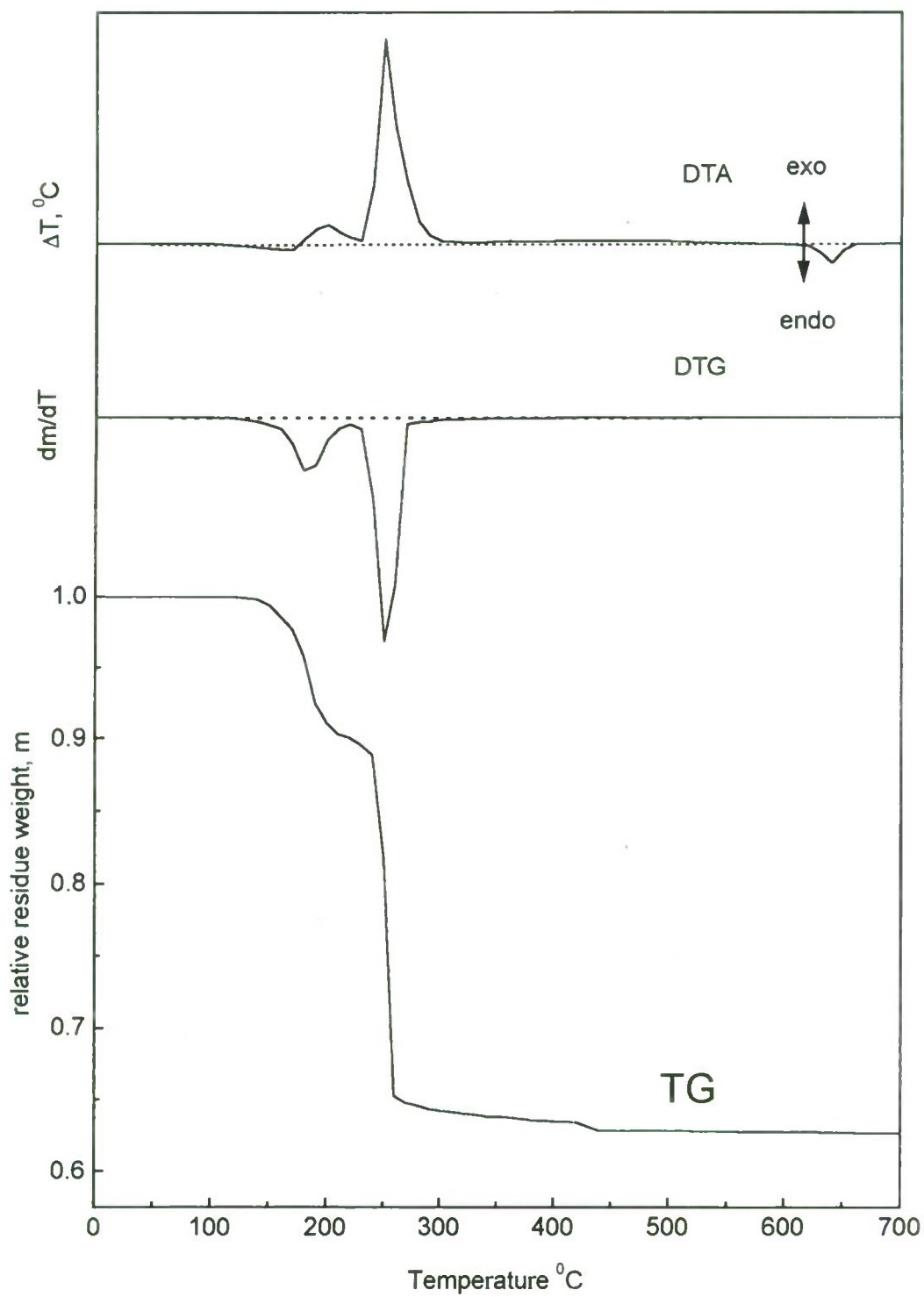Fig.4.5. DTA, TG and DTG traces for P2 propellant at heating rate 10^0C/min in argon.

Fig.4.6. DTA, TG and DTG traces for P3 propellant at heating rate 10^0C/min in argon.

4.3 . Thermal decomposition under fast heating.

4.3.1. Experimental technique

Thermal decomposition under fast heating rates gives valuable information on the processes in the combustion wave of solid propellants. Fast heating rates (>100 K/s) can be reached in different options of flash pyrolysis technique [49, 50]. In the present work fast heating of thin films of compositions A1-A3 and P1-P3 attached to the stainless steel 100 μm-thick foil was performed by radiation of Nd-YAG laser with wavelength 1.06 μm.

A sketch of the calorimeter is shown in Fig. 4.7. The foil liner with dimensions 2×2 mm² supplied with welded chromel-alumel thermocouples (100 μm wires) is attached to Teflon® ring with thermocouple spring holders. The A1÷A3 or P1÷P3 material film is mounted and kept by adhesion forces on the top surface of calorimeter plate. The sample assemblage is mounted on transparent plate and laser radiation is supplied from the bottom side of calorimeter (Fig. 4.8). To provide conditions for variation of environmental gas the assemblage is covered with transparent cover that allows visual observations of the process. Chosen geometry of laser heating permitted to avoid attenuation of radiant flux by aerosol particles formed in evaporation and decomposition of studied films. At the same time aerosol formation indicates intensity of mass loss. Scattered by aerosol particles at the angle 90° laser radiation was measured by photodiode in the wavelength band 0.98-1.1 μm. Scattered radiation was measured at the height of 4-5 mm above the calorimeter plate.

The total weight of calorimeter plate and film of studied material was in the range 0.5-1.0 mg. Laser power was equal 60 W, exposure time was about 4-5 s that ensured heating up to temperature 700°C. Signals measured by thermocouple and photodiode were digitized and stored in memory of personal computer. Video camera NV-M7EN (Japan) was used for visualization of heating and decomposition with framing rate 25 s⁻¹. The video records were synchronized with thermocouple and photodiode records.

For illustration, Fig. 4.9 shows example of thermocouple traces for calorimeter with and without sample. In this case a thin film of transformer oil (0.4 mg weight) played a role of evaporating film sample. It is seen that initial heating rate for calorimeter without sample amounts approximately 700 K/s while that for calorimeter with sample is about 450 K/s.

The heating of thermally thin body with mass m and heat capacity c by constant radiant flux q in presence of convective heat exchange is described by equation

$$mc \frac{dT}{dt} = -\alpha\, S\left(T - T_g\right) + kqS$$

Here S is the surface of heated body, k is the coefficient of radiation absorption, α is the convective heat exchange coefficient, T is the current averaged temperature of the body, T_g is the environmental gas temperature.
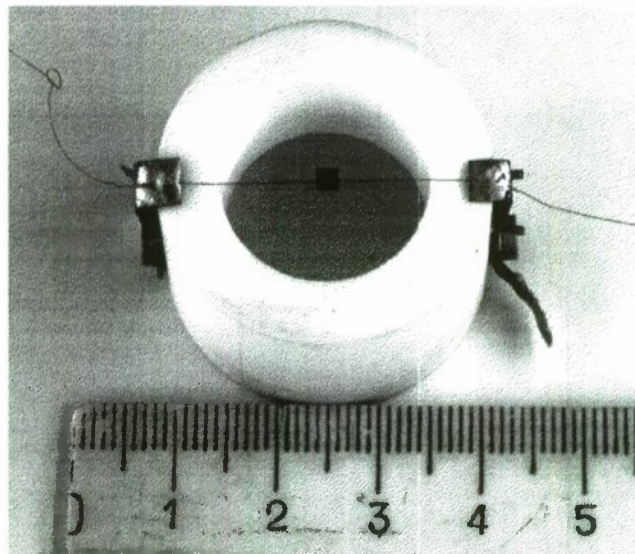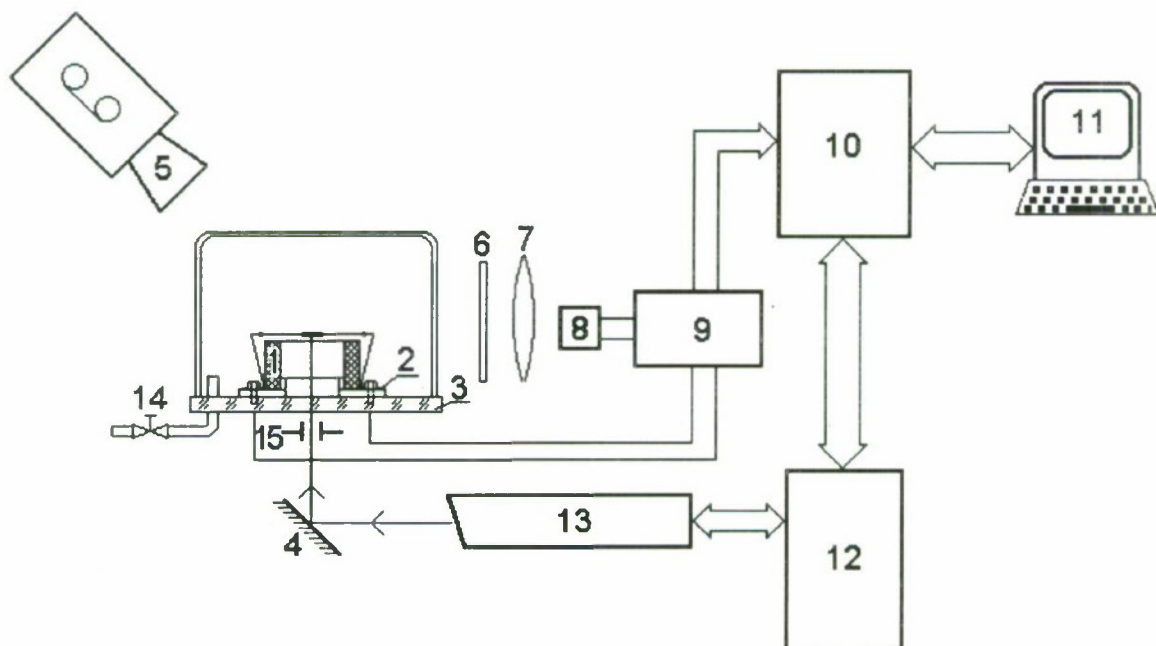
Fig. 4.7. A sketch of the plate calorimeter.

Fig. 4.8. A scheme of the experimental set-up.

1	-	Teflon ring with thermocouple spring holders,
2	-	Mounting ring,
3	-	Transparent plate,
4	-	Mirror,
5	-	Video camera,
6	-	Light filter,
7	-	Objective lens,
8	-	Photodiode transducer,

9	-	Amplifier,
10	-	CAMAC interface unit,
11	-	Computer,
12	-	Control supply laser unit,
13	-	Laser,
14	-	Gas outlet valve,
15	-	Diaphragm.

Assuming all coefficients constant, the temperature of heated body (initial temperature equals T_0) is given by

$$T - T_0 = T_1\left(1 - \exp\left(-at\right)\right) \qquad (4.1)$$

where $T_1 = \dfrac{kq}{\alpha S}$ and $a = \dfrac{\alpha S}{mc}$. Calculated by Eq. (4.1) temperature behavior is presented in Fig. 4.9 with dotted lines. It is seen nice correlation with experimental behavior at the initial stage of heating that can be treated as inert heating stage. The values for complexes T_1 and a were calculated by non-linear regression method based on algorithm of Levenberg-Murquat [51]. A comparison with experiments on heating of different inert materials showed that expression (4.1) describes well calorimeter thermal behavior until temperature 500^0C. The computer code gives calculated temperature data also at higher levels that corresponds to unique coefficient of heat exchange and constant mass of calorimeter. These data were used only for rough estimates of inert heating behavior.

4.3.2. Experimental results

Typical records of the temperature of calorimeter and photodiode signal corresponding to intensity of the light scattered by decomposition products of the films of studied compositions A1÷A3 and P1÷P3 are shown in Figs. 4.10-4.15. Experiments were conducted with heating rate about 450 K/s in nitrogen under pressure slightly exceeding atmospheric one. The dotted lines present calculated by Eq. (4.1) temperature curves upon assumption of inert heating of calorimeter without mass loss.

The calorimeter temperature behavior in case of A1 and A2 films heating is very similar, see Figs. 4.10 and 4.11. Temperature T_d on the experimental curve corresponds to the beginning of noticeable decomposition of film material. Analogous behavior of calorimeter has been observed in [49]. The magnitudes of T_d equal to 310±10°C for A1 and 330±14°C for A2. This temperature is close to the boiling temperature of transformer oil (350-400°C according [43]). Note that our experiments on fast heating the oil films, see Fig. 4.9, gave T_d=300-320°C.

Video records of A1 and A2 heating show that smoke starts to generate at the temperature 300-310°C. Shortly after this moment of time a central part of film forms bubble whose height gradually increases in magnitude. Finally, the film is transformed into liquid drop with cross-section less than surface of calorimeter. The drop size decreases with time and color of its material becomes dark. After completing heating (up to 700°C) there is no visible residue on calorimeter plate for both A1 and A2 films. The only difference in behavior of these materials is higher intensity of smoke generation in case of A2 film. This correlates with records of signal magnitude for scattered light.

Figure 4.12 presents data on fast heating of A3 film. It is seen again that overheating of calorimeter starts at the temperature T_d which correlates with the rise of scattered light signal and beginning of smoke formation. For A3 film T_d=255±7°C that is close to the boiling temperature of DEGDN, T_b=244°C. Video records show that in the beginning stage of heating the A3 film forms bubble with height changing periodically. Accordingly, scattered light signal also undergoes pulsation in time. On the second stage of heating a bubbled film changes color from yellow-brown to black, smoke generation rate increases, and bubble height decreases. After heating there is a black trace on the calorimeter plate which disappears in 1-2 sec heating in air. On the contrary to A1 and A2, the A3 film does not form liquid drop when heating up to 700°C.

It is worth to note that under slow heating the A3 material decomposes with exothermic effect at 180-190°C. No such effect has been detected under fast heating. Positive deviation of $T(t)$ curve from inert heating after point $T=T_d$ could not be definitely treated as a result of exothermic process. This effect can be mainly attributed to the loss of thermal contact between calorimeter and film for all tested materials. Quantitative determination of chemical reaction heat release becomes very uncertain at the temperatures higher T_d.

Studying of thermal decomposition of P1÷P3 films under fast heating was intended for clarifying details of "pocket" material behavior in the combustion wave. Figures 4.13-4.15 present the experimental data that exhibit many common features. The temperature T_d for these materials turns out significantly smaller than that for appropriate binder (compare Figs. 4.10 and 4.13, 4.11 and 4.14, 4.12 and 4.15, respectively). It is interesting to note that the light scattering signal rise is relatively small at the moment of reaching temperature T_d. When heated above temperature T_d, the calorimeter temperature increases smoothly with simultaneous rise of scattered light signal. Then the temperature curve undergoes sharp increase of the rate at the moment of reaching maximum on the light scattering signal. This point is designated as T_d^*. Video records show that during smooth temperature rise the films become bubbled (at the temperature approximately equal to half of sum of T_d and T_d^*) and smoke generation rate gradually increases. At the moment of reaching T_d^* the films detach abruptly from calorimeter leaving on metallic plate the aluminum aggregates. An example of such residue for P1 film shown in Fig. 4.16. Some less amount of aluminum aggregates leaves the P2-film while in the case of P3-film the residue represents large size carcass made of sintered Al particles. The weight of carcass equals to 45-50% of original weight of P3-film that correlates well with the content of aluminum in P3 formulation.
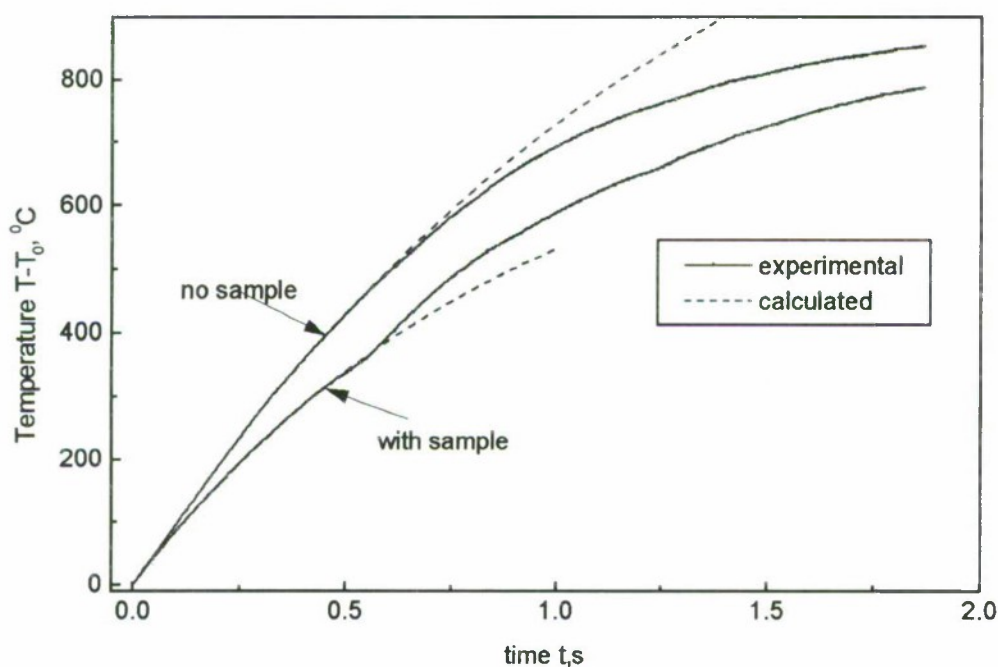

Fig. 4.9. Example of thermocouple traces for calorimeter with and without film sample.

Fig. 4.10. Calorimeter temperature and photodiode signal traces at fast heating for A1 composition in nitrogen.
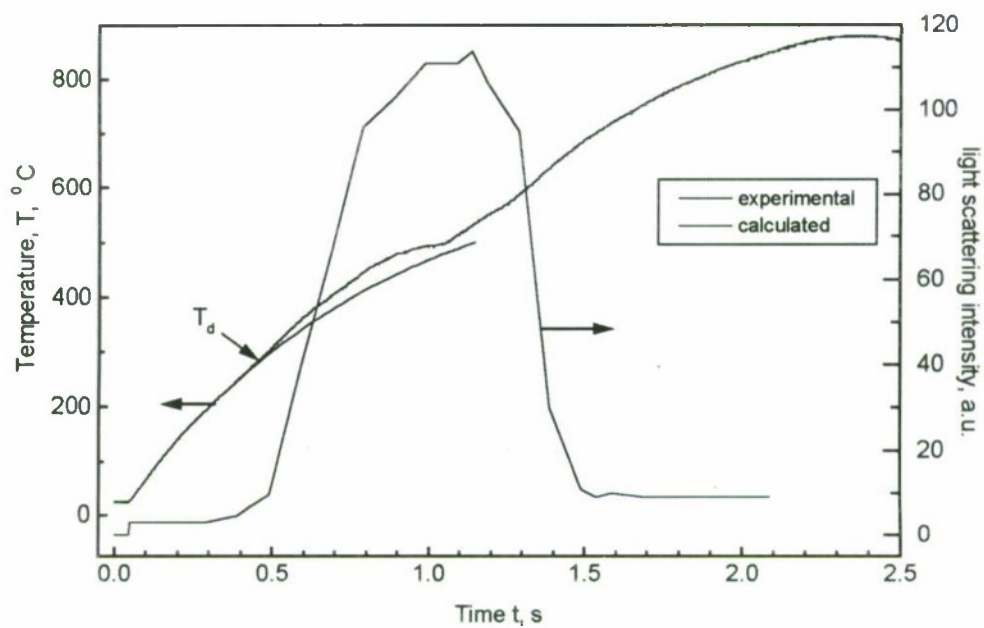

Fig. 4.11. Calorimeter temperature and photodiode signal traces at fast heating for A2 composition in nitrogen.

Fig. 4.12. Calorimeter temperature and photodiode signal traces at fast heating for A3 composition in nitrogen.

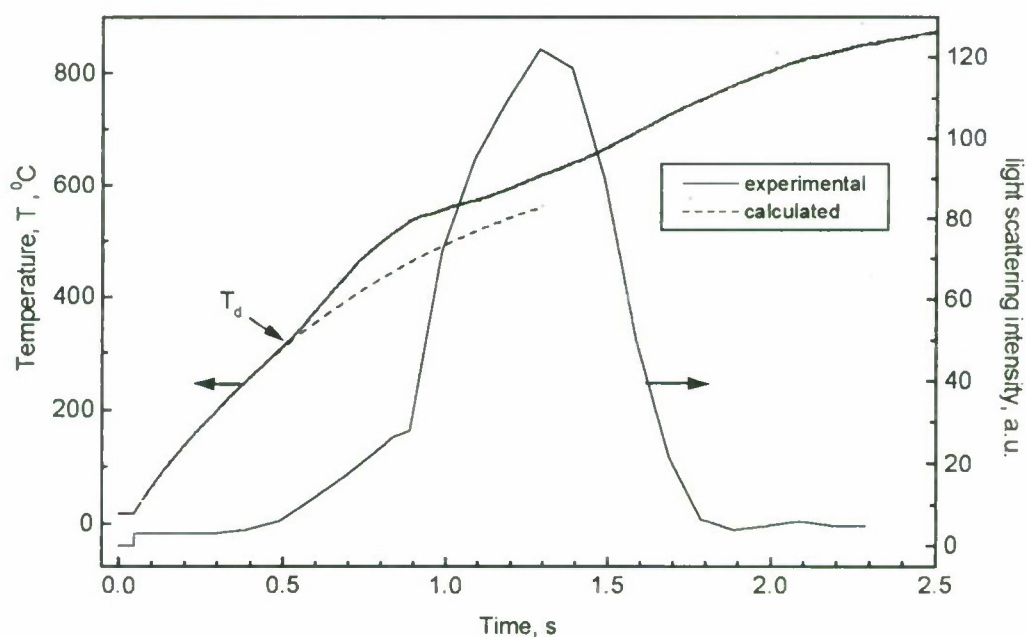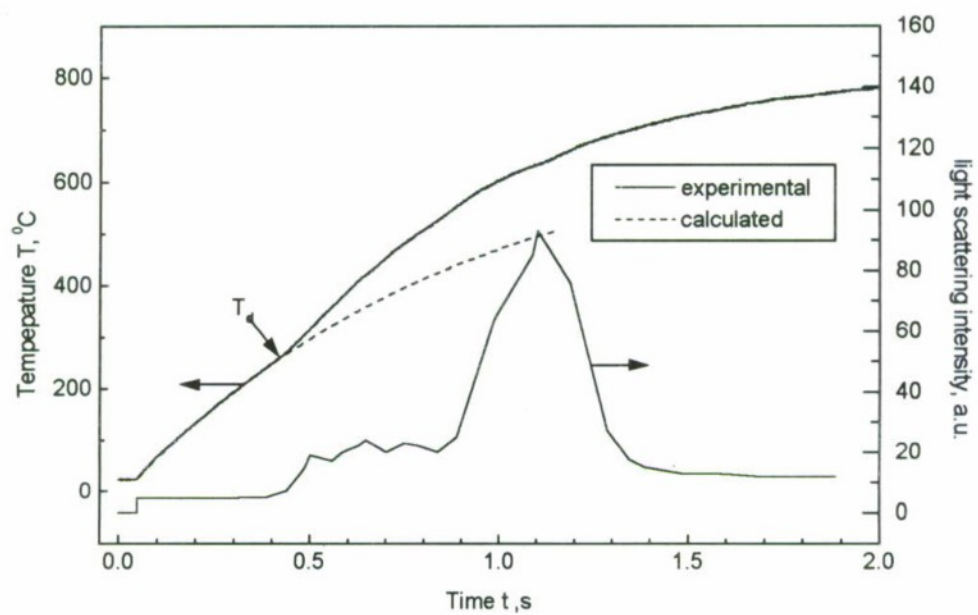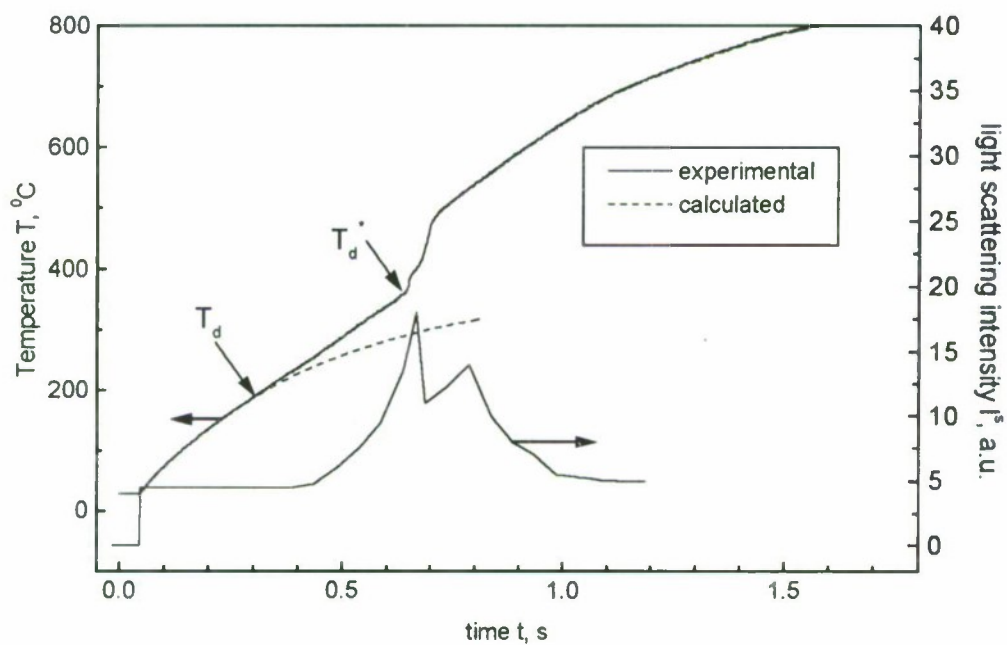Fig. 4.13. Calorimeter temperature and photodiode signal traces at fast heating for P1 propellant in nitrogen.
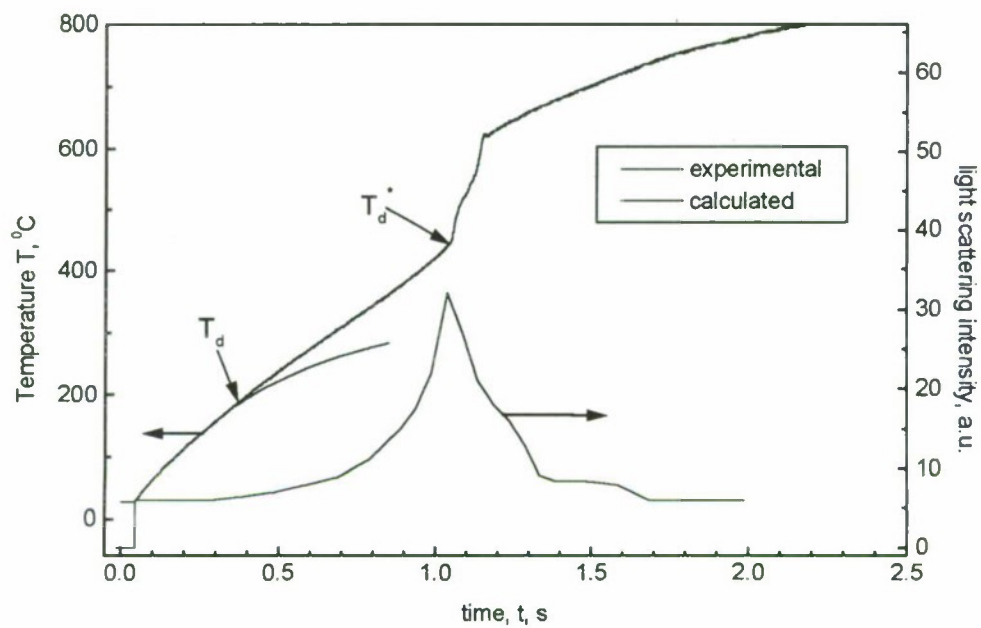
Fig. 4.14. Calorimeter temperature and photodiode signal traces at fast heating for P2 propellant in nitrogen.
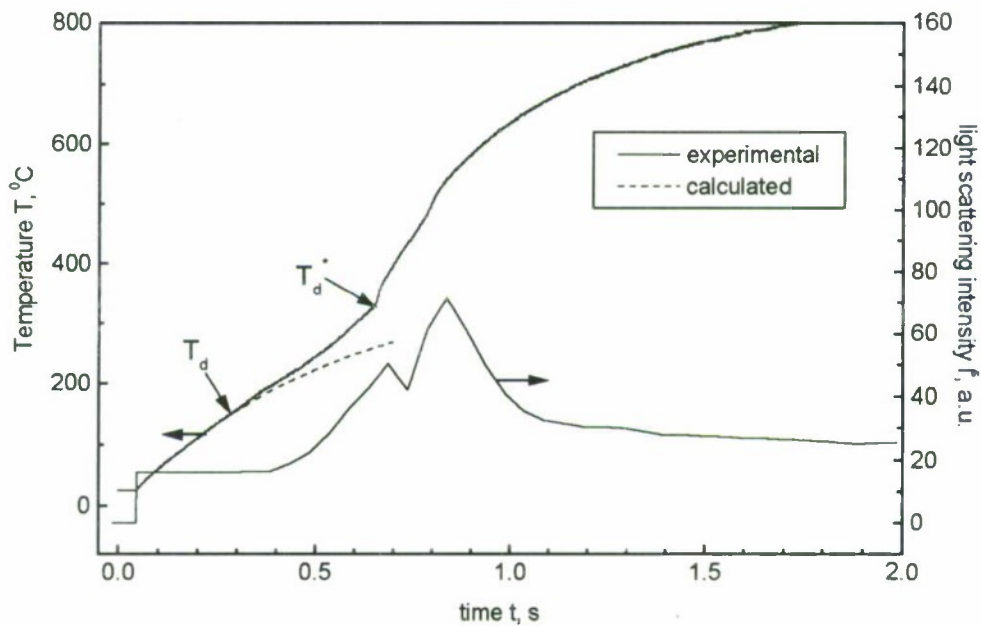

Fig. 4.15. Calorimeter temperature and photodiode signal traces at fast heating for P3 propellant in nitrogen.

Fig. 4.16. A residue for P1 film on the calorimeter plate.

CONCLUSIONS

The present work includes four investigation topics:
- Model agglomerate evolution.
- Drag coefficient for burning agglomerate.
- Condensed combustion products (both agglomerates and fine oxide particles) for Alex containing propellant formulations at elevated pressure.
- "Pocket matter" thermal decomposition behavior.

Below the main results are summarized for each topic.

Model agglomerate evolution

New approach for study of agglomerate evolution has been elaborated. The approach is based on use of special "super heterogeneous" propellants that generate during combustion the model agglomerates with given reproducible size and structure. "Super heterogeneous" propellant consists of non-metalized homogenized matrix with finite number of small insertions each of them converts into agglomerate in combustion wave. Uniformity of model agglomerates allows much more correct treatment of experimental data obtained via sampling technique than it can be done in the case of wide-varied agglomerate population in combustion of real propellants.

The experiments with agglomerates of $395 \div 540$ μm size and initial aluminum content 42.6 % were carried out in pressure range $1 \div 80$ atm. The following correlation for aluminum combustion efficiency has been found:

$$\eta = 2.86 \cdot t^{-0.28} \cdot P^{-0.20},$$

where $\eta = m_{Al} / m_{Al}^0$ - incompleteness of aluminum combustion; m_{Al} – mass of unburnt aluminum in sampled agglomerate, m_{Al}^0 – calculated initial mass of aluminum in agglomerate; t – the residence time for agglomerate in flame of super heterogeneous propellant ($20 < t < 90$ ms);
P – pressure ($10 < P < 70$ atm).

In addition, it was found that the mass fraction of oxide, accumulated on the burning agglomerate, increases with aluminum conversion extent. This is described by

$$\varphi = 0.539 + 0.213 \cdot \xi,$$

where $\varphi = m_{ox}^{ag} / m_{ox}^{exp}$ – mass fraction of oxide accumulated on agglomerate; m_{ox}^{ag} – mass of oxide in agglomerate (experimental); m_{ox}^{exp} – theoretical mass of oxide forming in course of combustion of aluminum; $\xi = 1 - \eta$ - completeness of aluminum combustion.

Due to oxide accumulation the agglomerate mass also increases with completeness of aluminum combustion ξ (or with time):

$$m/m_0 = 0.46 + 0.176 \cdot \xi,$$

where m is the mass of sampled agglomerate, m_0 is the initial agglomerate mass before burning.

Note that agglomerate begins its evolution in flame from the effective initial mass corresponding to the mass of aluminum in insertion.

The results obtained are in a good agreement with literature data on pure aluminum particle burning under zero gravity condition. This fact testifies similarity of combustion behavior of coarse aluminum particles and agglomerates.

The work is planned to be continued with various propellant formulations and different sizes of model agglomerates.

Drag coefficient during the motion of burning agglomerate

The experiments on visualization of the motion of model pseudo uniform agglomerates were performed at atmospheric pressure. Time-exposed, natural-luminosity images and trajectory points of burning particles moving in combustion products of non-metalized propellant were obtained using a gated charge coupled device (CCD) computer camera in conjunction with a chopper wheel. Rotation speed and slot arrangement of the chopper wheel was chosen to expose the CCD camera to the flame luminosity at intervals of 3 ms and for duration of 0.5 ms each. The treatment of trajectories allowed to obtain the drag resistance coefficient as the function of Reynolds number Re. When Re number varies in the range $7 \div 9$ the value of coefficient K in expression $C_d = K/Re$ equals $K = 45 \pm 7$. It is planning to continue experimental work in order to obtain similar data at elevated pressures (up to $20 \div 40$ atm) and in extended Reynolds number range ($Re = 1 \div 20$).

Condensed combustion products of Alex containing propellant formulations

Ultra fine metal powders seem to be promising additive to the propellant formulation to diminish agglomeration intensity. In current work the characteristics of condensed combustion products (including agglomerates) were measured via sampling technique at pressure 46 atm (argon or nitrogen) for 12 propellant formulations manufactured using well characterized ingredients. All compositions were based on energetic binder (20%). They included totally 18 % aluminum (commercial or fine particles in various proportion) and contained AP or AP and HMX as oxidizer.

• The propellants exhibited very effective aluminum conversion (total unburnt aluminum content in CCP did not exceed 9% for any fine aluminum containing formulation and the main portion of non-consumed aluminum was localized in agglomerates) and low intensity of the agglomeration process. The agglomeration behavior corresponds to *weakly agglomeration scenario* that is characterized by high efficiency of aluminum conversion into oxide particles and moderate size of agglomerates. For propellants under study the total range of CCP particle sizes is wide enough with maximum size of agglomerates reaching 950 μm, but main contribution into agglomerates mass is provided by particles with size up to approximately 300-400 μm. However, the agglomerate formation is relatively rare event that brings small mass contribution into total condensed products mass (1-12%).

• The replacement of commercial aluminum by Alex leads to increase of burning rate, decrease of agglomeration intensity and increase of metal conversion completeness. For propellants without HMX the mass size distribution function for different formulations is not changed significantly and increase of metal completeness is achieved mainly by decrease of mass fraction of agglomerates. The listed above trends are mostly expressed in combustion of HMX containing propellants which exhibit, as a rule, higher agglomeration intensity (for example, incompleteness of aluminum combustion for HMX-containing propellants is 3 times higher as compared with pure AP based propellants). The size distribution for these propellants transforms with Alex fraction. It is noteworthy to underline that in the case of HMX propellants even small amount of Alex (Alex/Al = 8.3/91.7) in propellant formulation gives sizable effect in terms of agglomeration behavior. The aluminum combustion incompleteness correlates with mass of agglomerates. For all propellants the dimensionless mass of agglomerate m_{ag} depends inversely proportionally on the burning rate. Presumably, enhanced heat release in subsurface layer of Alex

containing formulations cause changes in combustion behavior. Indirect evidence of that can be combustion of propellant based on pure Alex that demonstrated abnormally high burning rate (up to 300 mm/s) accompanied by destruction of sample holder.

- Additionally, when the experiments are carried out in argon instead nitrogen, the agglomerate mass is slightly lower.

For all propellants there is well recognized boundary $D_L \sim 100$ μm between coarse and fine CCP particles in the mass size distribution function. Fine CCP particles consist mainly of aluminum oxide. In special chemical and X-ray analyses the nitride phases were detected but their mass fraction was negligible. Regarding small oxide particles, the following observations were made:

- Three-peak structure of mass size distribution of oxide particles remains the same independently on aluminum type. The peaks are located in following histogram intervals: (1.2-1.5 μm), (3-3.9 μm) and (6.4-8.2 μm).

- The higher aluminum conversion degree, the greater oxide mass fraction in CCP. With consecutive replacement of aluminum by Alex the incompleteness of aluminum combustion decreases monotonously and mass size distribution $f(D)$ changes. The right hand side tail becomes shorter and the magnitude of function $f(D)$ increases in the size range 0.5-1.9 μm. This trend takes place for both propellant types - with and without HMX.

- The effect of environmental gas is found to be like the effect of changing the incompleteness of aluminum combustion. When the experiments are carried out in argon instead of nitrogen, the function $f(D)$ undergoes the same changes as if the aluminum combustion efficiency is increased. Namely, in most cases right hand tail becomes shorter and the magnitude of function $f(D)$ increases in the size range 0.5-1.9 μm.

Thus, the experiments have shown that addition of Alex may decrease the agglomeration intensity and increase the aluminum conversion degree. Similar results can be reached with different burning rate modificators that increase burning rate being small additives to the propellant formulation. However, there is no experimental evidences for such assumption and it can be checked in the future work. In addition, it seems important to establish minimal concentration of Alex that may affect agglomeration and combustion efficiency of commercial aluminum in solid propellant.

"Pocket matter" thermal decomposition behavior.

The thermal decomposition was investigated of three binder types based on 1) butadiene rubber, 2) isoprene rubber, and 3) nitryl rubber plasticized with diethylene glycol dinitrate (DEGDN) as well as of the metalized mixtures based on the same binders and modeling the "pocket" matter.

For low heating rate (10 K/min) the commercial derivatograph was used for DTA-TG-DTG measurements. For fast heating ($\geq$ 450 K/min) a special method was developed in which thin (110-180 μm thick) layer of substance was heated by laser flux (wavelength λ=1.06 μm) on metal plate equipped with thermocouple. Additionally, the intensity of source light scattered by condensed products in zone above the heated substance was measured by photodiode and the video registration of the processes on the substance surface was performed. It was revealed that:

- The characteristic temperature T_d^* when vigorous decomposition occurs under fast heating was higher than that for low heating rate for all binders and mixtures.

- Partial (local) swelling of layer-specimen and loss of thermal contact between layer and thermocouple plate observed under rapid heating made impossible correct layer temperature measurement and did not allow to estimate the heat release intensity properly.

- In the case of pure binders the decomposition temperature T_d was close to the temperature of evaporation/decomposition of used plasticizer (transformer oil or DEGDN).

- For isoprene binder and isoprene-based mixture the mechanical dispersion phenomenon was observed under fast heating.

- For pocket-modeling mixture based on nitryl rubber plasticized with DEGDN the formation of fragile porous frame of sintered aluminum particles has been observed.

Unfortunately, the data obtained on thermal decomposition of binders and pocket-modeling mixtures do not make clear the cause of difference in agglomeration behavior for corresponding propellant formulations. It stresses necessity of further investigations of rapid pyrolysis of more thin layers (<50 μm) combined with different visualization diagnostics.

LITERATURE CITED

1. Price, E. W. (1984). "Combustion of Metalized Propellants", In: *Fundamentals of Solid Propellant Combustion*, Progress in Astronautics and Aeronautics, Vol. 90, pp. 479-514.

2. Glotov, O. G., and Zyryanov, V. Ya. (1995). "The Condensed Combustion Products of Aluminized Solid Propellants. 1. The Method of Quenching at Various Distances from Burning Surface for Studying the Evolution of Particles". *Combustion, Explosion and Shock Waves*, Vol. 31, No. 1.

3. Zarko, V. E., Glotov, O. G., Karasev, V. V., Simonenko, V. N., Kiskin, A. B., Svit, A. G. L. K. Gusachenko (1998). "Studying the formulation effects on steady-state and transient combustion behavior of aluminized propellants". Final technical report under EOARD Contract F61708-97-W0197. Novosibirsk, 74 pages.

4. Fedotova, T. D., Malachov, V. V., Glotov, O. G., Kir'yanova, A. G. (1992). "Permanganatometric Determination of Metallic Aluminum in Condensed Combustion Products". *Siberian Chemical Journal*, No. 2, pp. 37-38 (in Russian).

5. Taylor, J. R. (1982). "An Introduction to Error Analysis". University Science Books Mill Valley, California.

6. "Theory of Turbulent Jets". (1984). Ed. by Abramovich G. I.. Moscow, Nauka, 716 p. (in Russian).

7. Gremyachkin, V. M., Istratov, A. G. , Leipunskii, O. I. (1980), "Theory of Metal Particle Combustion". In: *Physical Processes in Combustion and Explosion*, pp. 4-67. Moscow, Atomizdat. (in Russian).

8. Gremyachkin, V. M., Istratov, A. G. , Kolesnikov-Svinarev, and al. (1977), In: *Chemical Physics of Combustion and Explosion processes*. The Condensed Systems Combustion. AN SSSR Publ., Chernogolovka. (in Russian).

9. A. Zenin, G. Kusnezov, V. Kolesnikov. (1999). "Physics of aluminum particle combustion at zero-gravity". AIAA Paper 99-0696, pp. 1-6.

10. Glotov, O. G., Zyryanov, V. Ya. (1991). "The Effect of Pressure on Characteristics of Condensed Combustion Products of Aluminized Solid Propellant". Archivum Combustionis, Vol. 11, No. 3-4, pp. 251-262.

11. O. G. Glotov, V. E. Zarko, V. V. Karasev, M. W. Beckstead. (1998). "Aluminum Agglomeration in Solid Propellants: Formulation Effects". In: *Propellants, Explosives, Rockets, and Guns.* Proceedings of the Second International High Energy Materials Conference and Exhibit, December 8–10, 1998, IIT Madras, Chennai, India, pp. 131-137. (2ndIHEMCE: LOG NO 162A).

12. Williams, F. A. (1985). "Combustion Theory". Benjamin/ Cummings, Menlo Park, CA,.

13. Brauer B. (1971). "Grundlagen der Einphasen- und Mahrphasen-stromungen". Verlag Sauerlander, Aarau and Frankfurt.

14. Gorbis Z. R., Spokoinyi F. E. (1977). "Physical model and mathematical description of fine particle motion in turbulent two-phase flow". Thermophysics of high temperatures, v.15, No. 2, , pp. 399-408. (in Russian).

15. Shriber A. A., et al. (1987). "Turbulent two-phase flows". Kiev , Naukova Dumka. (in Russian).

16. Klyachko L. S. (1934). "Equation for motion of dust particles in dust trap devises". Heating and Ventilation, No. 4, pp. 11-17. (in Russian).

17. A. Putnam. (1963). Integratable Form of Droplet Drag Coefficient. ARS Journal, v. 31, No. 10, pp. 1467-1468.
18. Sternin L. E., Shriber A. A., Maslov B. M. et al. (1980). "Two-phase mono- and poly dysperse particles flow (Ed. by Sternin L. E.), Moscow, Mashonostroenie. (in Russian).
19. Clift R, Grace J. R. and Weber M. E. (1978). "Bubbles, Drops and Particles". Academic Press, New York.
20. Bailie, R. C. (1978). "Energy Conversion Engineering". Addison-Wesley, New York.
21. Chigier, N.A. (1976). "Progress in Energy and Combustion Science". 2:97-114
22. Renie J. P., Osborn , J. P.(1979). "Combustion Modeling of Aluminized Propellants". AIAA Paper, 79-1131.
23. Harrje, D. T., and Reardon, F. H. (1972). "Liquid Propellant Rocket Combustion Instability", NASA SP-194, 70, Washington, DC.
24. Price E. W. (1979). "Combustion of Aluminum in Solid Propellant Flames". Proceedings of 53rd AGARD/PEP Meeting.
25. L. H. Caveny, A. Gany. (1979). "Breackup of Al/Al$_2$O$_3$ Agglomerates in Accelerating Flowfields". AIAA Journal, v.17, No. 12, pp.1368-1371.
26. Brundige W. N., Caveny L. H. (1984). "Low Burning Rate Aluminized Propellants in Acceleration Fields".- AIAA Journal, , v. 22, No. 5, pp. 638-646.
27. J. Yin, B. Li, K. Wang, and X. Wu (1991). "On the velocity and evaporation of drops during liquid quench of solid rocket motor (China)". AIAA Paper 91-1952
28. Babii V. I., Ivanova I. P. (1965). "Aerodynamic drag of particle under nonisothermic conditions". Thermoenergetica, No. 9, pp. 19-23. (in Russian).
29. Babii V. I., Kuvaev Yu. F. (1986). "Combustion of coal dust and simulation of dust coal flame". Moscow, Energoatomizdat, 207 pages. (in Russian).
30. Marshall, R.L., Pellet, G.L., and Saunders, A.S. (1967). "An Experimental Study of the Drag Coefficient of Burning Aluminum Droplets". Air Force Rocket Propulsion Laboratory Two- Phase Flow Conference, Norton Air Force Base, San Bernardino, California, March, p. 843.
31. Kanury, A.M. (1975). "Introduction to Combustion Phenomena". Gordon and Breach, New York.
32. .Eisenklam P., Arunachalam S.A. and Weston J.A. (1967). "Evaporation Rates and Drag Resistance of Burning Drops". In: *11th Symposinm (Intern.) on Combustion*, The Combustion Institute, Pittsburgh, pp. 715-728.
33. Strongin M. P., Koshelev K. B. (1993). "Mathematical modeling transient effects in streamline of individual burning particle". *Combustion, Explosion and Shock Waves*, Vol. 29, No. 3.
34. V. N. Simonenko, V.E. Zarko. (1999). "Comparative studying the combustion behavior of composite propellants containing ultra fine aluminum". In: *Energetic materials. 30th Int. Annual Conf. of ICT*, Karlsruhe, Germany. Report 21, 14 pages.
35. A. E. Sal'ko. (1995). "Certain aspects of development and use of novel ultrafine powdered materials." In: *Chemical gasdynamics and combustion of energetic materials*. Tomsk, 1995. Int. Workshop TW95, Book of Abstracts. Report P8, pp. 10-12.
36. I. M. Kolthoff, E. B. Sandel. (1948). Quantitative chemical analysis. Moscow, Goskhimizdat. (in Russian).
37. G. V. Samsonov. (1969)."Nitrides". Kiev, Naukova Dumka. (in Russian).

38. G. V. Samsonov. O. P. Kulik, V. S. Polischuk. (1978)."Methods of preparation and analysis of nitrides". Kiev, Naukova Dumka. (in Russian).

39. Zarko, V. E., Glotov, O. G, Karasev, V. V. (1996). "The effect of solid propellant binder on the formation and evolution of condensed combustion product particles". Final technical report under Brigham Young University Contract. Novosibirsk. 81 pages.

40. Glotov, O. G., Zarko, V. E., Karasev, V. V., Beckstead, M. W. (1998). "Condensed combustion products of metalized propellants of variable formulation". AIAA Paper 98-0449, 6 pages.

41. Glotov, O. G., Zarko, V. E., Karasev, V. V., Beckstead, M. W. (1997). "Effect of Binder on the Formation and Evolution of Condensed Combustion Products of Metalized Solid Propellants", In: *Combustion and Detonation. 28th Int. Annual Conf. of ICT*, Karlsruhe, Germany, Report 75, 14 pages.

42. Physical properties. (1991). Handbook, Ed. by A. P. Babichev et al. Moscow, Energoatomizdat, 1232 pages. (in Russian).

43. Lipshtein R.A., Shahnvich M. I. (1983) "Transformer Oil". Moscow, Energiya. (in Russian).

44. Bryik M.T. (1989). "Decomposition of loaded polymers". Moscow, Chemistry. (in Russian).

45. Corshak V.V. (1970). "Chemical structure and temperature characteristics of polymers", Moscow, Nauka. (in Russian).

46. Dolgoplosk E.A., Tinyakova E. I. (1961). "Thermal destruction of some polymers", Journal of Chemical Industry, vol. 52, No 11, Moscow (in Russian).

47. Lur'e B. A. (1990). "Diethylene glycol dinitrate", In: *Chemical Encyclopedia*, vol. 2, Moscow, Sovskaya Encyclopedia. (in Russian).

48. Jojic I. and Brewster M.Q. (1998) "Condensed-Phase Chemical Interaction between Ammonium Pelchorate and Hydroxyl-Terminated Polybutadiene", Journal of Propulsion and Power, vol.14, No 4.

49. Chen J. K. and Brill T. B. (1991) "Chemistry and Kinetics of Hydroxyl-Terminated Polybutadiene (HTPB) and Diisocyanate-HTPB Polymers during Slow Decomposition and Combustion-like Conditions", Combustion and Flame, vol. 87, pp. 217-232.

50. Arisawa H. and Brill T. B. (1996). "Flash Pyrolysis of Hydroxyl-Terminated Polybutadiene (HTPB): Implications of the Kinetics and Mechanism to Combustion of Organic Polymers", Combustion and Flame, vol. 106, pp. 131-154.

51. Press W. H. et al. (1986). "Numerical Recipes: The Art of Scientific Computing", Cambridge University Press, 818 pp.

52. Pavlov P. A. (1988). "Boiling dynamics of strong superheating liquids". Sverdlovsk, Ural Branch of USSR Academy of Sciences Publ., 248 pp. (in Russian).